CERAMIC ADDITIVE MANUFACTURING BY MICRON SIZED DROPLET JETTING OF THERMOPLASTIC FEEDSTOCKS

İpeknaz Özden Moser

Doctoral Dissertation
Jožef Stefan International Postgraduate School
Ljubljana, Slovenia

Supervisor: Assoc. Prof. Dr. Andraž Kocjan, Jožef Stefan Institute, Department for Nanostructured Materials, Ljubljana, Slovenia
Co-Supervisor: Dr. Aljaž Iveković, Jožef Stefan Institute, Department for Nanostructured Materials, Ljubljana, Slovenia

Evaluation Board:
Assoc. Prof. Dr. Danjela Kuščer Hrovatin, Chair, IPS and Jožef Stefan Institute, Ljubljana, Slovenia
Prof. Dr. Saša Novak Krmpotič, Member, IPS, Ljubljana, Slovenia
Dr. Andrea Zocca, Member, Bundesanstalt für Materialforschung und -prüfung (BAM), Berlin, Germany

MEDNARODNA PODIPLOMSKA ŠOLA JOŽEFA STEFANA
JOŽEF STEFAN INTERNATIONAL POSTGRADUATE SCHOOL



İpeknaz Özden Moser

CERAMIC ADDITIVE MANUFACTURING BY MICRON SIZED DROPLET JETTING OF THERMOPLASTIC FEEDSTOCKS

Doctoral Dissertation

ADITIVNO OBLIKOVANJE KERAMIKE NA PODLAGI TERMOPLASTIČNE EKSTRUZIJE MIKROMETRSKIH KAPLJIC

Doktorska disertacija

Supervisor: Assoc. Prof. Dr. Andraž Kocjan

Co-Supervisor: Dr. Aljaž Iveković

Ljubljana, Slovenia, December 2025

Acknowledgments

First and foremost, I would like to express my appreciation to my supervisor, Assoc. Prof. Andraž Kocjan, for giving me the opportunity to embark on this journey of doctoral studies and for his continuous support, guidance, and patience along the way. I would also like to thank my co-supervisor, Dr. Aljaž Iveković, for his help, understanding, and ability to stay calm when I could not.

I would like to thank the Slovenian Research Agency for supporting this work with funding through the research project Preclinical and clinical investigations of zirconia dental ceramics fabricated by additive manufacturing technologies (J3–3064), and the research program Ceramics and complementary materials for advanced engineering and biomedical applications (P2–0087).

I am grateful to the JECS Trust for funding my visit to the Fraunhofer Institute for Ceramic Technologies and Systems IKTS, Dresden, Germany (Contract No. 2019230) for a mobility project entitled "Thermoplastic 3D printing of wax-based zirconia feedstocks". I thank Dr. Uwe Scheithauer and his colleagues for welcoming me warmly during my stay.

I acknowledge my colleagues from K7 for their help and support in and out of the lab, for all the good times: picnics, birthday celebrations, and even skiing trips!

Last but not least, I thank my family for their unconditional love, strength, and patience. And finally, Matjaž, thank you for holding my hand through absolutely everything.

Abstract

Thermoplastic 3D printing (T3DP) is an additive manufacturing (AM) process where micron sized droplets of thermoplastic wax-based feedstocks, with high solid content of ceramic powder, are deposited with high precision and resolution. The complete workflow of T3DP, from the properties of the suspensions to the process parameters, to deposit droplet by droplet, forming lines and layers, needs to be understood and controlled. Since T3DP is a relatively new AM technique, the studies of the suspension rheological requirements have been limited. It was reported that the suspensions should exhibit a shear thinning behavior in a given viscosity window. The details about colloidal particle interactions, whether particles should be weakly flocculated (at secondary minimum) and have a yield point, and their influence on the printability, however, have not yet been studied. Next to the properties of the used feedstocks, the role of the infill strategy for the formation of layers from lines, an important process parameter being highly sensitive to the introduced flaw type population, which ultimately determines final mechanical strength and reliability of T3DP-printed and sintered ceramic parts, is yet to be investigated.

The goal of this doctoral thesis was to study and control the complete workflow of T3DP in a systematic approach consisting of two main parts. In the first part of the study, paraffin-wax suspensions highly loaded with fine zirconia powder, stabilized by a combination of surfactants with significantly different chain lengths, were prepared. The relation between the surfactant chain length, conformation, and interparticle interactions, as well as the rheological behavior of the suspensions, such as viscosity, yield stress, storage, and loss moduli, was investigated in detail. Furthermore, the feedstocks were deposited in the form of individual droplets, lines, and single layers to correlate these rheological properties with jettability. It was found that the conformation and thickness of the steric barrier were critical parameters, affecting the rheological properties and the state of suspensions, being weakly flocculated or well dispersed, depending on the surfactant chain length (2.4 nm or 10 nm) and the ratios of the used surfactants. Thus, it was shown that T3DP jettability was dictated not only by the viscosity of the feedstocks but also by their respective yield point. In the second part of the study, wax-based zirconia feedstocks were printed in the form of rectangular bending bars with 3 different infill strategies, i.e., 0°, 90°, and alternating 0° + 90°. The homogeneity of formed bars, the type of flaw populations, final sintered density, Weibull strength distribution, and fractography were studied. It was shown that the infill strategy did not have a significant effect on the mechanical properties for T3DP, unlike other AM processes such as fused filament fabrication. However, the Weibull moduli obtained from the parts were significantly lower than the values achieved by other AM processes. Fractography revealed two types of flaws in the form of feedstock inhomogeneities and/or voids from imperfect fusion of subsequent droplets, indicating a need for improvement of both feedstock properties and process parameters.

T3DP allows for the preparation of complex-shaped ceramic parts and multi-material components that can be used in many different areas, such as dentistry, biomedicine, the semiconductor industry, and catalysis. However, understanding the interparticle

interactions and resulting rheological behavior of highly-loaded paraffin-wax suspensions is essential for their successful implementation. The thesis delivers a "*roadmap*" for the design of the steric barrier thickness and configuration, which governs various rheological properties of the feedstocks, with defined boundaries for the successful jetting outcome, going beyond the state of the art for T3DP.

Povzetek

Termoplastično 3D-tiskanje (ang. thermoplastic 3D printing, T3DP) je postopek aditivnega oblikovanja keramike na osnovi iztiskanja mikrometrskih kapljic termoplastične suspenzije z visoko vsebnostjo keramičnega prahu. Tak način nanašanja omogoča natančno oblikovanje komponent z visoko ločljivostjo. Nanesene kapljice se na podlagi z ohlajanjem strjujejo, z delnim prekrivanjem kapljic pa tvorimo posamezne linije in nato dvodimenzionalne plasti celotne komponente, kar dela postopek T3DP kompleksen. Za popolno obvladovanje postopka T3DP je tako potrebno razumeti ne samo parametre tiskanja, tj., načrtovanje in strategijo brizganja kapljic na podlago, ampak tudi lastnosti uporabljene keramične suspenzije (surovine). T3DP je razmeroma nov postopek aditivnega oblikovanja keramike, zato v literaturi ni veliko podatkov o primerni sestavi in zahtevanih lastnostih suspenzij. Znano je le, da morajo suspenzije izkazovati psevdoplastično obnašanje, ni pa znano, kakšne meddelčne interakcije so dopustne, tj., ali so lahko delci šibko flokulirani in ali mora suspenzija izkazovati mejno strižno napetost. Do te mere meddelčne interakcije suspenzij za T3DP še niso bile dovolj raziskane, a vendar ključno vplivajo na reološke lastnosti ter na uspešnost aditivnega postopka T3DP. Neraziskan ostaja tudi vpliv strategije oblikovanja plasti iz posameznih linij združenih kapljic (ang. infill strategy). Strategija tiskanja je ključni procesni parameter, ki določa vrsto nastalih napak v oblikovancu, ki nadalje določajo mehansko trdnost in zanesljivost tako oblikovanih ter sintranih keramičnih komponent.

Cilj doktorske disertacije je bil sistematično preučiti zakonitosti in načrtovanje keramičnih suspenzij in celoten postopek T3DP za uspešno oblikovanje zanesljivih keramičnih komponent. Prvi del disertacije zaobjema načrtovanje in pripravo keramičnih suspenzij na osnovi parafinskega voska z visoko vsebnostjo keramičnega prahu cirkonijevega oksida, pri čemer je bil prah dispergiran v vosek z uporabo kombinacije površinsko aktivnih snovi z različnimi dolžinami verig. Podrobno je bila preučena povezava med dolžino verige surfaktanta, možne konformacije, ko je adsorbiran na površini keramičnega delca in posledičnega vpliva na meddelčne interakcije, ter reološkega obnašanja suspenzij, kot so viskoznost, mejna strižna napetost, elastični in viskozni modul. Sledi preučevanje sposobnosti iztiskanja oziroma brizganja in združevanja posameznih kapljic v linije ter nanešene plasti na podlago kot posledico različnih reoloških lastnosti suspenzij v odvisnosti od danih meddelčnih interakcij. Ugotovljeno je bilo, da sta konformacija in debelina sloja surfaktantov ključna parametra, ki vplivata na reološke lastnosti in obnašanje termoplastične suspenzije. Glede na dolžino verige uporabljenih površinsko aktivnih snovi (2,4 nm ali 10 nm) ter njihovo množinsko razmerje so lahko delci v suspenziji šibko flokulirani ali dobro dispergirani. Izkaže se, da je poleg viskoznosti suspenzije izredno pomemba tudi prisotnost ter magnituda mejne strižne napetosti za uspešno oblikovanje linij in plasti s postopkom T3DP. Namen drugega dela disertacije je bil študirati vpliv strategije aditivnega oblikovanja palčk iz cirkonijevega oksida na

upogibno trdnost, zanesljivost in naravo vnesenih napak tekom oblikovanja. Glede na uporabljeno strategijo oblikovanja, tj., 0°, 90° ali izmenično 0° + 90°, je bila preučena homogenost oblikovanih preizkušancev, končna sintrana gostota vrsta in velikost (fraktografija), upogibna trdnost ter Weibullova porazdelitev trdnosti. Za razliko od drugih postopkov aditivnega oblikovanja, kot na primer metode termoplastičnega spajanja filamenta (ang. fused filament fabrication), strategija oblikovanja plasti pri T3DP nima večjega vpliva na mehansko trdnost in tip napak. Kljub temu pa so bile izmerjene vrednosti Weibullovega modula vzorcev T3DP bistveno nižje od vrednosti, ki jih dosega keramika iz cirkonijevega oksida, pripravljena z drugimi postopki aditivnega oblikovanja. Fraktografska analiza je razkrila dva tipa napak, tj., primarne vnesene napake kot posledica nehomogenosti suspenzije in/ali sekundarne v obliki praznin kot posledica nepopolnega združevanja iztisnjenih kapljic, kar kaže na potrebo po izboljšavah tako pri homogenizaciji suspenzije kot pri nastavitvah procesnih parametrov.

T3DP tehnologija aditivnega oblikovanja omogoča izdelavo keramičnih komponent kompleksnih geometrij iz enega ali več keramičnih materialov, uporabnih na številnih področjih, kot so stomatologija, biomedicina, polprevodniška industrija in kataliza. Vendar pa je za uspešno implementacijo tehnologije T3DP bistveno razumevanje meddelčnih interakcij in posledičnega reološkega obnašanja suspenzij, ki se uporabijo kot surovine za tisk. Doktorska disertacija ponuja poglobljen vpogled na razumevanje in načrtovanje meddelčnih interakcij keramičnih delcev v parafinskih suspenzijah, ki določajo reološke lastnosti teh suspenzij, in definira meje za uspešno nanašanje kapljic s tehnologijo T3DP za aditivno oblikovanje keramičnih komponent.

Contents

List of Figures **xv**

List of Tables **xvii**

Abbreviations **xix**

1 Introduction **1**
1.1 Additive Manufacturing of Ceramics 1
1.2 Ceramic AM Processes that Utilize Thermoplastic Feedstocks 4
1.2.1 Fused filament fabrication 5
1.2.1.1 Preparation and properties of filaments 6
1.2.1.2 The infill strategy for filament deposition 7
1.2.1.3 Post processing and characterization of printed parts 7
1.2.2 Thermoplastic 3D printing 10
1.2.2.1 Suspensions used for T3DP (and LPIM) ceramic manufacturing 12
1.2.2.2 Post-processing of parts prepared by T3DP (and LPIM & FFF) 14
1.3 Colloidal Particle Interactions in Thermoplastic Suspensions 14
1.3.1 Attractive particle interactions 15
1.3.2 Repulsive (steric) particle interactions 16
1.4 Rheological Properties of Thermoplastic Suspensions 20
1.4.1 Rheological properties and droplet jetting 23

2 Materials and Methods **27**
2.1 Preparation of Paraffin-Wax-Based Zirconia Suspensions 27
2.2 Rheological Characterization of Suspensions 30
2.3 Thermoplastic 3D Printing 31
2.3.1 Jetting of droplets with a micro-dispensing system 31
2.3.2 Printing and post-processing of bending bars with different infill strategies 32
2.4 Characterization of Parts Printed by T3DP 34
2.4.1 High speed camera imaging and laser scanning of individual droplets 34
2.4.2 Surface roughness of single layers 35
2.4.3 Properties of bending bars 35
2.4.3.1 Density measurement 35
2.4.3.2 Microstructure and phase analysis 35
2.4.3.3 4-point bending test, Weibull analysis and fractography of sintered bending bars 35

3 Aims and Hypothesis **37**

4 Results **39**
4.1 Composition and Thermal Stability of Suspensions 39
4.2 Rheological Properties of Suspensions 41
4.2.1 Effect of surfactant amount and solid loading on viscosity 41
4.2.2 Effect of steric barrier thickness and conformation on rheological properties 44
4.2.2.1 Viscosity of the suspensions stabilized with various ratios of SA and S3 44
4.2.2.2 Yield stress behavior 47
4.2.2.3 Storage and loss moduli 48
4.2.2.4 Calculating Reynolds number 49
4.3 Jetting Behavior of Individual Droplets and Lines as a Function of Suspension Characteristics 49
4.4 Morphology of Printed Single Layers from Fused Droplets and Lines 52
4.5 Properties of Bending Bars Prepared by T3DP 54
4.5.1 Density measurement 54
4.5.2 Microstructure and phase analysis 55
4.5.3 4-point bending test and Weibull analysis 56
4.5.4 Fractography 57

5 Discussion **61**
5.1 The Role of Steric Barrier Thickness and Conformation on the Flowability and Viscoelasticity of Suspensions Used for T3DP 62
5.1.1 The mechanistic model of steric barrier interactions affecting flowability of suspensions 62
5.1.2 The role of attractive potential magnitude and conformation of steric barrier on the viscoelastic behavior of suspensions 67
5.2 Droplet Jetting Dynamics as a Function of Rheological Properties 69
5.3 The Role of Droplet Deposition and Infill Strategy on the Strength and Flaw Type Population 72

6 Conclusions **77**

References **79**

Bibliography **93**

Biography **95**

List of Figures

Figure 1: Conventional ceramic shaping processes vs AM [10]. 2
Figure 2: Ceramic AM processes and their sub-processes [10]. 2
Figure 3: Schematic on working principles of most common ceramic AM processes [10]....4
Figure 4: Shear modulus and behavior of cross-linked and un-cross-linked polymers [10]. .5
Figure 5: Workflow for preparation and processing of filaments used for ceramic FFF [10]. 6
Figure 6: Infill strategies a) 0°, b) 90° and c) ±45°. 7
Figure 7: Different stages of thermal post-processing [10]. 8
Figure 8: a) 3-point bending test, b) Weibull analysis of rectangular bars prepared by FFF with different infill strategies [50]. 9
Figure 9: Working principle of T3DP [10]. 10
Figure 10: Parameters used for controlling the frequency of droplet deposition [72]. 11
Figure 11: a) Dimensions of an individual droplet, b) droplets fusing together to form lines, c) detailed droplet and line fusion [54]. 12
Figure 12: MMJ of heatable multi-material parts [80]....14
Figure 13: Different configurations of surfactants include a) mushroom and b) brush [119]. 17
Figure 14: Steric barrier interactions [122]. 17
Figure 15: Steric repulsion is the sum of mixing and elastic interactions [121]....18
Figure 16: Relation of potential energy and particle dispersion for a) well dispersed, b) weakly flocculated, and c) strongly flocculated particles [87]. 19
Figure 17: Range of viscosity of feedstocks used for T3DP [73]. 21
Figure 18: Effect of chain length of surfactant on the yield stress [127]. 21
Figure 19: Effect of a) solid loading [138] and b) particle size on the storage and loss modulus [139]. 22
Figure 20: Droplet jetting of a) Newtonian, b) non-Newtonian feedstocks [141]. 23
Figure 21: Formation of a tail on the deposited droplet [142]. 24
Figure 22: Limits of jettability for Newtonian fluids, in terms of We and Re [144]. 25
Figure 23: Structures of a) stearic acid [150] and b) Solsperse 3000® [149]....28
Figure 24: a) HAGE 140 L 3D printer, b) Vermes micro-dispenser attached to 3D printer. 31
Figure 25: CerAM T3DP machine (left) and micro-dispensing system assembly (right) [54]. 32
Figure 26: Schematic of a) bending bars on print bed and bending bars printed with infill strategy b) 0°, c) 90°, d) 0°+ 90° [54]. 33
Figure 27: Heating regimes for a) debinding, b) sintering the zirconia bending bars [54].34
Figure 28: a) Cumulative volumetric particle size distribution, b) scanning electron micrograph and c) optical microscopy image of 3Y-TZP powder used in this study [151]. 40
Figure 29: TG/DTA of a) paraffin wax, SA and S3, b) 100 SA, 50 S3 and 100 S3 [151]. 41

Figure 30: a) Effect of surfactant amount on the viscosity of suspensions containing 35 vol% zirconia at a shear rate of 0.1 s^{-1}, b) Effect of solid loading on the change of relative viscosity with increasing shear rate of the investigated suspensions with optimal surfactant amount (i.e., 1.25 mg/m^2 and 2 mg/m^2 for SA and S3, respectively) [151]..... 43
Figure 31: a) Measurement of viscosity versus shear rate (flow curves measurements) for suspensions with various SA/S3 surfactant content, b) shear stress vs shear rate for suspensions with various SA/S3 surfactant content where symbols represent experimental data and solid lines are fits of Herschel–Bulkley model [151]..... 45
Figure 32: Flow curves with all cycles for a)100 SA, b)15 S3, c) 25 S3, d) 50 S3, e) 75 S3 and f) 100 S3 [151]. 46
Figure 33: Shear stress versus shear strain curves for the following suspensions: 100 SA, 15 S3, 25 S3, 50 S3, 75 S3 and 100 S3 [151]..... 47
Figure 34: The storage (G′) and loss (G″) moduli of suspensions in relation to the temperature decrease [151]..... 48
Figure 35: Droplet formation during jetting with T3DP recorded by high-speed camera [151]. 50
Figure 36: Top and side optical micrographs of deposited droplets from feedstocks: a)100 SA, b)15 S3, c) 25 S3, d) 50 S3, e) 75 S3 and f) 100 S3 [151]..... 50
Figure 37: Droplet diameter versus height with respect to feedstock composition [151].. 51
Figure 38: High-speed camera images presenting single lines formed from fused droplets jetted by T3DP from the following feedstocks: 100 SA, 15 S3, 25 S3, 50 S3, 75 S3 and 100 S3 [151]. 52
Figure 39: Topographical view of single layer squares printed from feedstocks: a)100 SA, b)15 S3, c) 25 S3, d) 50 S3, e) 75 S3 and f) 100 S3 [151]..... 53
Figure 40: Profilometry 3D surface textures with corresponding roughness values of single layer squares printed from feedstocks: a)100 SA, b)15 S3, c) 25 S3, d) 50 S3 and e) 75 S3 [151]. 54
Figure 41: SEM micrograph of polished-and-etched sample with 0° infill strategy [54].. 55
Figure 42: XRD pattern after machining and after regeneration firing [54]..... 56
Figure 43: Weibull plot for 0°, 90°, and 0° + 90° infill strategies [54]..... 57
Figure 44: Fractography results for different infill strategies (from top to bottom: 0°, 90°, and 0° + 90°, from left to right: strong, medium and weak) [54]..... 59
Figure 45: Interaction potential vs steric barrier thickness between particles dispersed in paraffin. 63
Figure 46: The relation of steric barrier thickness with the flow indicators and particle interactions for all suspensions..... 64
Figure 47: Schematic representation of the possible chain interaction: a) rigid, b) overlapping, c) compression. 64
Figure 48: Formation of a monomolecular layer on alumina [171]..... 66
Figure 49: a) Defining the LVER for suspensions 100 SA, 50 S3 and 100 S3, b) temperature sweep in defined LVER conditions for suspensions 100 SA and 100 S3..... 68
Figure 50: Printing demonstrators with one of the “suitable” feedstocks, 75 S3 [151]..... 71
Figure 51: Roadmap for jettability of feedstocks for T3DP. 72
Figure 52: Droplet positioning of 0° infill strategy [54]. 73
Figure 53: Droplet positioning of 90° infill strategy [54]. 73
Figure 54: Droplet positioning of 0° + 90° infill strategy [54]..... 74
Figure 55: Total volumetric population of defects present in a) 0°, b) 90°, and c) 0° + 90° infill strategy. 74
Figure 56: Voids present in alumina 4-point bending bars, prepared by material extrusion [184]. 75

List of Tables

Table 1: Comparison of different AM methods [10].....3
Table 2: Compositions of suspensions with variation in surfactant content [150].....29
Table 3: Properties of zirconia suspensions with 40 vol% solid loading, summarized [150]. 49
Table 4: Sintered densities of parts [54].....54
Table 5: Strength (σ), characteristic strength (σ_0) and Weibull modulus (m) of parts for each infill strategy [54]. 56

Abbreviations

0D	... Pseudo-dimensionless
1D	... 1-dimensional
2D	... 2-dimensional
3D	... 3-dimensional
3Y-TZP	... 3 mol% yttria-doped tetragonal zirconia
AM	... Additive manufacturing
ATZ	... Alumina toughened zirconia
BJ	... Binder jetting
CAD	... Computer aided design
CIM	... Ceramic injection molding
CT	... Computed tomography
dcp	... Direction of crack propagation
DED	... Directed energy deposition
dff	... Droplet fusion factor
dl	... Delay time
DLVO	... Derjaguin – Landau – Verwey – Overbeek
FA	... Falling time
FFF	... Fused filament fabrication
H-B	... Herschel-Bulkley
IKTS	... Institute for Ceramic Technologies and Systems
IM	... Injection molding
JECS	... Journal of the European Ceramic Society
lff	... Line fusion factor
LOM	... Laminated object manufacturing
LPIM	... Low pressure injection molding
ME	... Material extrusion
MJ	... Material jetting
MMJ	... Multi-material jetting
NL	... Needle lift
Oh	... Ohnesorge number
OT	... Open time
PBF	... Powder bed fusion
PIM	... Powder injection molding
Re	... Reynolds number
RI	... Rising time
S3	... Solsperse 3000®
SA	... Stearic acid
SEM	... Scanning electron microscope
SLA	... Stereolithography
STA	... Simultaneous thermal analysis
T3DP	... Thermoplastic 3D printing

TG/DTA ... Thermogravimetric/differential thermal analysis
TZ-3YS-E ... 3Y-TZP powder, not containing binders
We ... Weber number
XRD ... X-ray diffractometer

Chapter 1

Introduction

1.1 Additive Manufacturing of Ceramics

Engineering ceramics are non-metallic, inorganic materials that have been used as device components in many applications such as aerospace, chemistry, medicine, and electronics, due to their favourable properties like high mechanical strength, hardness, good thermal and chemical stability [1], [2]. The geometrical complexity of ceramic devices varies from simple, planar-shape geometries to intricate 3 dimensional (3D) structures. Shaping of ceramics, however, is a complex process, especially in comparison to the shaping of polymers or metals. Ceramics can be shaped in two basic ways: *i*) dry shaping, where ceramic powders are mixed with additives, followed by uni-axial and/or isostatic pressing in the dry powder form, and *ii*) wet forming, where the ceramic particles are dispersed in a solvent, which is then removed by drying or debinding [3]. After powder consolidation, in order to ensure complete densification of the manufactured part, a solid state or liquid phase sintering [4] step is needed, which requires high energy and time input due to high melting temperatures and slow diffusion processes of ceramic materials.

Ceramics have been shaped by the principles of wet forming for thousands of years, traditionally with a potter's wheel [5], whereas nowadays engineering ceramics may be formed by extrusion, slip casting, or tape casting [5] as well as gel casting and freeze casting methods [6]. These conventional wet forming processes were attractive at the time, given their low cost and the ability for high volume production, yet the geometrical complexity of the produced parts was limited. Introduction of powder injection molding (PIM), where a thermoplastic binder system is used to host ceramic powders, paved the way for shaping of near-net ceramic parts with a higher level of geometrical complexity [7], [8]. Subtractive methods such as milling of the dry pressed presintered parts also gained popularity for shaping, especially dental ceramics. Yet, these methods had the major disadvantage of large waste generation [9]. The introduction of additive manufacturing (AM) allowed a big leap in the manufacturing of complex ceramic geometries with minimal waste. While the popularity of AM methods is ever-increasing, conventional methods, which have been used for near-net-shaping of ceramics, still serve as a benchmark for the know-how for slurry preparation, rheological behavior, debinding, and sintering for additive manufacturing processes, as summarized in Figure 1.

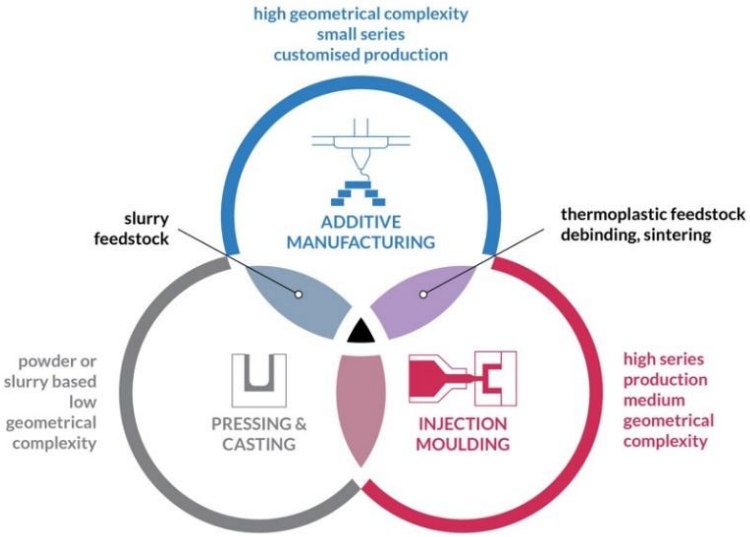


Figure 1: Conventional ceramic shaping processes vs AM [10].

Additive manufacturing, according to the ISO/ASTM 17296 standard, is the "process of joining materials to make objects from 3D model data, usually layer by layer, as opposed to subtractive manufacturing and formative manufacturing methodologies" [11]. In other words, AM is the bottom-up production of near-net-shape parts with complex geometries and functions [10] with minimal waste [12]. The model of the desired part is often prepared by using computer-aided design (CAD) software. This model is then sliced into 2-dimensional (2D) layers using slicer software, which allows for the production of the desired part in a layer-by-layer manner. The first AM process, stereolithography, was invented in 1984 [13] while the first successful AM of ceramics was achieved in 1990 by the binder jetting process [14]. Since then, many different AM processes have been developed for shaping ceramics. While these processes can be classified in many different ways, such as means of deposition (direct vs indirect [15]), in this work, we follow a classification based on the feedstock properties; i.e., powder-based, liquid-based, and solid-based, as summarized in Figure 2.

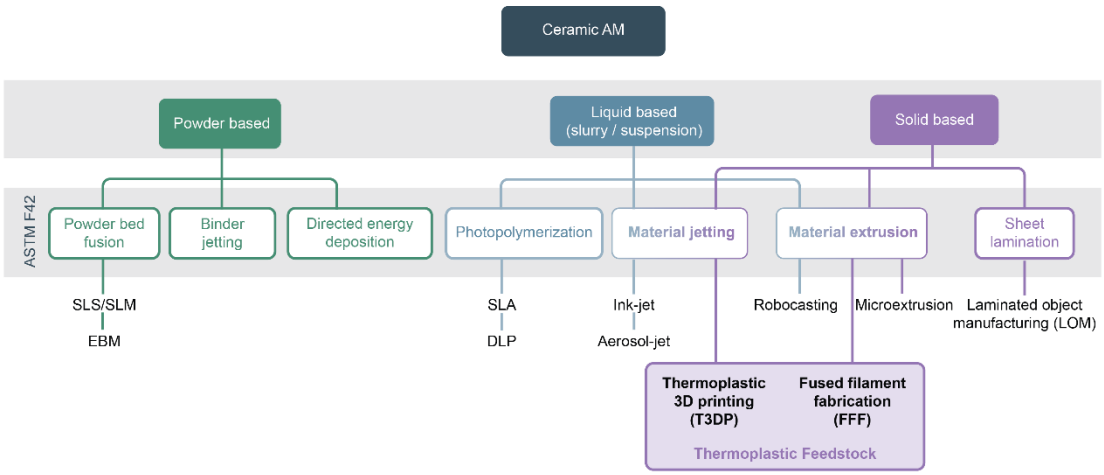


Figure 2: Ceramic AM processes and their sub-processes [10].

Essentially, there are 7 main AM processes that can be used for shaping ceramics: powder bed fusion (PBF), binder jetting (BJ), directed energy deposition (DED), photopolymerization, material jetting (MJ), material extrusion (ME), and sheet lamination [11]. Comparison of some important parameters, such as build volume, resolution, and cost of the above-mentioned AM processes, is presented in Table 1 [10]. The working principles of each of these processes are schematically summarized in Figure 3.

Table 1: Comparison of different AM methods [10].

AM process	**Build volume**	**Resolution**	**Surface quality**	**Cost**	**Examples for used materials**
Binder jetting	10mm-1m [16]	Poor[1]	Poor[1]	Medium	Si_3N_4 [17], Al_2O_3 [18]
Powder bed fusion	10mm-1m [16]	Good (100 μm) [19]	Good[20]	High[20]	Al_2O_3 [21]
Laminated object manufacturing	10mm-1m [16]	Good (100 μm) [22]	Poor [20]	Low[20]	SiC, SiSiC composites, AlN [16]
Photopolymerization	1mm- 0.1 m [16]	Very good (25 μm) [22]	Good[23]	High[20]	Al_2O_3 [24], ZrO_2 [25], SiOC [26], SiAlON [27]
Material extrusion	10mm-1m [16]	Good (100 μm) [22]	Poor[15]	Low[28]	Al_2O_3 [29], yttria-stabilized zirconia [30]
Material jetting	1mm-0.1m [16]	Good [31]	Medium [15]	High [16]	yttria-stabilized zirconia [32], black and white zirconia [33]

Powder bed fusion is a powder-based AM process exploiting the use of laser or electron beam to fuse or partially sinter the ceramic powder, which is kept in a powder bed, in pre-defined positions to ensure production of desired geometries. PBF processes allow good resolution [19] and good surface quality, but are costly [20] as summarized in Table 1. Another powder-based method is **binder jetting**, which relies on the fusion of the ceramic powder with the deposition of the binder in desired locations, and it requires an additional step of curing [34], [35]. Porous parts with high geometrical complexity can be produced with this AM process, while the resolution and surface quality of prepared parts are low [1], [36].

Photopolymerization, or digital light processing, also known as vat photopolymerization, is a highly promising liquid (slurry) based AM process due to good surface finish [23] with a high resolution of 25 μm [22], summarized in Table 1. It relies on the light-activated polymerization of monomers in the ceramic slurry [1], [16]. Despite its advantages, photopolymerization is costly [20], and a lengthy debinding step is required to remove the photopolymer binder [37], [38].

On the other hand, a solid based AM process, **sheet lamination**, also known as laminated object manufacturing, is a process where layers of feedstock are stacked together with a layer of adhesive in between, which is then cut to generate the desired geometry [39]. Parts prepared by this process have good resolution of 100 µm [22].

Material extrusion is possibly one of the most commonly used AM processes, thanks to its low cost [28] and ease of use [40]. During ME, a filament, highly filled with ceramic particles, is deposited continuously on the print bed. The surface quality is low [15] and the resolution is in the range of 100 µm [22] for parts prepared with ME. Fused filament fabrication (FFF) is a material extrusion process where thermoplastic filaments are deposited. Details of this method are covered in the upcoming chapters. Another material extrusion method is robocasting, where an ink is deposited continuously, without being exposed to thermal changes [41], unlike FFF.

Finally, **material jetting**, a type of AM process, that will be the main focus of the present doctoral thesis, is based on the deposition of micron sized droplets of feedstocks on the build platform. The droplet deposition is controlled in order to produce parts with high resolution [31] and medium surface quality [15]. By combining multiple deposition systems, this technique also allows multi-material AM.

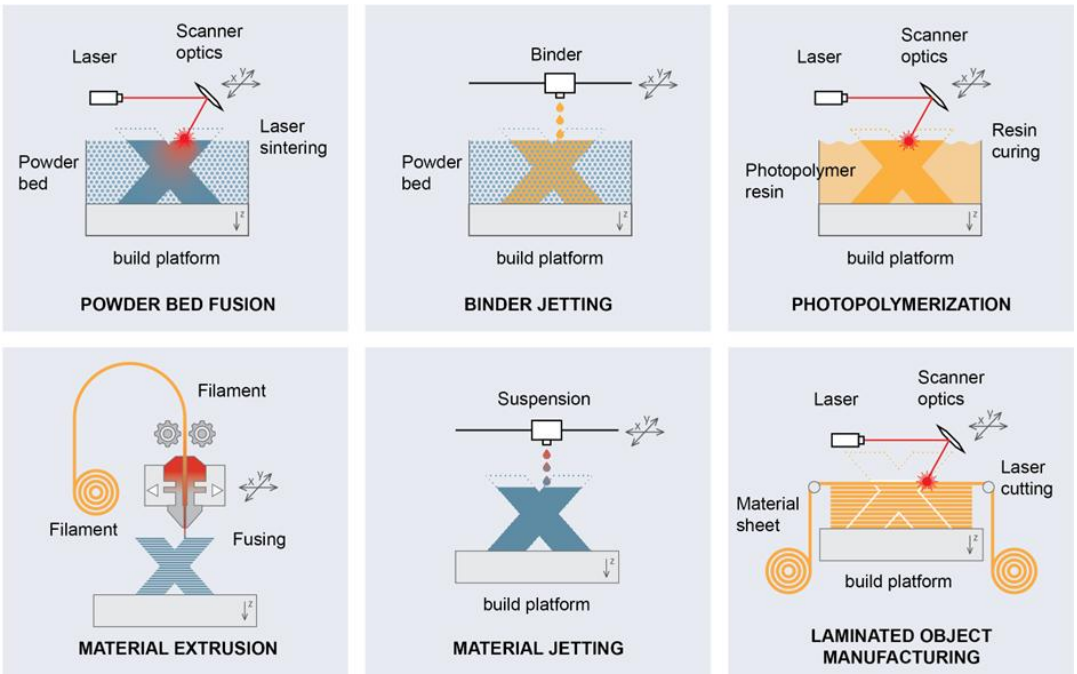


Figure 3: Schematic on working principles of most common ceramic AM processes [10].

1.2 Ceramic AM Processes that Utilize Thermoplastic Feedstocks

Fused filament fabrication and thermoplastic 3D printing (T3DP) utilize thermoplastic suspension-based feedstocks encompassing the knowledge from the processing science and technology of conventional shaping processes, such as ceramic injection molding. FFF is a well-studied AM method, which has similarities to T3DP in terms of not only the thermoplastic nature of the feedstocks but also the building logic of parts. Hence, the extensive knowledge that was accumulated on FFF and low pressure injection molding

(LPIM) of ceramics can be helpful as guidelines for T3DP, a relatively less explored AM process.

Thermoplasticity is a material property where, at elevated temperatures, a transition to a viscous state takes place, while at lower temperatures material is re-solidified [42]. Thermoplastic materials can be heated and cooled down several times without appreciable loss of properties. Thermoplastic materials have a glassy nature below the glass transition temperature (T_g) (Figure 4). As the temperature increases, the material reaches the rubber elastic region, followed by the critical point of melting temperature (T_m), where the material starts to flow. Un-cross-linked polymers (thermoplastics) are subject to changes in their rheological properties (shear modulus) with increased temperature, while the cross-linked polymers (thermosets) are almost insensitive to temperature changes.

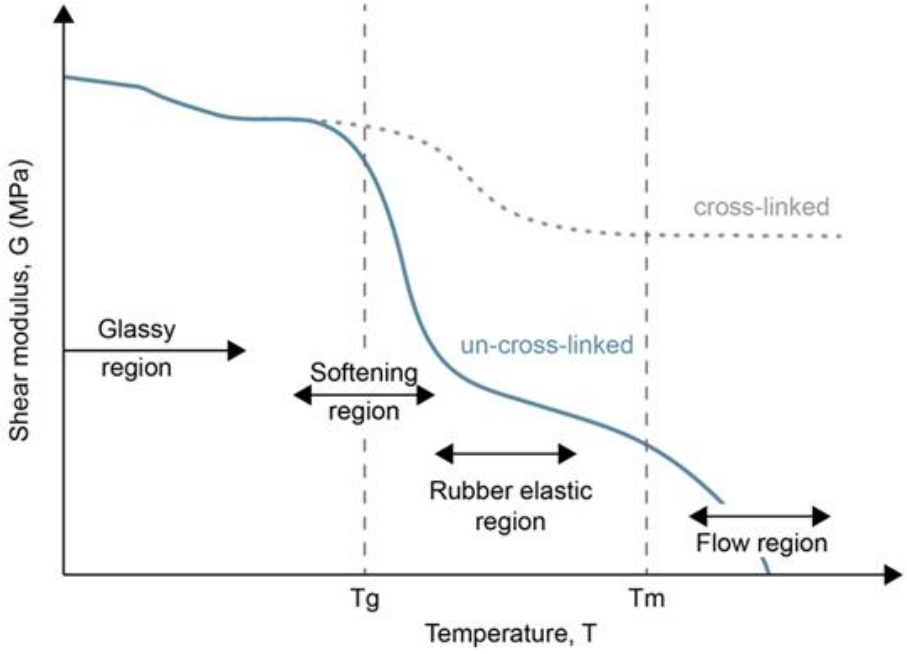


Figure 4: Shear modulus and behavior of cross-linked and un-cross-linked polymers [10].

During ceramic AM, the thermoplastic nature of the material allows transition of the material to a viscous (flowable) or viscoelastic (fluid and solid-like) state at increased temperatures where deposition is conducted, while lower temperatures at the print bed ensure (re)solidification of the material and retention of the formed geometry of the ceramic green body. The thermoplastic nature of the suspensions also ensures a good level of homogenization of ceramic particles.

1.2.1 Fused filament fabrication

Fused filament fabrication is a material extrusion method that relies on the continuous deposition of one-dimensional (1D) thermoplastic filament on the x - y axis of the printing bed/substrate, through a nozzle that is heated up above the melting point of the filament, to ensure moldability. Deposition of a new layer of filament onto the already deposited layer in z axis allows fabrication of 3D geometries. Temperature values lower than the melting point of the filament are used at the print bed to ensure the solidification and preservation of the manufactured geometry (Figure 5).

Fused filament fabrication is used for shaping not only ceramics but also polymers and metals, due to its many advantages, such as low cost, high speed, ease of use, simple design, ability to produce multi-material parts, and low printing temperatures [43]–[46]. With that being said, FFF also has some weaknesses compared to other AM processes, such as lower resolution [22], poor surface finish[15], surface roughness [1], which leads to additional post-processing steps and process-related flaws, such as voids that can appear between deposited filaments [47] that eventually leads to inferior (mechanical) properties.

1.2.1.1 Preparation and properties of filaments

Filaments that are used for ceramic FFF applications are thermoplastic and generally consist of a backbone polymer with a high melting point, a low molecular weight support polymer, and other additives such as surfactants, which are collectively called the binder. In the case of ceramic FFF, the binder is filled with a high solid loading of ceramic particles. All components are homogenised using a kneader or a twin screw extruder [48]. Mixing is followed by granulation and extrusion, commonly done by a single screw extruder [30]. The extruded filament is cooled down and spooled to have the final FFF filament, ready to be used, as shown in Figure 5.

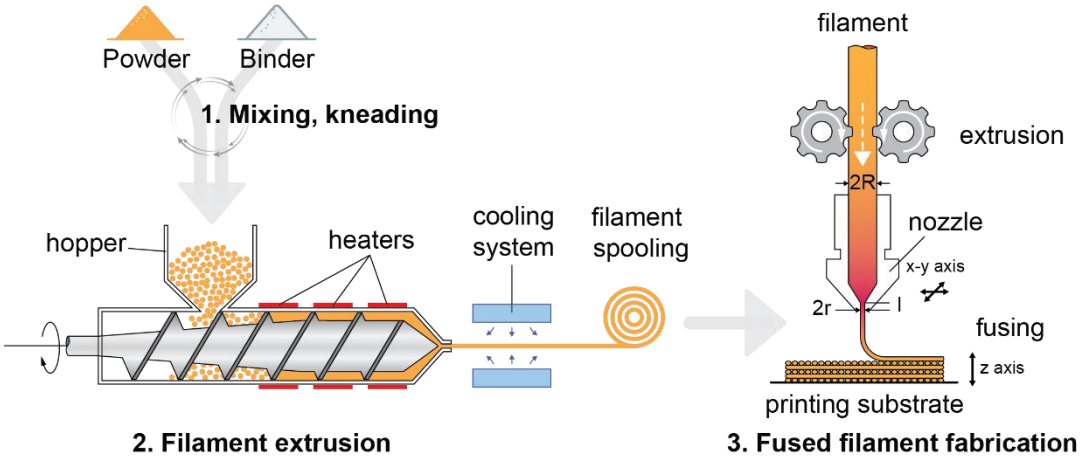


Figure 5: Workflow for preparation and processing of filaments used for ceramic FFF [10].

Filaments used for ceramic FFF commonly have high solid loading of ceramic powder, which is necessary to achieve high sintered densities of the parts. However, there exists a maximum solid loading, which is limited by the rheological properties, such as viscosity and yield stress, as well as the mechanical properties, including brittleness, and the handling and printability of the filaments. The filaments need to show a shear thinning behavior [2], which allows them to be deposited under the high shear rates that they are exposed to during extrusion. Filaments should have a certain level of stiffness to prevent them from buckling in the nozzle during deposition [44] as well as acceptable flexibility for easy handling [49].

Different ceramics with varying solid loading were reported to be used to prepare filaments for FFF. Cano et al. reported preparation of ZrO_2 filaments with 47 vol% solid loading [50] while Nötzel et al. were able to prepare filaments with 50 vol% of ZrO_2 loading [51]. Orlovska et al. reported Al_2O_3 filaments with 50 vol% solid loading [52] while Nötzel

et al. experimented with a wide range of solid loading from 10 to 60 vol% [29]. Xu et al. reported Si_3N_4 filaments with 55 vol% solid loading [53].

1.2.1.2 The infill strategy for filament deposition

As mentioned, during FFF, (1D) filaments are deposited and fused in the x - y axis to ensure the formation of a complete (2D) single layer. A subsequent single layer is deposited onto (and fused with) the existing layer in the z axis to generate 3D objects. The way the filaments in a single layer are positioned with respect to the length of the part is regarded as the infill strategy [54]. There are many possible infill strategies, such as circular, grid, honeycomb, rectilinear, etc. [55], [56], and commonly used rectilinear infill strategies are 0°, 90°, and ±45° [47], [50], shown in Figure 6.

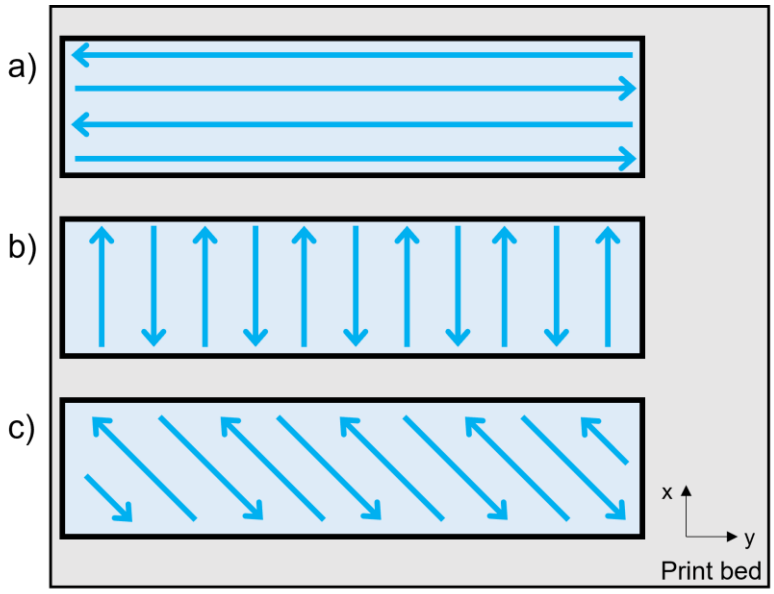


Figure 6: Infill strategies a) 0°, b) 90° and c) ±45°.

It was shown that infill strategies affect the mechanical properties of the parts prepared by FFF, with the 0° infill strategy having better results than the rest [50]. The infill strategy affects not only the mechanical properties of the parts but also the quality of shaping. For example, it was shown that ±45° infill strategy can be used to prevent warping (partial detachment) of the parts from the print bed [57]. The studies on the infill strategies of parts prepared by FFF serve as guidelines for other AM methods, where the deposition is done in a similar manner.

1.2.1.3 Post processing and characterization of printed parts

In order to have high theoretical density and consequently good mechanical properties of the parts prepared by FFF, the binder system has to be removed from the manufactured part by post-processing steps of debinding and sintering, which are graphically summarized in Figure 7. As the binder used in FFF filaments consists of multiple polymers with different properties, often a multiple-step debinding is necessary. Initially, the low molecular weight support polymer is removed with the help of chemical debinding, leading to the formation of pore channels in the part. These channels allow the easy removal of the backbone polymer during the subsequent thermal debinding step at elevated

temperatures. The debinded part is then sintered to achieve high densities, where the temperature is increased to values around 2/3 of the melting temperature of the ceramic powder [58]. During sintering, the surface energy is reduced as the neck formation between particles begins [59], referred to as coarsening, which is followed by densification [60].

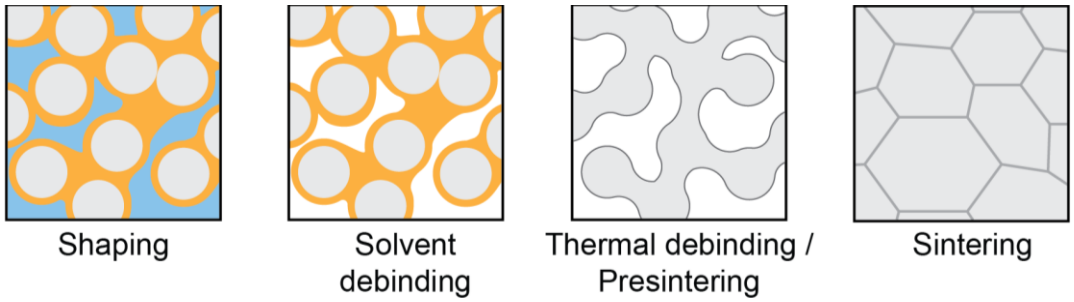


Figure 7: Different stages of thermal post-processing [10].

After sintering, ceramic parts are commonly characterized by their mechanical properties. Flexural strength of parts can be evaluated by tests such as 4-point bending [61], 3-point bending [52] and biaxial strength testing (e.g., ball-on-three-balls) [62]. In order to find the origins of strength-limiting defects present in the ceramic parts, fractography can be used [62], [63]. Furthermore, to evaluate the reliability of prepared ceramic parts, the Weibull modulus is studied [61]. If the data obtained from strength measurements is highly scattered, a low Weibull modulus would be obtained [64], indicating low reliability, while higher values of Weibull modulus indicate higher reliability [65]. Commonly obtained Weibull moduli for ceramics vary from 5 to 15 for advanced ceramics [66].

An example from the literature on the characterization of mechanical properties is presented in Figure 8, where 3-point bending test and Weibull analysis were performed to study the effect of different infill strategies for zirconia parts prepared by FFF [50]. In this study, bending bars were prepared by using 0°, ±45°, and 90° infill strategies. It was shown that parts prepared with 0° infill strategy had the highest characteristic and average bending strength (537 MPa and 512 MPa, respectively) as well as Weibull modulus of 9.9, while parts prepared with 90° infill strategy had the lowest values of all parameters, which was attributed to the formation of pores and defects in the prepared parts.

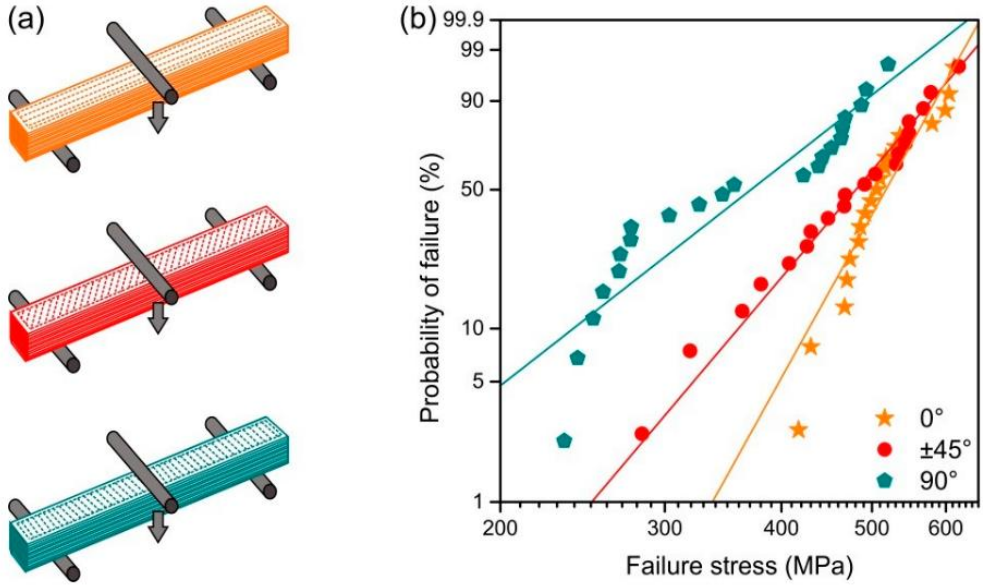


Figure 8: a) 3-point bending test, b) Weibull analysis of rectangular bars prepared by FFF with different infill strategies [50].

The differences in mechanical properties arise from the types of flaws present in the parts. For parts prepared by FFF, the most common flaw types were reported to be pores and voids, which are caused by the sub-optimal fusion of filaments or pre-existing flaws in the filament [50], [51], [67].

1.2.2 Thermoplastic 3D printing

In this work, thermoplastic 3D printing, a drop-on-demand, material jetting process that is recently referred to as multi-material jetting (MMJ) [68], was used. MMJ (T3DP) relies on the deposition of a thermoplastic feedstock, which is usually wax-based, in the form of droplets at a pre-defined frequency, onto a print bed. During the T3DP process, as shown in Figure 9, the ceramic feedstock is kept in a heated cartridge at temperatures above its melting point to ensure flowability during deposition. With the help of applied pressure of maximum 7 bars, a mobile tappet and a piezoelectric micro dispensing system, feedstock is deposited in the form of micron sized, pseudo-dimensionless (0D) droplets at desired positions on the print bed, with controlled frequency and resolution of 0.2 mm in x and y direction and 0.1 mm in z direction [31], [69], [70]. After reaching the print bed, where the temperature is lower than the melting temperature of the feedstock, the droplet solidifies, and the shape of the printed droplets and geometries is retained.

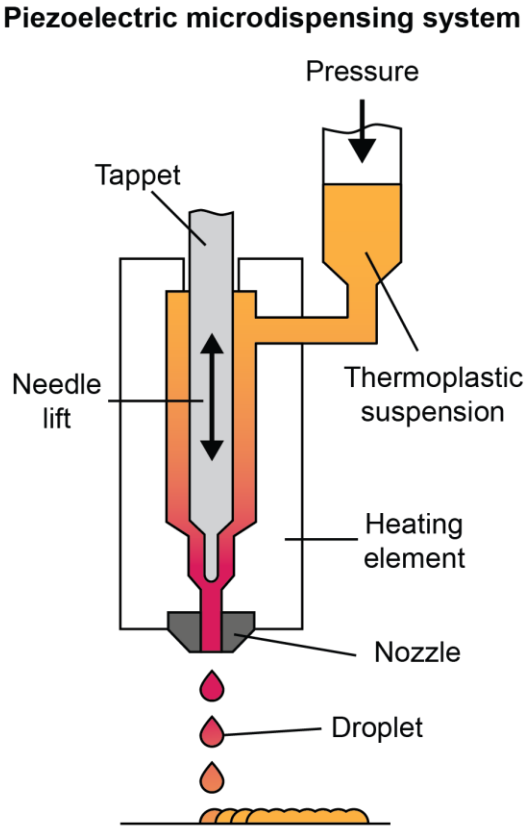


Figure 9: Working principle of T3DP [10].

The frequency of droplet deposition is defined by parameters such as rising time, open time, falling time, and delay time (dl), as shown in Figure 10. Needle lift (NL), which provides energy to the system, is the maximum height that the (needle) tappet reaches and is an important parameter defining the volume of the droplets. The time spent to reach the maximum height of the tappet is the rising time (RI), while open time (OT) is the time needed for filling the gap created under the tappet with feedstock. Falling time (FA) is the time required for the dropping of the tappet, and delay is the time between two cycles [71].

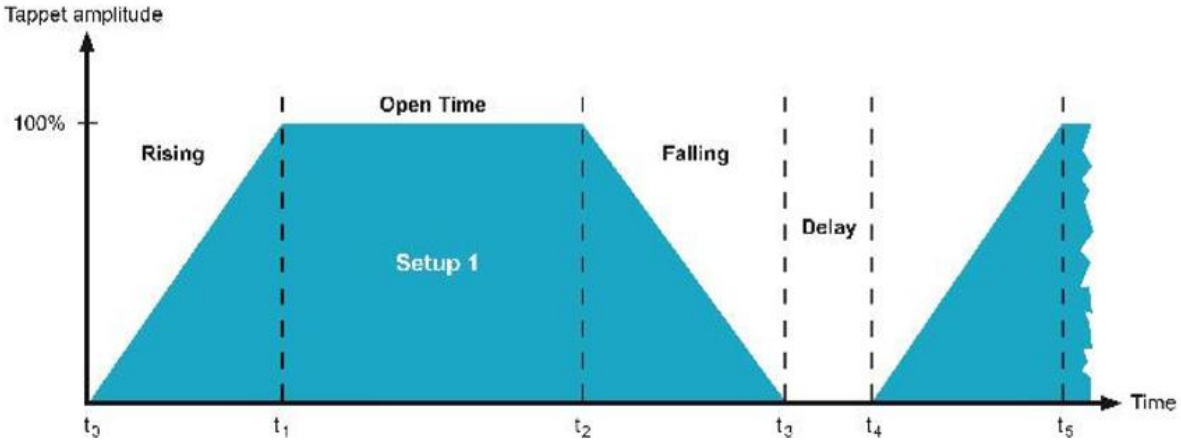


Figure 10: Parameters used for controlling the frequency of droplet deposition [72].

These parameters and travel speed (*tsp*) are used to calculate the frequency of deposition as well as the droplet fusion factor, following Equation 1. It was previously reported that the frequency value of a maximum of 100 Hz can be used for deposition with a T3DP system [73].

$$tsp = (1 - dff) * \frac{d_{char}}{t_{RI} + t_{OT} + t_{FA} + t_{dl}} \tag{1}$$

During T3DP, the feedstock is deposited in the form of (0D) droplets with controlled frequency. Then, more individual droplets are successively deposited at a controlled level of overlap (fusion) to form (1D) lines. The extent of overlap of droplets, which is referred to as the droplet fusion factor (*dff*) (Figure 11b) can be controlled by the speed of the print head, combined with the frequency of deposition, and the diameter of the droplet in the direction of printing ($d_{//}$) (Figure 11a) which is considered as the characteristic diameter (d_{char}), following Equation 1. It was shown previously that, in order to have the formation of continuous lines with minimal flaws, a droplet fusion factor of 50% can be used [74], while another study showed that *dff* of 56–66% was optimal [71] for the formation of lines with constant width.

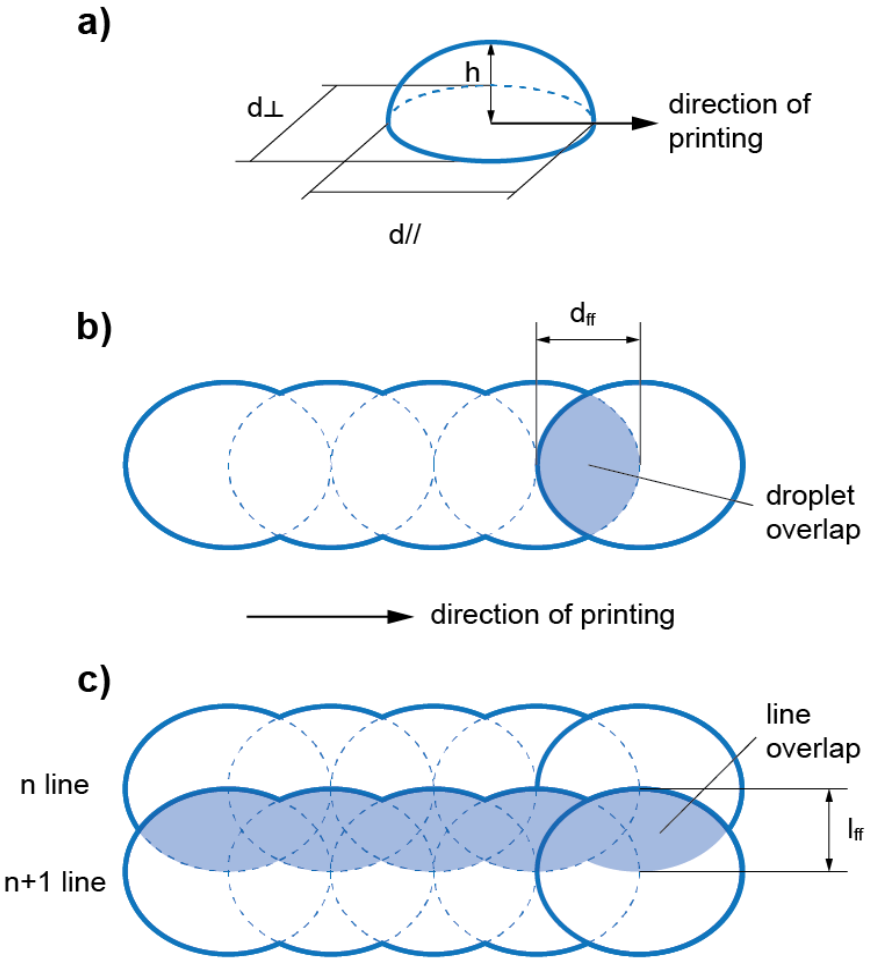


Figure 11: a) Dimensions of an individual droplet, b) droplets fusing together to form lines, c) detailed droplet and line fusion [54].

Once (1D) lines are formed, they fuse further in the z direction to form (2D) layers (Figure 11c) with a controlled level of fusion, known as line fusion factor (*lff*). Finally, these layers are stacked and fused together to form 3-dimensional objects. Similar to FFF, the way the (0D) droplets are positioned in the printed part is considered the infill strategy.

1.2.2.1 Suspensions used for T3DP (and LPIM) ceramic manufacturing

The properties and the preparation of suspensions used with T3DP are very similar to those used for low pressure injection moulding. LPIM is a conventional process used for shaping ceramics under milder conditions than conventional ceramic injection molding (CIM) [7]. During LPIM, the suspension, which is prepared by mixing the ceramic powder with a thermoplastic binder system, is melted at elevated temperatures, injected into the moulds, and cooled down to retain the desired shape. LPIM suspensions are composed of ceramic particles, which are mixed with wax-based binders such as paraffin wax, polyethylene wax, and carnauba wax [75] and surfactants such as carboxylic acids, which provide steric stabilization. The suspensions have low viscosity, allowing processing at low pressure values (below 0.7 MPa [8]). Suspensions used with LPIM were also shown to have shear thinning behavior [76].

The knowledge on the properties and preparation of suspensions, shaping, and post-processing of LPIM serves as guidelines for the novel AM method, T3DP, as summarized in Figure 1. However, a feedstock that was shaped successfully with LPIM will not necessarily be shaped successfully by T3DP, mainly due to differences in the shaping principles of these two processes. Namely, during LPIM, the molten feedstock is directly filled into the hot mold with the help of applied pressure and is not exposed to changes in temperature during the injection part of the process. Afterwards, the part is cooled down and physically removed from the mold. In T3DP, however, as shown in Figure 9, the feedstock is initially at rest in the hot cartridge where temperature is above the melting point of the feedstock. Then the feedstock travels through the hot nozzle, where it is exposed to the highest shear rates and has the minimum viscosity. Here, the kinetic energy from the pressure and tappet, in combination with gravitational forces, overcomes the surface tension to allow extrusion. Once extruded, the droplet is airborne and under no shear stress. During the travel from the nozzle to the print bed, the temperature of the droplets decreases, and the viscosity increases. Finally, when the droplet reaches the print bed, the carried kinetic energy leads to spreading of the droplet, followed by the receding due to surface tension. The droplet is then solidified into its final form.

It can be summarized that, while relying on the existing information from LPIM is useful, it is also necessary to define the unique properties of suspensions that can be used with T3DP.

Suspensions used with T3DP are commonly composed of thermoplastic waxes, ceramic powders, and other additives, such as surfactants. Preparation of the suspensions for T3DP is based on mixing of ceramic powder and other additives into molten wax and homogenization by manual mixing followed by shearing. Waxes such as paraffin wax and beeswax [31], [77], [78] have been reported to be used for the preparation of suspensions for T3DP applications. Suspensions used with T3DP can be prepared using very fine particles [71] and a high solid loading of a wide range of ceramic powders, such as 67 vol% alumina [77], 50 vol% yttria-stabilized zirconia [32], 40 vol% black zirconia and white zirconia [33], Si_3N_4, 40–45 vol% alumina toughened zirconia (ATZ), aluminium nitride (AlN) [79].

While it is possible to manufacture the parts using a single feedstock deposited from a single print head, T3DP also presents the possibility to manufacture parts with multiple materials deposited from multiple print heads, to achieve different properties in a single part [33] as well as in a single layer [71], opening the door to the manufacturing of exciting multi-functional, multi-material composites, possibly mimicking the complex structure of natural materials. In 2015, Scheithauer et al. [85] prepared highly dense ceramic parts from alumina feedstock with 67 vol% solid loading with a binder system composed of beeswax and paraffin wax, as well as from zirconia feedstocks with a solid loading of 45 vol%, which were shaped by T3DP. This study was a milestone for understanding the requirements for limits of solid loading and suspension viscosity, as well as process and post-process conditions for deposition with T3DP. In another study [40], the possibility to manufacture multi-material parts by T3DP was displayed by using feedstocks prepared by ceramic and metal powders. Yttria-stabilized zirconia feedstocks with 50 vol% solid loading and steel feedstocks with solid loading up to 50 vol% were prepared with a binder system composed of beeswax and paraffin wax and used to manufacture a single part. In 2019, Weingarten et al. [41] showed the possibility of producing multi-material and multi-colour ceramic parts by T3DP, using black and white zirconia with solid loading up to 40 vol%. Recently, in 2025, Scheithauer et al. showed the possibility of preparing heatable multi-material ceramic components prepared with MMJ, using Si_3N_4 and $MoSi_2$, as shown in Figure 12.

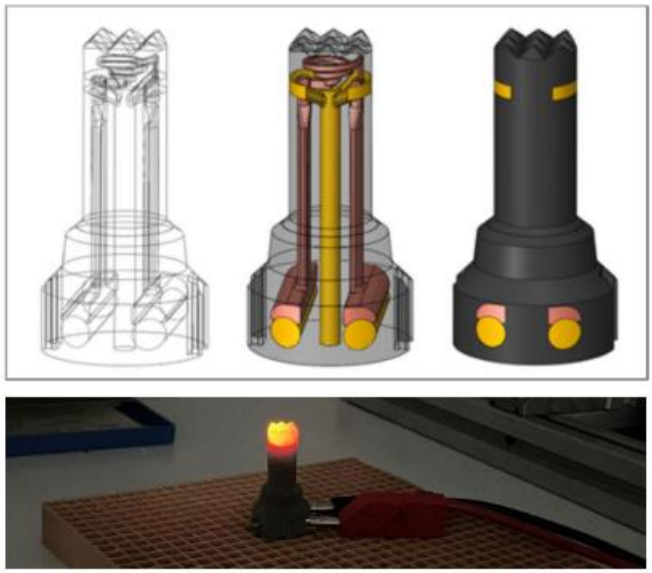


Figure 12: MMJ of heatable multi-material parts [80].

1.2.2.2 Post-processing of parts prepared by T3DP (and LPIM & FFF)

Similar to parts prepared by FFF and LPIM, the parts prepared by T3DP need to be debinded to remove the binder content from the parts and reach high final densities. The debinding of green parts prepared by T3DP is relatively straightforward, as the debinding is achieved through a single-step thermal debinding, similar to parts prepared by LPIM. However, the lack of mechanical support, which is provided by a backbone polymer in the case of FFF suspensions, might lead to the collapse of the parts after debinding [8], [81]. In order to avoid the occurrence of this problem, parts are wick debinded in a high-surface-area powder bed with very fine pores or a porous substrate [8], [82], [83], which provides support to the parts, as well as thermal uniformity, while also ensuring a homogenous capillary extraction of the binder out of the part [8], [84]. Wick debinding also allows using lower temperature values (150–200 °C), compared to thermal debinding [81], [84]. Following wick debinding, parts are sintered to final densities.

1.3 Colloidal Particle Interactions in Thermoplastic Suspensions

While suspensions used with T3DP should have high solid loading to ensure high densities with minimal shrinkage and porosity of sintered parts [76], [85], [86], the increased solid loading leads to increased particle interactions in the dispersing medium, and greatly affects the properties of the suspensions.

Colloidal particle interactions occur when particles within the size range of 10^{-3} to 1 µm [5], [87] are dispersed in an aqueous or non-aqueous dispersing medium, and the behavior of the suspension is dominated by the interparticle forces and Brownian motion, not gravitational forces [5]. The high surface area of colloidal particles results in increased surface interactions.

DLVO (Derjaguin – Landau – Verwey – Overbeek) theory [88], [89] summarizes the overall potential energy of a colloidal system as the sum of attractive van der Waals potential and repulsive electrostatic forces between particles (Equation 2). This equation provides a simplified understanding of particle interactions under the assumption that the particles are spherical [90].

$$V_{TOTAL} = V_{ATTRACTION} + V_{REPULSION} \tag{2}$$

1.3.1 Attractive particle interactions

The attractive interactions of colloids are due to van der Waals attractive forces, which are always attractive between particles with similar dielectric constants [91] and are a result of interactions between oscillating and rotating electric dipoles [92], [93].

Attractive van der Waals forces are formulated in Equation 3, where D is the distance between particle centres, a is the radius of the ceramic particle, and A is the Hamaker constant [94]. It can be seen from Equation 3 that the attractive van der Waals forces exhibit a power law dependence on the interparticle distance.

$$V_{vdw}(D) = -\frac{A(D)}{6}\left(\frac{2a^2}{D^2-4a^2} + \frac{2a^2}{D^2} + \ln\frac{D^2-4a^2}{D^2}\right) \tag{3}$$

Here, it is also important to introduce the retardation effects that arise when the interparticle distance is increased. When the particles are separated by a large distance, the electromagnetic wave propagation, which is the means of interaction of molecules in the neighbouring particles, takes place with a delay [95]. Therefore, when calculating the interparticle interactions, it is important to consider the effect of this delay/retardation by using a distance-dependent Hamaker constant [96].

Hamaker constant indicates the tendency for aggregation or flocculation (coagulation) [90] and its value depends on the dielectric properties of the particles from a given matter and the medium [97]. There are different approaches to calculating the Hamaker constant: initially, in the microscopic approach, the interactions and properties of only two interacting bodies were considered [98], while later on, in the Lifshitz approach, the system was considered as a continuum and the many body effects were taken into account [97].

It can be seen from Equation 4 that the Hamaker constant will be smaller when the Hamaker constant of particle (A_2) is closer to that of the dispersion medium (A_1) [99], i.e., when the dielectric properties of the particles and the medium are similar [100]. Following Equation 3, we can also see that the smaller A will result in a smaller van der Waals attractive potential when the particles and the dispersion medium have similar properties.

$$A = \left(\sqrt{A_2} - \sqrt{A_1}\right)^2 \tag{4}$$

1.3.2 Repulsive (steric) particle interactions

As it is energetically favourable, ceramic particles tend to coagulate and/or flocculate due to attractive interactions; however, this is not desirable from the processing point of view. An ideal colloidal dispersion where particles are stabilized and not agglomerated is needed. Therefore, it is essential to provide energy barriers, in the order of several kT, to prevent the flocculation and have stable dispersions [95]. An energy barrier of a maximum of 1–2 kT was previously defined as a limit for having stable dispersions [100]. Such energy barriers can be introduced by electrostatic repulsion forces. In the case of an aqueous medium, it is common to have electrostatic stabilization, achieved by controlling pH [101], or salt amount [102], leading to the presence of a charged double layer around the particle, and finally, repulsion [103].

While for systems with only electrostatic stabilization, Equation 2 is sufficient to summarize the total interaction energy, when a non-aqueous medium is used, there are other forces that need to be considered. In this case, steric stabilization which is achieved by the adsorption of long chain polymers to the particle surface, helps overcoming the attractive van der Waals forces. When the steric repulsion is taken into consideration, the DLVO theory needs to be elaborated into (extended) X-DLVO theory, shown in Equation 5 [90], [104].

$$V_{TOTAL} = V_{ATTRACTION} + V_{REPULSION} + V_{STERIC} \tag{5}$$

Steric stabilization of ceramic particles has commonly been achieved by the use of surfactants such as carboxylic acids, for injection moulding as well as centrifuge casting suspensions [7], [94], [105]–[109]. Fatty acids (carboxylic acids) anchor to the ceramic particle surface via their carboxylic functional group through acid-base reactions [110], while their hydrocarbon chain is extended into the wax. The attached surfactant and its tail create a steric barrier around the ceramic particle, overcoming van der Waals attractive forces and increasing stability [76], [111]. The molecular weight [112], chain structure and length [113], [114] and the amount of the surfactant are important parameters that define the interaction energy and the final properties of the suspensions.

The surfactants that are used to provide steric stabilization need to be long enough to provide a steric barrier thickness that can keep the particles at a distance where attractive van der Waals forces are not dominant [95], [101]. With that being said, the length of the surfactant should not be too long, as this would result in a larger volume occupied by the particle and consequently a lower maximum solid loading in the dispersing medium [115]. The surfactant is also desired to have a low molecular mass, in order not to cause additional attractive interactions [116]. Surfactant needs to be strongly adsorbed on the particle to prevent desorption [97].

An “optimum” surfactant amount is usually achieved with a complete monolayer coverage of the particle surface, leading to the lowest viscosity values [105], where the interfacial energy between the particles and the dispersing medium is minimum, the yield point is reduced, and the thixotropic behavior is avoided [117]. The amount of surfactant attached to the particle surface, i.e., fraction of surfactant coverage, is known to affect the conformation of the surfactant, which was studied in detail and quantified by de Gennes [118]. Ensuring high coverage of surfactant around the ceramic particle is crucial so that the surfactant polymers can be fully extended in the liquid medium, taking “brush” configuration, shown in Figure 13b, and not collapsing into the “mushroom” configuration, shown in Figure 13a, which would be present in the case of insufficient surface coverage of

the particle with surfactants [97]. If the surfactant is insufficiently covering the ceramic particle surface, particle contact or bridging flocculation might occur [87], [97], resulting in an increase in viscosity.

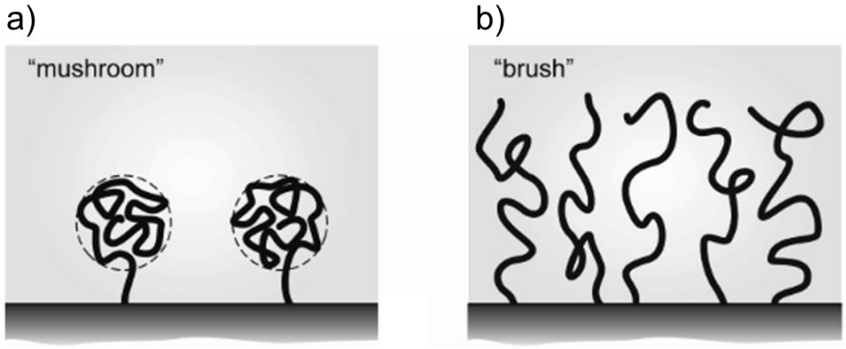


Figure 13: Different configurations of surfactants include a) mushroom and b) brush [119].

When ceramic particles with steric barrier thickness δ, approach each other at a distance (h) smaller than 2 δ, the surfactant chains interact with each other in two possible ways: the chains can overlap (also called interpenetration), or they might get compressed [120], [121] as shown in Figure 14. In both scenarios, the density of polymers in the interaction region is increased, which leads to one of the two possible mechanisms of steric repulsion [122].

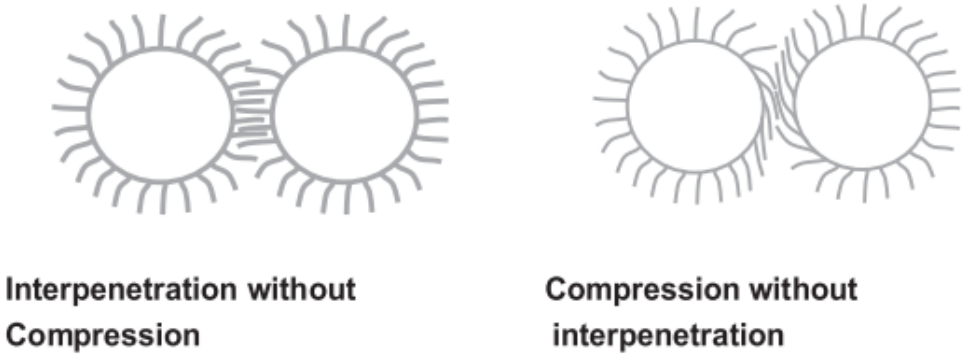


Figure 14: Steric barrier interactions [122].

In the **interpenetration (or overlapping) mechanism**, an increase in the osmotic pressure is observed since the particles come closer than 2 δ [112], contributing to an increased density of polymers in the interaction region. As a result, the liquid medium is "pushed" to the interaction region separating the particles. This is referred to as osmotic repulsion or mixing interaction, and the free energy is presented as G_{mix} [123].

G_{mix} is dependent on the interaction of the surfactant chain with the liquid medium, and can be quantified by the Flory-Huggins interaction parameter (χ). In a good solvent, where the surfactant chain is elongated and relaxed, χ is less than 0.5, resulting in a positive G_{mix} and consequential repulsion of particles. In a poor solvent, on the other hand, where the polymer interacts with itself and collapses [124], the χ is larger than 0.5 [97], resulting in a negative $G_{mix,}$ and the attraction dominates. Free energy of mixing can be calculated by Equation 6, where k is the Boltzmann constant, T is the absolute temperature, h is the

interparticle distance, V_1 is the molar volume of the solvent, V_2 is the molar volume of the polymer and ν_2 is the number of polymer chains per unit area [121].

$$\frac{G_{mix}}{kT} = \frac{2V_2^2}{V_1}\nu_2^2\left(\frac{1}{2} - \chi\right)\left(\delta - \frac{h}{2}\right)^2\left(3R + 2\delta + \frac{h}{2}\right) \tag{6}$$

In the case of **compression mechanism**, the particles come closer than δ [112] and the volume available for surfactant chains in the interaction region is limited compared to the rest of the suspension. It follows that the number of possible configurations and configurational entropy of the surfactant chains in this region is decreased, leading to steric repulsion [121]. This is called volume restriction interaction or entropic interaction, and the free energy is G_{el}. G_{el} is always positive, which means even in poor solvents, steric stabilization of particles can be achieved [122].

Although it was stated previously that in real situations, both of these interactions are present, G_{mix} is caused mainly by the overlapping of surfactants [104] while G_{el} can be present in the case of both compression and overlapping [121]. As shown in Equation 5, the total interaction energy in extended DLVO theory takes into account the repulsion provided by steric interactions, and here we can introduce that the steric repulsion is the sum of G_{mix} and G_{el}, as shown in Figure 15, where G_A is the attractive (van der Waals) energy and G_T is the total free energy of the system.

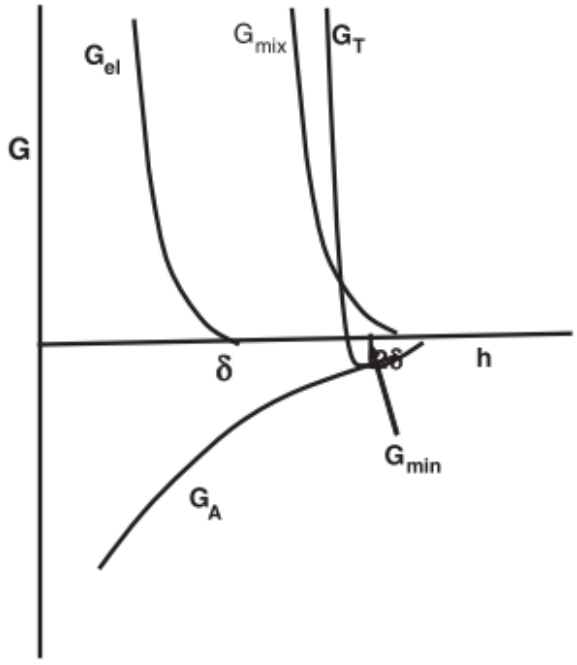


Figure 15: Steric repulsion is the sum of mixing and elastic interactions [121].

One particular carboxylic acid, stearic acid [85], with chain length of 2.4 nm [125], has been a popular choice for steric stabilization of ceramic particles. This is due to its ability to attach to the surface of the ceramic particle with its polar group while spreading its

hydrocarbon chain into the binder [126], forming a steric barrier [111], [127], [128] and consequently improving dispersion [76] while decreasing the viscosity of the suspensions.

The stearic acid was shown previously to provide only partial stabilization of particles, referred to as "semi-steric" stabilization [111], [125]. In this case, due to the short chain length of the surfactant, the effect of van der Waals attractive forces between particles is only reduced, and not prevented completely [116], [127]. The result of this "semi-steric" barrier is a network of **weakly flocculated, non-touching particulate network,** where ceramic particles reside in the secondary minimum where the net potential is attractive (-2 to 20 kT [87]) and there exists a reversible flocculation behavior [5]. The depth of the secondary minimum well, shown in Figure 16b is an indicator of the force that is needed to overcome the attractive forces between particles [101]. Suspension with a weakly flocculated particle system consequently has a yield stress behavior [129], which will be elaborated in the upcoming chapter.

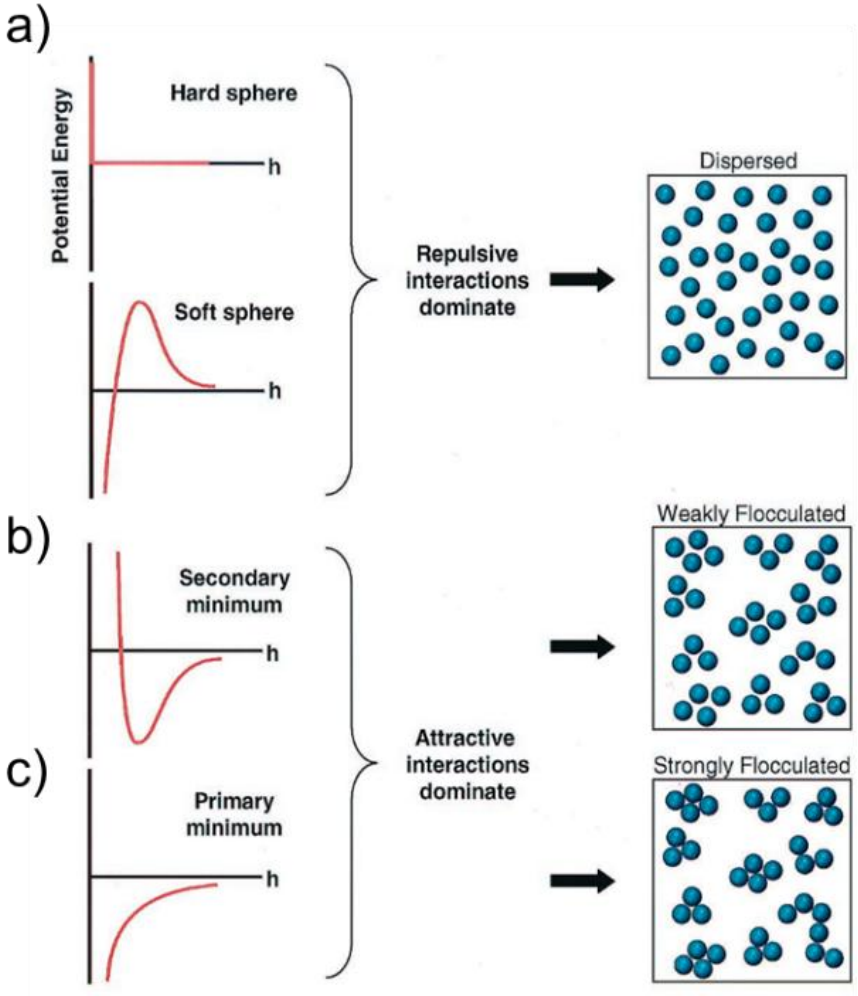


Figure 16: Relation of potential energy and particle dispersion for a) well dispersed, b) weakly flocculated, and c) strongly flocculated particles [87].

When the chain length of surfactants is long enough to overcome the van der Waals attractive forces, a complete steric stabilization is achieved, and particles are **well dispersed** (Figure 16a). In **hard sphere** interactions, the particles only interact at the point of contact [87], where the repulsive forces dominate and increase immediately to infinity [130]. While for **soft sphere** interactions, the repulsive forces are present at a certain distance from the particle surface [87]. On the other hand, if the attractive forces are dominant and not overcome by any means of particle stabilization (i.e., no surfactants are used in the case of non-aqueous suspensions), the particles are **strongly flocculated** at the primary minimum (less than -20 kT [87]) and flocculation is irreversible (Figure 16c) and strong flocculation, also referred to as coagulation [5], occurs, and a **touching particle network** is formed [87].

1.4 Rheological Properties of Thermoplastic Suspensions

During shaping of thermoplastic suspensions, that can be used as feedstocks for T3DP, LPIM and/or FFF, the suspensions in a molten form are subjected to a series of rheological changes, mainly due to differences in temperature and shear rates and in order to optimize each step of shaping, it is crucial to understand how such suspension behaves under these changing conditions of the workflow of a given shaping process.

Rheological properties of T3DP suspensions are analogous in a way to those used for LPIM and FFF. In order to manufacture green body parts with high green densities that allow minimal shrinkage after densification during sintering, high solid loading is required at the lowest possible suspension viscosity [76], [85], [86]. For LPIM suspensions, this requirement is achieved by controlling the colloidal interactions between ceramic particles. As introduced previously, stearic acid is used as a surfactant to ensure steric stabilization of ceramic particles, but due to its short chain length of 2.4 nm [125], the formed steric barrier does not result in an overall repulsive potential energy between particles. Instead, **weakly attractive (colloidal) particle network** is formed where the particles are weakly flocculated under the effect of attractive van der Waals forces, residing in the secondary minimum [5]. Due to these attractive interactions, it follows that [109], [111] LPIM suspensions will exhibit **yield point behavior**, which is the critical yield stress required at which the suspension starts to flow [129], that will provoke a transition from weakly flocculated to fully dispersed state, i.e., "bringing the particles out" of the secondary minimum, when the (shear) stress is applied (during injection or extrusion). While the rheological properties of LPIM suspensions were studied in detail, the rheological properties of suspensions used for T3DP are not yet well understood.

The range of viscosity for suspensions that can be deposited by T3DP was defined previously by Weingarten et al. [33] as viscosity values below 100 $Pa \cdot s$, 20 $Pa \cdot s$ and 1 $Pa \cdot s$ for shear rates below 10 s^{-1}, 100 s^{-1}, and 5000 s^{-1}, respectively [33]. Suspensions that fulfil these conditions for pseudoplastic flow behavior were considered as suitable for the T3DP process (Figure 17). Lower values than those defined would result in jetting problems, such as continuous flow and spattering, while higher values would lead to the collection of feedstock on the nozzle due to increased viscous resistance [131]. The shear thinning behavior of T3DP suspensions displays an order of magnitude lower viscosity values (below 100 $Pa \cdot s$ at 10 s^{-1} [33]) than filaments used for FFF (on the scale of 1000 $Pa \cdot s$ at 10 s^{-1} [49]), attributed to differences in shaping mechanisms of these processes, and the requirements for the depositability of the feedstocks. It was shown that shear thinning behavior (pseudoplasticity) of material jetting feedstocks allows deposition under high shear rates present at the nozzle (on the scale of 10^5 s^{-1} [132]) and maintaining the shape at lower temperatures, after the deposition.

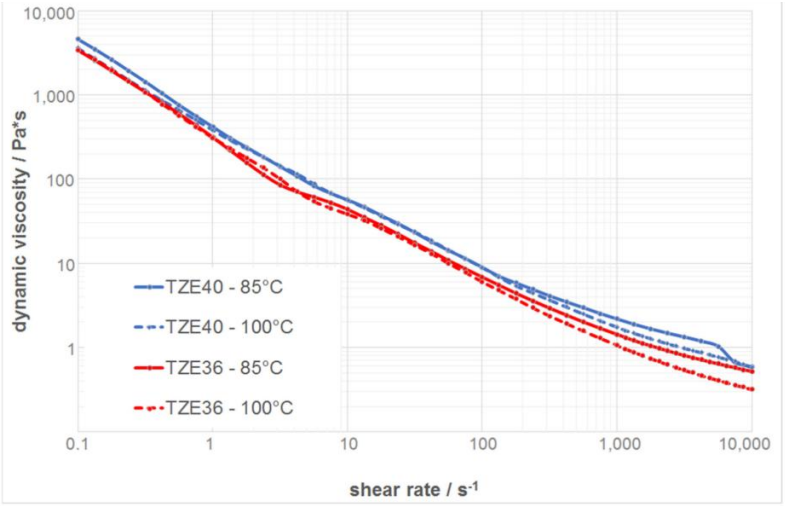


Figure 17: Range of viscosity of feedstocks used for T3DP [73].

Yield stress is the stress that needs to be applied on a system to initiate flow, where the flow behavior changes from elastic (solid) to viscous (liquid) [133]. Yield stress is an important rheological property of suspensions since defining the transition between touching versus non-touching particle network of the weakly flocculated ceramic suspension during shaping. It is known that the yield stress needs to be low enough to allow shaping of the feedstocks [127] and high enough for shape retention during debinding [109]. The value of the yield stress depends on the surfactant amount and length (as shown in Figure 18 for feedstocks with 47 vol% of solids loading of A16 powder, used for LPIM applications), size and amount of ceramic powder, as well as temperature [134].

Although literature exist on the yield stress behavior of thermoplastic feedstocks used for conventional shaping methods, such as LPIM, **it is not yet known** if feedstocks for T3DP should have weakly flocculated particles, thus a weak attractive total potential (secondary minimum) and therefore, have yield point, and if so, what would be its magnitude, further affecting the droplet jetting, deposition dynamics and fusion, as well as shape and dimensions of the printed green body.

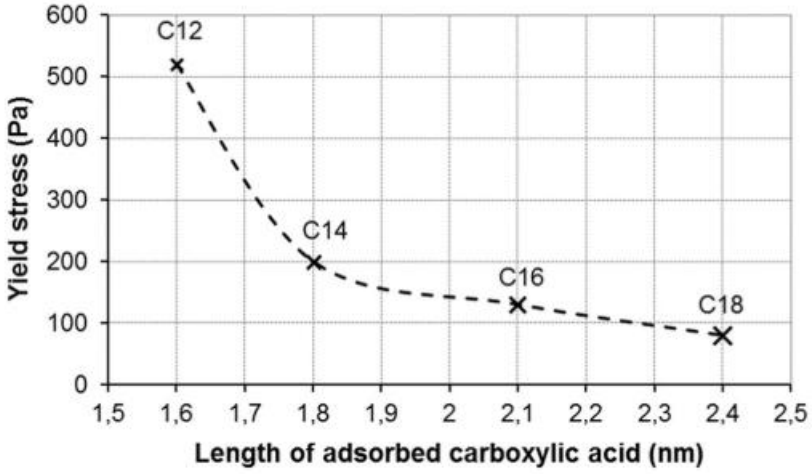


Figure 18: Effect of chain length of surfactant on the yield stress [127].

Viscoelastic materials present solid-like (elastic), as well as liquid-like (viscous) behavior. The time lag (or the phase shift) between the applied stress and the resulting strain indicates the elastic or viscous behavior of the material where phase shift values closer to 90° indicate liquid-like behavior and phase shift values closer to 0° indicate solid-like behavior. Both liquid and solid-like behaviors of viscoelastic materials can be characterized by **storage (G') and loss (G'') modulus**. Storage modulus gives information on the elastic behavior of the material and the stored energy [51], [135] which is used to get back to the initial state of the material when the stresses are removed. Loss modulus gives information on the viscous behavior of the material [136] and is a measure of the energy loss due to internal friction during flow. When the storage modulus is higher than the loss modulus, it can be concluded that the material has solid-like behavior, while a higher loss modulus indicates liquid-like behavior [137], as shown in Figure 19a, where the storage modulus is larger than the loss modulus before the yield point, indicating a solid-like behavior. It is also known that with increased solid loading, the storage and loss modulus increase, as shown in Figure 19, for ceramic inks used in direct ink writing applications.

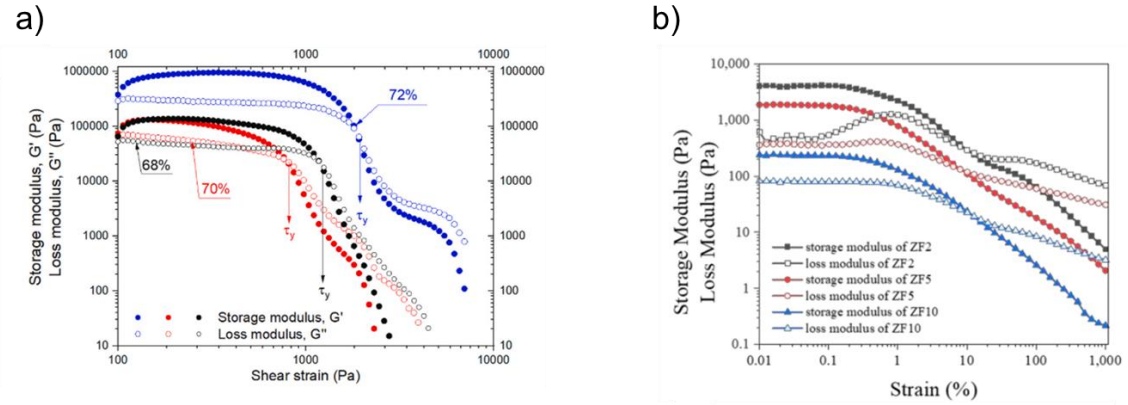


Figure 19: Effect of a) solid loading [138] and b) particle size on the storage and loss modulus [139].

The dependency of storage modulus on particle size was also shown, where the increased particle size resulted in decreased storage modulus, as shown in Figure 19b, for ceramic slurries used for SLA. Furthermore, when surfactants with longer chain length are used, due to increased interparticle distance, the storage modulus decreases [128].

As during the deposition of feedstocks used in T3DP applications, the 3D geometries are built in a drop-by-drop, line-by-line, and layer-by-layer manner, it is crucial that the already printed entities maintain their integrity during deposition of the following layers. Such a condition can be achieved if the storage modulus is higher than the loss modulus [140]. In addition, it is important to focus on the effect of temperature change on the storage modulus of the T3DP feedstock to understand the behavior of the deposited droplets, especially after they are extruded from the nozzle and airborne before being deposited on the printing bed (or on top of the previously deposited droplets or layers) and solidified with the temperature decrease. During this period, the feedstock passes through T_m and T_g (Figure 4). So far, no such study has been reported, and it is aimed to be covered within the scope of this work.

1.4.1 Rheological properties and droplet jetting

As T3DP is a method that relies on the jetting of feedstocks in the form of droplets, it is clearly important to study the connection between rheological properties and the jettability of feedstocks. During T3DP, as the feedstock is subjected to changes in shear stress and temperature during deposition, the rheological properties vary. Ceramic feedstocks used for T3DP have non-Newtonian properties, and here it must be noted that for Newtonian and non-Newtonian fluids, the jetting dynamics and resulting droplets are different, as presented in Figure 20. While for Newtonian fluids the jetting dynamics are well understood, for non-Newtonian fluids, due to changes of properties during deposition, understanding of jetting is more complicated.

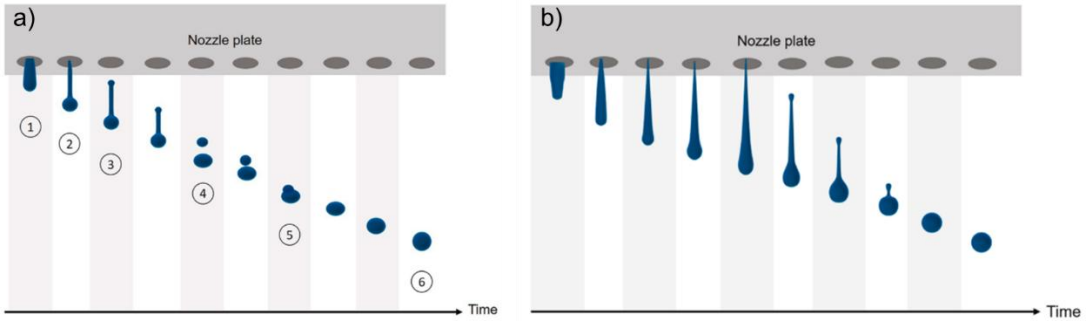


Figure 20: Droplet jetting of a) Newtonian, b) non-Newtonian feedstocks [141].

Differences in the rheological properties, capillary and viscous forces, as well as surface tension of Newtonian and non-Newtonian fluids, lead to differences in the jetting dynamics and droplet formation, as presented in Figure 20. For Newtonian fluids, presented in Figure 20a, droplet deposition starts with a droplet head followed by a short and thick tail. This tail is then separated from the droplet head as a consequence of surface tension, resulting in a following secondary droplet. Finally, these droplets are merged and take the shape of a circular droplet, under the effect of surface tension and arrive to the print bed.

On the other hand, for non-Newtonian fluids, presented in Figure 20b, the jetted material forms an elongated ellipsoidal fluid column, which was explained by higher viscous forces [142]. This column leads to formation of a tail behind the head of the droplet, and depending on the viscosity of the feedstock, this tail may be retracted back in to the droplet similar to Newtonian feedstocks (if surface tension is larger than viscous forces) or can be deposited on the droplet as a bump (if viscous forces overcome surface tension), as shown in Figure 21.

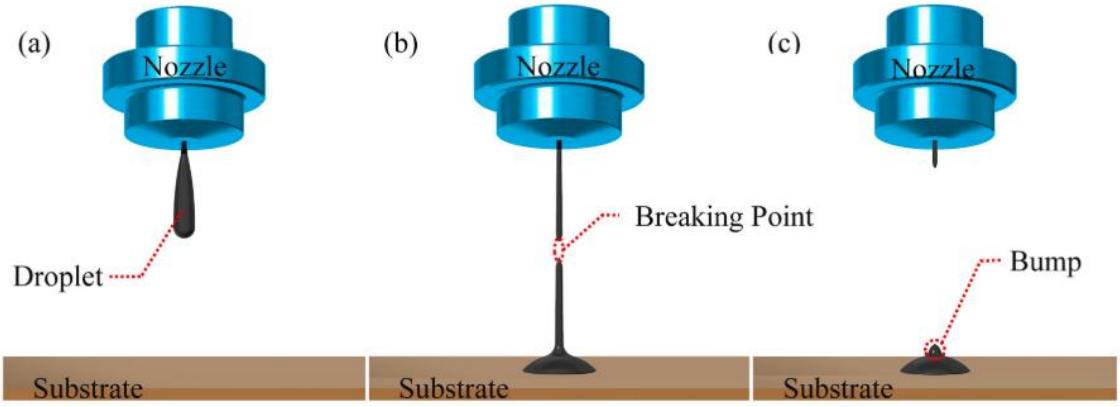


Figure 21: Formation of a tail on the deposited droplet [142].

Dimensionless quantities, Reynolds (Re), Weber (We), and Ohnesorge (Oh) numbers have been used to characterize the behavior of Newtonian suspensions previously, which can be calculated by following Equation 7, Equation 8, and Equation 9, respectively. Here, velocity (υ), viscosity (η), surface tension (γ), characteristic length (a), that is the diameter of the nozzle [143], and density (ρ) are used for the calculations.

$$Re = \frac{\upsilon \rho a}{\eta} \tag{7}$$

$$We = \frac{\upsilon^2 \rho a}{\gamma} \tag{8}$$

$$Oh = \frac{\sqrt{We}}{Re} = \frac{\eta}{(\gamma \rho a)^{1/2}} \tag{9}$$

The Ohnesorge number, Oh, is independent of fluid velocity and is often used for describing the behavior of Newtonian liquid droplets. Furthermore, the parameter $Z = 1/Oh$ was proposed to determine stable drop generation, and the range $1 < Z < 10$ was found for stable drop formation [143]. It was also shown that $Z > 10$ resulted in the formation of satellite droplets, and when $Z < 1$, it was not possible to deposit the feedstock [143], as summarized in Figure 22.

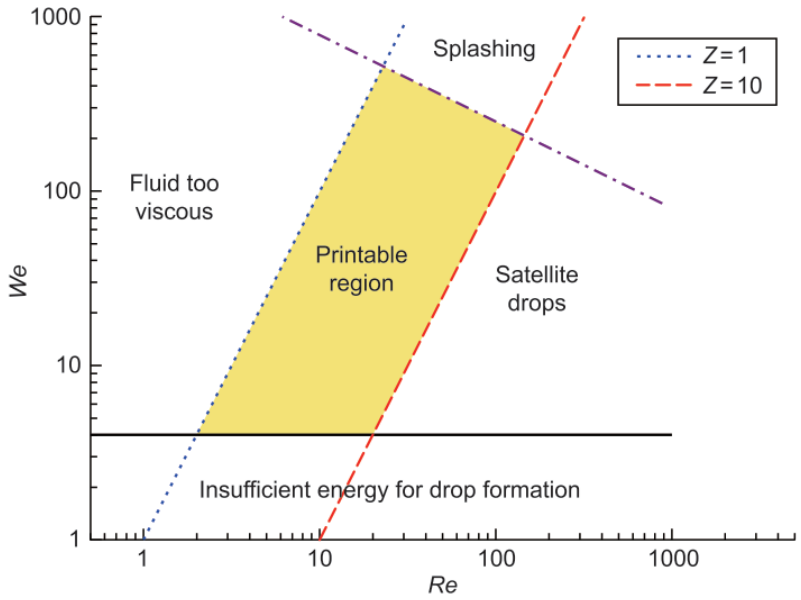


Figure 22: Limits of jettability for Newtonian fluids, in terms of We and Re [144].

Later, the printable range based on Z value was revised considering the jetting frequency, the distance from the nozzle orifice to the substrate, positional accuracy, and formability of the droplet. The vast majority of determined rheological properties were applied to Newtonian fluids, leading to revised printable range expressed by Z value as $4 \leq Z \leq 14$ [145]. While the Z value helps to understand the behavior of feedstocks with low viscosity, it was previously discussed that for highly viscous fluids used for jetting applications, Re explains the behavior during jetting better, as it is the ratio of inertial and viscous forces, which are dominant in the case of such feedstocks [146].

There is a wide range of experimental and simulation-based studies on the droplet jetting of Newtonian fluids, where the viscosity, Re, and We are insensitive to changes in shear rates and are constant throughout the shaping process. For non-Newtonian fluids, which are used with T3DP, however, the viscosity is dependent on the shear rate; therefore, the parameters and limits defined for jetting of Newtonian fluids are not applicable to these suspensions.

Chapter 2

Materials and Methods

2.1 Preparation of Paraffin-Wax-Based Zirconia Suspensions

In the first part of this work, paraffin-wax-based suspensions containing granulated 3 mol% yttria-doped tetragonal zirconia (3Y-TZP) powder, not containing binders (TZ-3YS-E, TOSOH, Japan), were prepared. According to data provided by the manufacturer, this powder has a specific surface area of 7±2 m^2/g, similar to the values obtained by performed BET measurements (6.983 m^2/g), and has impurities of HfO_2, Al_2O_3 ($\leq 0.1 \sim 0.4$ wt%), SiO_2, Fe_2O_3, and Na_2O.

Particle size distribution of the powder was determined with a laser scattering device (LA-920, HORIBA, Japan) by dispersing a small amount of powder into the measuring cell containing distilled water and deflocculant (Dolapix CE 64, Zschimmer & Schwarz Chemie GmbH, Germany). Prior to measurement, a 3-minute ultrasonic treatment with 60% amplitude was applied to break the agglomerates, which was followed by a 5-minute ultrasonic treatment during the measurement.

Paraffin wax (Paraffin wax $T_m > 65$ °C, Sigma-Aldrich, United States) was used as the dispersing medium of the suspensions. Two different surfactants were used in this study. The first surfactant was stearic acid, (SA), ($C_{17}H_{35}$-COOH) (Figure 23a), with an 18C hydrocarbon chain that has a length of 2.4 nm [125]. This surfactant has a molecular weight of 284 g/mol [125]. The second surfactant was a hyperdispersant, Solsperse 3000®, (S3), ($C_{90}H_{172}O_{10}$) (Figure 23b), (Lubrizol, United States), a pentamer of one stearic acid and four 12-hydroxystearic acid [113]. This surfactant has a 66C long chain [147] with the length of 10 nm [148], density of 0.91 kg/m^3 [149] and a molecular weight of 1414 g/mol [109] and was shown previously to result in lower viscosities compared to other surfactants [148]. The orientation of the surfactants was assumed to be perpendicular to the particle surface, as suggested in the literature [94], [125] and the fluctuations of orientation and resulting changes in the steric barrier thickness were considered too small to change the interaction energies and hence were neglected [94].

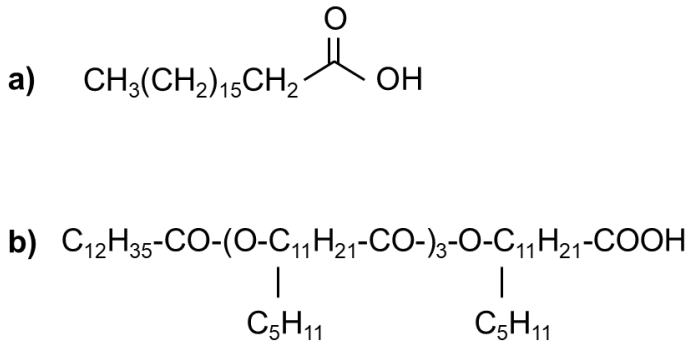


Figure 23: Structures of a) stearic acid [150] and b) Solsperse 3000® [149].

As the first step of suspension preparation, the paraffin wax was heated up above its melting temperature, in a glass beaker. Initially, the surfactant was added to the molten paraffin wax, and the system was mixed with a glass rod. Once all surfactant was dissolved, the desired amount of dried (120 ℃ for 2 hours) zirconia powder was added gradually to the wax solvent containing surfactant, avoiding agglomeration by continuing mixing with the glass rod. When the whole amount of zirconia powder was dispersed, the suspension was homogenized further by 3 roll milling. Suspensions were passed 3 times through a 3-roll mill (EXAKT 3 roll mill 80E, EXAKT Advanced Technologies GmbH, Germany) at 80 ℃ and 300 rpm with a gap size of 5 µm between rollers.

Initially, in order to determine the "optimal" amount of surfactant that results in a monolayer coverage, indicated by the lowest viscosity values, suspensions with 35 vol% solid loading and varying amounts of stearic acid and Solsperse 3000® from 0.75 mg/m^2 to 5 mg/m^2 were prepared. In order to study the effect of solid loading, suspensions with a fixed amount of stearic acid or Solsperse 3000® were prepared, with solid loading varying from 35 to 45 vol%.

Additionally, suspensions with a certain percentage of the optimal amount of each surfactant were prepared in order to study the effect of surfactant chain length, conformation, and particle interactions/flocculation in the suspensions. Exact compositions of suspensions with varying surfactant compositions are collected in Table 2.

Table 2: Compositions of suspensions with variation in surfactant content [151].

Suspension sample label	**Powder loading**	**SA**	**S3**	**SA/S3 ratio**
	vol%	**mg/m²**	**mg/m²**	
100 SA	40	1.25	0	100/0
15 S3		1.06	0.3	85/15
25 S3		0.93	0.5	75/25
50 S3		0.625	1	50/50
75 S3		0.31	1.5	25/75
100 S3		0	2	0/100

Thermogravimetric/differential thermal analysis (TG/DTA) was performed for the individual ingredients of suspensions (paraffin wax, stearic acid and Solsperse 3000®), as well as for selected suspensions (100 SA, 50 S3 and 100 S3), using a simultaneous thermal analysis (STA) instrument (STA 449 C Jupiter, NETZSCH, Germany) coupled with a mass spectrometer (QMS 403 Aëolos, NETZSCH, Germany), for analysis of the gases produced during heating of the samples in the Al_2O_3 crucibles with a heating rate of 10°C/min in argon/oxygen (80/20) atmosphere.

In the second part of this work, a suspension with 40 vol% powder loading was prepared by mixing TZ-3YS-E powder (TOSOH, Japan) with a wax-based binder system developed at Fraunhofer Institute for Ceramic Technologies and Systems (IKTS), in a heated-up dissolver (DISPERMAT CA 20-C, VMA-GETZMANN GmbH, Germany). The components of the binder system were added to the dispersion container and melted at 100 ℃. When binder components were melted and homogenized, the ceramic powder was slowly added to the mixture. Further homogenization of the suspension was achieved by mixing for 6 hours at 100 ℃ and 500 rpm.

2.2 Rheological Characterization of Suspensions

Rheological characterizations of suspensions used in the first part of the study were done by a rheometer (Physica MCR 301, Anton Paar GmbH, Austria) with a cone–plate measuring system using a cone with 25 mm diameter and an angle of 1.994°. The distance between the upper and lower plates was set to 0.051 mm. Before the measurements, the suspensions were pre-sheared at 50 s^{-1} for 5 minutes, followed by at least 1 minute rest. Pre-shearing and the measurements were performed at 100 °C.

Flow behavior of suspensions was determined by measuring viscosity during the increase and immediate decrease (collectively referred to as cycle) of the shear rate in the range 0.1–1000 s^{-1}. 41 points per interval were measured. The measurements of each data point were done every 5 seconds at low shear rates and every 1 second at high shear rates. For each suspension, three cycles of increase and decrease of shear rate were completed.

Yield stress measurements were done in the range of 0.01 to 1000 Pa, while shear strain was recorded. Sharp increase in shear strain values in the plotted graphs was used as an indication of presence of yield point in a suspension.

Herschel-Bulkley model [152], [153] was used to analyse the rheological data obtained from viscosity measurements. This model describes the dependence of the shear stress on the shear rate, summarized by Equation 10, where τ is the applied stress, $\dot{\gamma}$ is the shear rate, τ_0 the yield stress, K is the consistency coefficient (also referred to as "Herschel-Bulkley viscosity"), and n is the flow behavior index, with $n < 1$ for pseudoplasticity [138].

$$\tau = \tau_0 + K\dot{\gamma}^n \tag{10}$$

Fitting of the model curve (maximization of R^2 value) to the experimental data was performed using OriginPro® software using the Levenberg-Marquardt algorithm for nonlinear curve-fitting.

Storage and the loss moduli measurements were done at constant shear strain of 1% and frequency of 1 Hz in the temperature range from 100 °C to 65 °C with 5 °C intervals with a measuring step of 1 min per point. The measurements could not be performed at temperature values below 65 °C, where all suspensions were solidified.

Reynolds numbers for all suspensions were calculated, using viscosity values at a shear rate of 10 s^{-1} and 100 °C. Jetting velocity was calculated using the needle radius (0.75 mm), nozzle diameter (200 µm), nozzle taper angle (90°), and needle speed (0.0144 m/s), following the equation previously defined in the literature for the calculation of droplet velocity [41]. Density values were taken as 2955 kg/m^3 for all suspensions, as the changes in composition did not result in major differences in density.

2.3 Thermoplastic 3D Printing

2.3.1 Jetting of droplets with a micro-dispensing system

In the first part of this work, a 3D printer (HAGE3D 140L, HAGE3D GmbH, Austria) (Figure 24) with 640 x 455 x 400 mm^3 build volume was used as host for the micro-dispensing system (MDS 3280 and MDC 3290+, VERMES Microdispensing GmbH, Germany), that has a maximum working temperature of 180 ℃, and was used for deposition of prepared feedstocks.

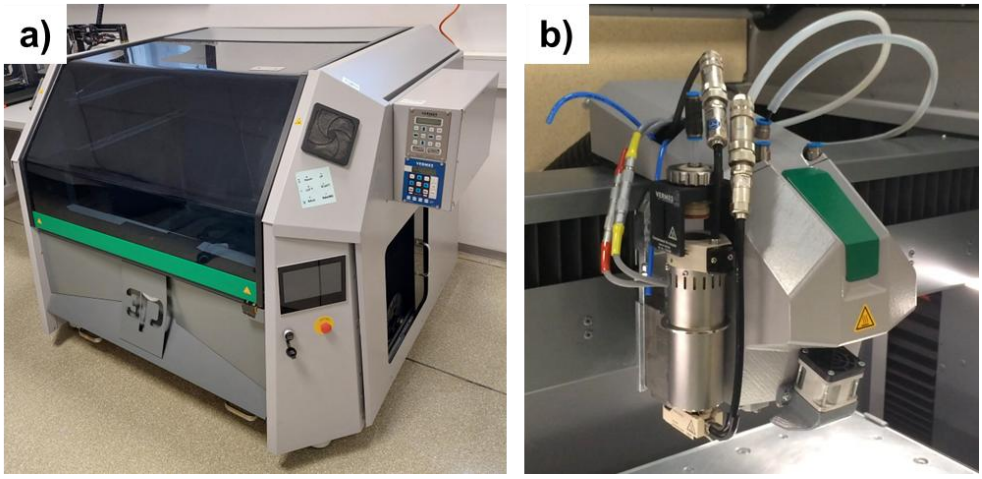


Figure 24: a) HAGE 140 L 3D printer, b) Vermes micro-dispenser attached to 3D printer.

Initially, individual droplets were deposited from all the feedstocks presented in Table 2. In order to control the frequency at which the droplets were deposited, multiple printing parameters that are summarized in Figure 10 were controlled. For all print-jobs, rising time (RT) of 7 ms, open time (OT) of 0 ms, falling time (FT) of 0.32 ms, delay time (DT) of 10 ms, and needle lift (NL) of 50% which resulted in a frequency of 57.7 Hz, were used. Deposition was done at a distance of 1.5 mm between the print bed and the nozzle. A nozzle with 200 µm diameter was used in all experiments. Deposition of droplets was done at a travel speed of 100 mm/s in the x and y directions for all feedstocks.

Single lines and single layer squares were printed from all feedstocks, to observe the fusion of individual droplets, layer consistency, and surface properties. For the printing of single lines and layers, the same printing parameters as the printing of droplets were used. In this case, the travel speed was reduced, following Equation 1 to ensure a droplet fusion of 50%.

2.3.2 Printing and post-processing of bending bars with different infill strategies

In the second part of the study, bending bars with dimensions of 4 × 4 × 40 mm^3 were additively manufactured with T3DP using a feedstock with 40 vol% TZ-3YS-E and wax-based binder system developed at Fraunhofer IKTS. This suspension was prepared during a short mobility stay at the Fraunhofer IKTS, supported by JECS Trust, and the details are limited due to IPR reasons. A micro-dispensing system (VERMES Microdispensing GmbH, Germany) mounted in a CerAM T3DP machine, which was developed by Fraunhofer IKTS (Figure 25) was used for deposition. A nozzle with a diameter of 150 µm was used for printing the parts. Frequencies of 50–60 Hz were used for the deposition, with a nozzle temperature of 110 ℃, cartridge temperature of 100 °C, valve temperature of 30 ℃, and print bed temperature of 50 ℃. All the parts were printed at a speed of 20 mm/s with an applied pressure of 1 bar.



Figure 25: CerAM T3DP machine (left) and micro-dispensing system assembly (right) [54].

A droplet fusion factor and line fusion factor of 0.5 (50% overlap) and 0.6 (60% overlap) were used, respectively. Three different infill strategies, 0°, 90° as well as a combination of those (0° + 90°), were used to prepare the bending bars, as shown in Figure 26. 0° and 90° infill strategies have been commonly used previously for material jetting [154] as well as other AM processes [50] but a combination of these was not reported previously and was explored in this work.

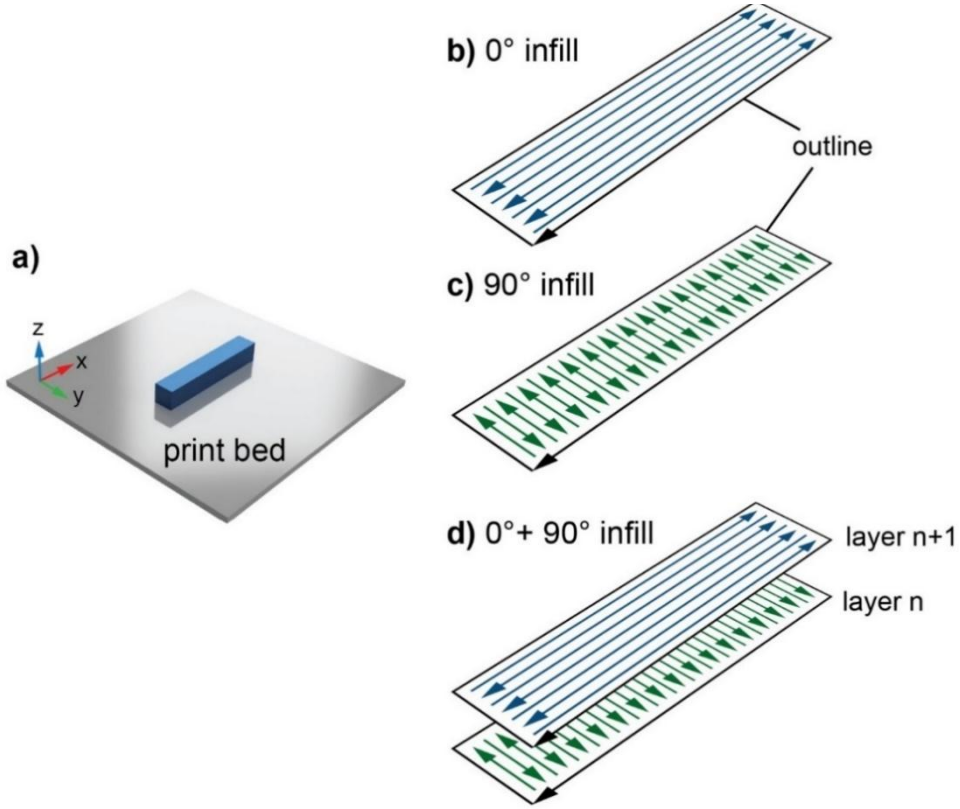


Figure 26: Schematic of a) bending bars on print bed and bending bars printed with infill strategy b) 0°, c) 90°, d) 0°+ 90° [54].

As-printed parts were debinded in alumina powder bed in a chamber furnace (Nabertherm N60, Nabertherm GmbH, Germany), following the heating regime in Figure 27a. After debinding, parts were revealed from the powder bed with the help of an airbrush inside a powder-recycling station (ZD5, Z Corporation, United States). Sintering was conducted in a high-temperature furnace (Nabertherm HT 08/18, Nabertherm GmbH, Germany) following the heating regime in Figure 27b. After sintering, the parts were grinded down to final dimensions of $2 \times 2.5 \times 30$ mm^3 with a surface-grinding machine (Jung Vario-P, Jung GmbH, Germany), making them ready for the 4-point bending tests.

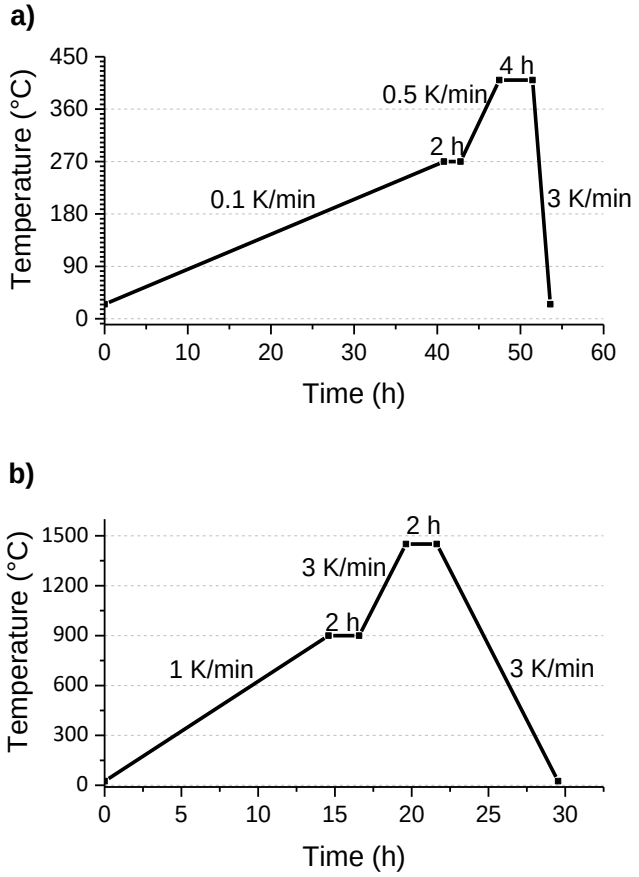


Figure 27: Heating regimes for a) debinding, b) sintering the zirconia bending bars [54].

2.4 Characterization of Parts Printed by T3DP

2.4.1 High speed camera imaging and laser scanning of individual droplets

In the first part of the study, a high-speed camera (FASTCAM Mini UX100, Photron, Japan), with a frame rate of 20000 fps, a shutter speed of 1/frame sec, and a resolution of 1280 x 248, was used to record the droplet and line jetting process. The images were processed on the software (FASTCAM Viewer 4, Photron, Japan). The quality of droplets and their dimensions were analyzed by stereomicroscopy (Discovery V8, Carl Zeiss AG, Germany) and optical microscopy (Zeiss Axio Imager Z1, Carl Zeiss AG, Germany). Diameter of the droplets in the direction of printing ($d_{//}$) as well as in the direction perpendicular to printing ($d_{\perp}$) (Figure 11) were measured.

In the second part of the study, individual droplets were also scanned with a laser scanner (LJ-V7020, Keyence, Japan). The dimensions of the droplets; diameter in the direction of printing ($d_{//}$) and in the direction perpendicular to printing ($d_{\perp}$), as well as the height (h) (Figure 11) were measured and then used to set the slicing parameters in the software, that was specifically developed for the process at IKTS.

2.4.2 Surface roughness of single layers

The surface roughness of printed single layers was measured by a profilometer (Dektak XT Stylus, Bruker, United States) with a 2 µm radius tip and a load of 1 mN. The resolution of 1 µm in the y direction was used to prepare images with 2 x 1 mm^2.

2.4.3 Properties of bending bars

Bending bars were characterized for their density, microstructure, and mechanical properties.

2.4.3.1 Density measurement

The densities of the green bending bars were calculated geometrically, by measuring the weight, width, thickness, and length of all the samples, while for the sintered parts, the density was measured by Archimedes´ method. For this, all samples were weighed when dry. Then, they were placed in distilled water at room temperature, in a vacuum chamber for 1.5 hours to remove the trapped air. Following, samples were first weighed in water, then quickly dried only to remove excess water on the surface and weighed in air. A theoretical density of 6.08 g/cm^3 for zirconia was used in these calculations.

2.4.3.2 Microstructure and phase analysis

Microstructural analyses were performed on selected parts, which were mirror polished down to a 3-µm suspension and etched in air at 1350 ℃ for 20 minutes with a heating rate of 20 ℃/min. The samples were carbon coated (BAL-TEC SCD 005, Gemini B.V., The Netherlands) and analyzed with a scanning electron microscope (JSM-7600F, JEOL Ltd., Japan).

Samples were scanned in the range $2\theta = 27°$ to $40°$ with an X-ray diffractometer (PANalytical X´Pert PRO, Malvern Panalytical, United Kingdom) on their tensile side to determine the crystalline phases. Following the initial XRD measurements, regeneration firing was applied to remove the effects of phase transformation in the parts. For this purpose, samples were heat treated in air, at 1000 ℃ for 15 minutes with a heating rate of 20 ℃/min. The XRD analysis was repeated on the compression side of the samples after regeneration firing to confirm the success of the regeneration firing.

2.4.3.3 4-point bending test, Weibull analysis and fractography of sintered bending bars

Four-point bending tests were performed on 30 samples per infill strategy. Prior to the mechanical characterization, all parts were chamfered on the long edges of the tensile side (the first printed layer, the layer touching the print bed) on a polishing machine (RotoPol-15, Struers, Denmark) using a diamond grinding disc with a grit size of 600. A universal testing machine (Quasar 50, GALDABINI, Italy) with the inner and outer spans of 10 mm and 20 mm, respectively, was used. A crosshead speed was 1mm/min, and the load was 50 kN.

The strength of the parts was calculated using Equation 11, where $\sigma_{\max}$ is the strength (MPa), F is the load at fracture (N), *S1* and *S2* are the distances between the inner and outer spans (mm), respectively, b is the width (mm), and h is the height (mm) of the sample.

$$\sigma_{max} = [3F(S_1 + S_2)]/2bh^2 \tag{11}$$

The results of the 4-point bending tests were analyzed by Weibull statistics. A maximum-likelihood estimation was used to calculate the Weibull moduli with a 90%

confidence interval. The characteristic strength (σ_0) is the strength at failure with a probability of 63.2%.

Finally, fractographical analysis of the samples with the highest, lowest, and medium strength values was made to find the location and size of the origin of the fracture in parts with different flaw populations. The samples were prepared by carbon coating and examined using a scanning electron microscope, as described previously for the microstructural analysis.

Chapter 3

Aims and Hypothesis

T3DP is a relatively new, "zero dimensional" additive manufacturing process based on micron sized droplet jetting of thermoplastic wax-based zirconia feedstocks allowing precise build-up of intricate parts of various ceramic and metal systems, even multi-material components. However, besides being known that the feedstocks should exhibit pseudoplastic flow behavior, the exact nature of interparticle potential and whether suspensions should exhibit weak attractive total potential (secondary minimum) to result in weak flocculation, and therefore a yield point, is not known. In addition, the role of infill strategy on the mechanical properties of sintered ceramic parts is yet to be investigated and compared to other extrusion-based techniques, such as FFF.

The main goal of the doctoral thesis was to study and control the complete workflow of T3DP with a systematic approach in which various rheological properties of ceramic suspensions were analyzed and used to define their printability, setting more complete and concrete guidelines on how the rheological properties of feedstocks affect the printing outcome. **In the first part of the study**, the relation between the surfactant chain length, conformation, and interparticle interactions of ceramic particles as well as the rheological behavior of the suspensions was investigated in detail. Various formulations of paraffin-wax suspensions highly loaded with fine zirconia powder, stabilized by combination of surfactants with significantly different chain lengths, were prepared and used as feedstocks in the T3DP, where their printability, printing process and printed parts were investigated. **In the second part of the study**, wax-based zirconia feedstocks were printed in the form of rectangular bending bars with different infill strategies to understand the effect of infill strategy on the homogeneity of formed bars, the type of flaw populations, final sintered density, Weibull strength distribution, and fractography.

In order to reach the set goals, the following four hypotheses were set.

Hypothesis 1:

It is hypothesised that using combination of surfactants will result in different chain lengths and conformations where chains will be completely stretched or coiled depending on the combination. The particles that are sterically stabilized by combination of surfactants with significantly different chain lengths will display a decay in van der Waals attractive forces around 5 nm, which will affect the rheological properties of the suspensions.

Hypothesis 2:

The feedstocks which can be successfully printed with T3DP will exhibit weakly flocculated ceramic particles that result in pronounced yield point and shear thinning behavior, thus having similar rheological properties to those used for LPIM.

Hypothesis 3:

It is known that feedstocks with high viscosity are not suitable for deposition, as problems such as collecting on the nozzle occur [131]. It is hypothesized that increasing surfactant chain length from 2.4 nm to 10 nm will be required to overcome this problem and have successfully deposited droplets.

Hypothesis 4:

Alternating layers of 0° infill strategy with layers of 90° infill strategy for parts prepared by T3DP will result in higher mechanical strength and reliability (lower number and size of the introduced flaws) than parts with 90° infill strategy only, as layers with 0° infill strategy will serve as strength increasing pillars inside the part.

Chapter 4

Results

4.1 Composition and Thermal Stability of Suspensions

Granulated and binder-free 3Y-TZP zirconia, a well-known and researched ceramic powder from Japanese manufacturer TOSOH, was used. The particle size distribution of TZ-3YS-E zirconia powder was determined by a laser scattering device and is presented in Figure 28a. The measured d_{10}, d_{50}, and d_{90} were 0.21, 0.34, and 0.76 µm, respectively, indicating a relatively fine, narrow, and monomodal particle distribution with a slight tail of larger fractions around 2 µm, extending up to 5 µm. The supporting SEM image shown in Figure 28b reveals agglomerated equiaxed crystallite morphology, with the crystallite size being around 100-150 nm. The powder is granulated (spray dried), but binder-free, and the granule morphology and size were inspected with optical microscopy, as shown in Figure 28c. Granules exhibited spherical morphology and an average size of around 50 µm.

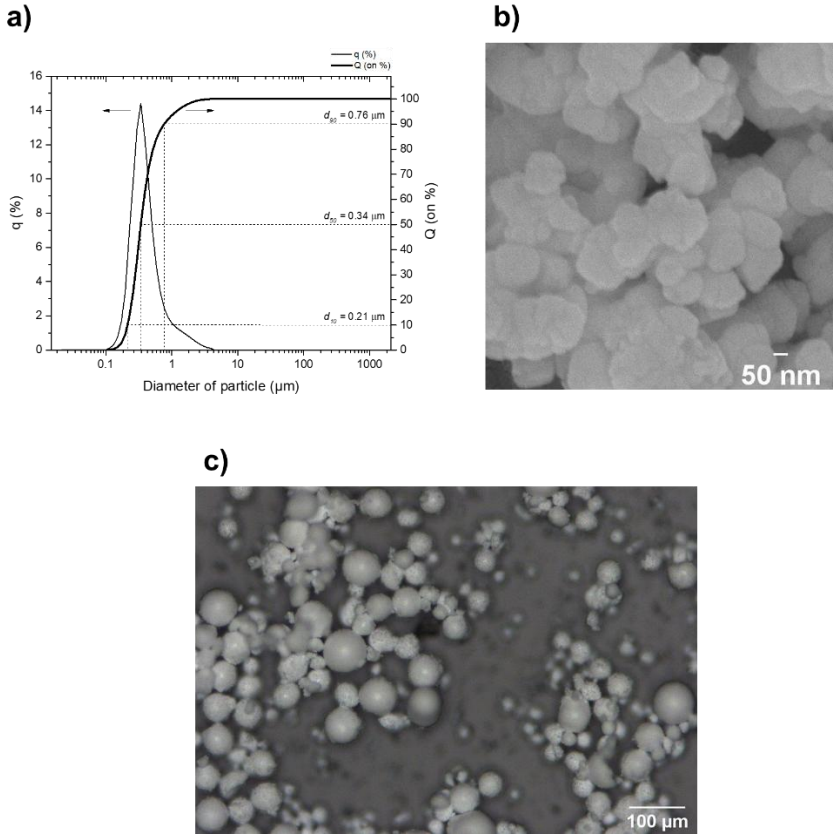


Figure 28: a) Cumulative volumetric particle size distribution, b) scanning electron micrograph and c) optical microscopy image of 3Y-TZP powder used in this study [151].

The thermal stability of the solvent (paraffin wax) as well as that of both surfactants used was evaluated, since the T3DP process can take place at elevated temperatures of 120 °C. The results of TG/DTA for individual ingredients of the suspensions are presented in Figure 29a. It can be seen that for paraffin wax, a peak around 65 °C marked with a black vertical dashed line indicated the melting point, while the DTA peak was observed at approximately 275 °C, and the second peak around 520 °C. While for Solsperse 3000®, the values of the peaks were 350°C and 500 °C. Stearic acid (SA), on the other hand, had a melting point slightly higher than paraffin wax, indicated by blue vertical dashed line and decomposition around 260 °C.

In the next step, suspensions containing a single surfactant or an equal amount of both were analyzed as well. It can be seen in Figure 29b that for suspensions 100 SA, 50 S3 and 100 S3, melting was dominated by paraffin wax. The onset of decomposition indicated by dashed lines showed that suspension 100 SA had the lowest decomposition temperature, while suspension 100 S3 had the highest, as expected based on the TG/DTA results of individual components. These results indicate that neither the individual components of the suspensions nor the suspensions themselves decomposed at the temperature values that were used during characterization and processing by T3DP.

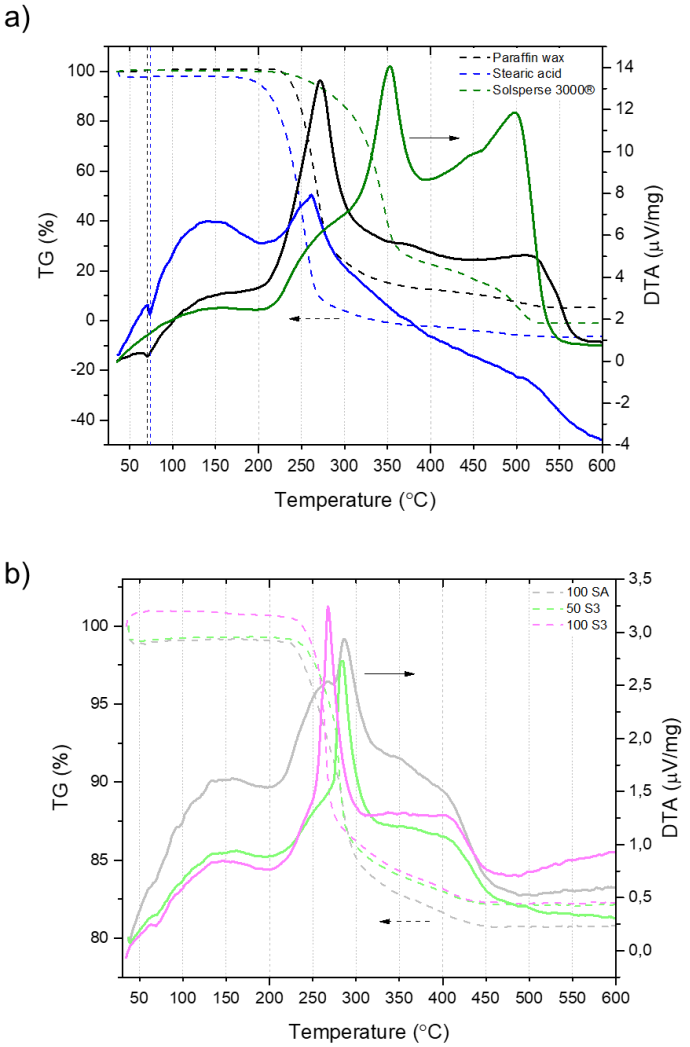


Figure 29: TG/DTA of a) paraffin wax, SA and S3, b) 100 SA, 50 S3 and 100 S3 [151].

4.2 Rheological Properties of Suspensions

4.2.1 Effect of surfactant amount and solid loading on viscosity

The effect of surfactant amount on the viscosity of the suspension at a constant shear rate of 0.1 s^{-1}, with zirconia dispersed into paraffin wax containing either stearic acid (SA) or Solsperse 3000® (S3), is presented in Figure 30a. A minimum viscosity was achieved for 1.25 mg/m^2 and 2 mg/m^2 for SA and S3, respectively, which provided monolayer coverage of adhered surfactant for its "optimum" amount. For SA amounts from 1.25 to 2 mg/m^2 the minimum viscosity (45 $Pa \cdot s$) increased with increased surfactant amount as when more surfactant was added to the system than the optimum amount, the "extra" un-adsorbed surfactants resulted in an increase in viscosity, due to cross-linking of polar ends of un-adsorbed surfactants in the dispersant medium [105] or due to the interactions of surfactant and dispersion medium [113]. Further increase in the SA amount did not cause any changes in viscosity. In the case of Solsperse 3000®, for 2 mg/m^2, which is the recommended amount by the manufacturer, the measured viscosity was lower (the suspension was visibly thinner), i.e., 1.5 $Pa \cdot s$, and further addition of surfactant did not

affect the viscosity. For both surfactants, when amounts less than the "optimum" value were used, due to insufficient coverage of particle surfaces, van der Waals attractive forces were able to dominate, resulting in particle coagulation and increasing viscosity [155]. These trends were similar to those that were previously reported by Zurcher et al. [113] for zirconia suspensions prepared with stearic acid and Solsperse 3000®.

In the next step, the effect of solid loading on the change of relative viscosity with the increasing shear rate (flow curve behavior) of the suspensions with a constant surfactant amount is presented in Figure 30b. As expected, viscosity was almost linearly correlated to solid loading for suspensions with both of the surfactants. On the other hand, flow behavior was different for suspensions stabilized with SA or S3. For suspensions dispersed with 1.25 mg/m^2 of SA, a discontinuous, non-monotonous flow behavior was observed. The initial pseudoplastic (shear-thinning) flow behavior was followed by a dilatant (shear thickening) behavior at shear rate of approximately 10 s^{-1}. The shear thickening was followed by shear-thinning behavior, which continued until the end of the measurement range. For suspensions dispersed with 2 mg/m^2 of S3, a minimal shear thinning behavior (pseudo-Newtonian) was observed, where the viscosity was less sensitive to the changes in shear rate.

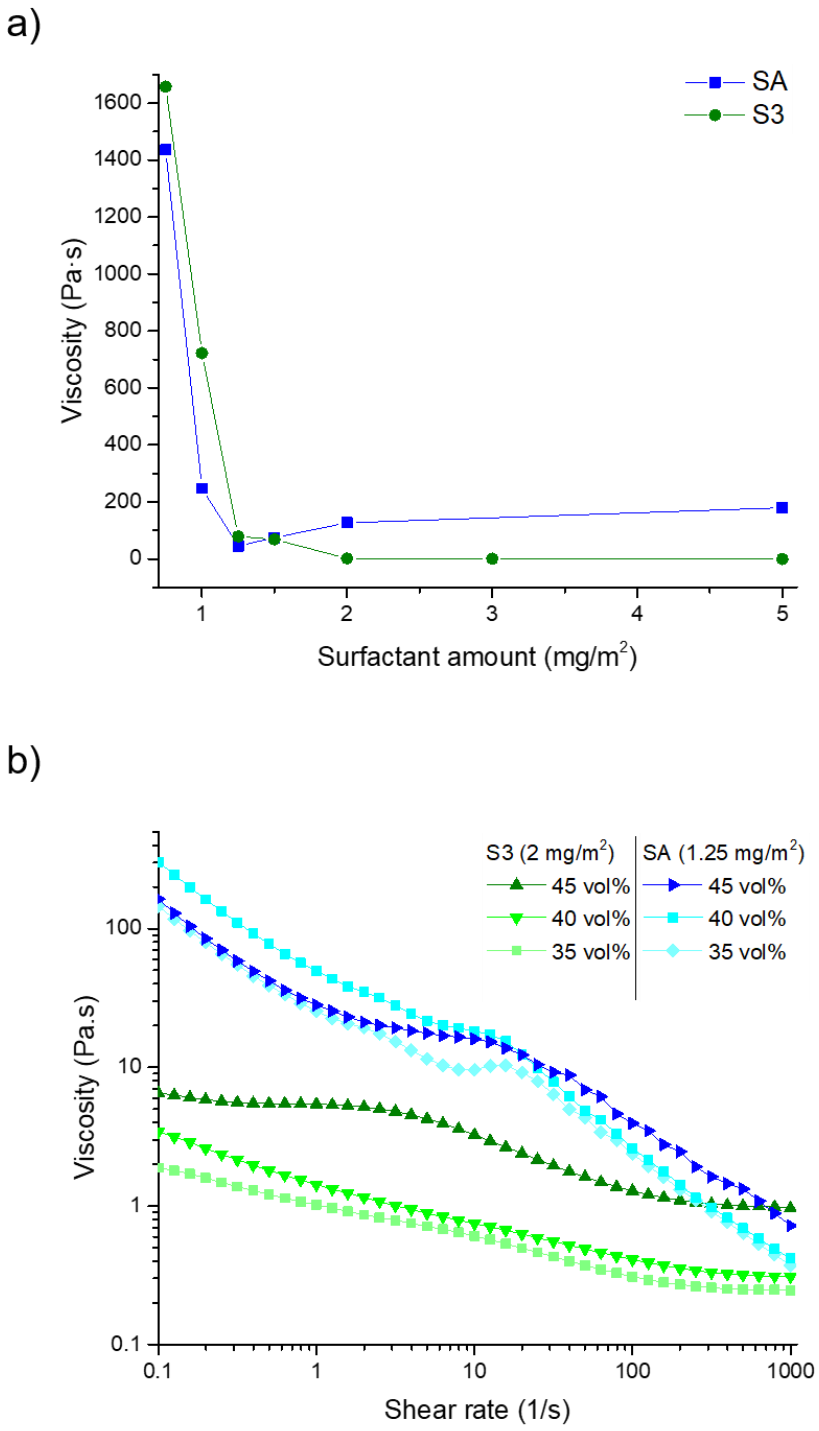


Figure 30: a) Effect of surfactant amount on the viscosity of suspensions containing 35 vol% zirconia at a shear rate of 0.1 s^{-1}, b) Effect of solid loading on the change of relative viscosity with increasing shear rate of the investigated suspensions with optimal surfactant amount (i.e., 1.25 mg/m^2 and 2 mg/m^2 for SA and S3, respectively) [151].

4.2.2 Effect of steric barrier thickness and conformation on rheological properties

Suspensions with combined surfactants (presented in Table 2) were characterized for their rheological properties such as viscosity, yield stress, and loss/storage moduli, and the results are presented in this chapter.

Since the surfactants Solsperse 3000® and stearic acid are known to have almost the same solvency [117] with the dispersing medium, i.e., paraffin wax, which is a non-polar straight-chain hydrocarbon [99], it was possible to evaluate and compare the behavior of suspensions where particles were stabilized with single and combined surfactants.

4.2.2.1 Viscosity of the suspensions stabilized with various ratios of SA and S3

All the prepared suspensions exhibited a shear thinning behavior in the measurement range of shear rates from 0.1 to 1000 s^{-1}. Increasing the S3 ratio resulted in a decrease of viscosity, and a maximum of 2 orders of magnitude difference at low shear rates (500 vs 3 $Pa \cdot s$ at the initial shear rate of 0.1 s^{-1}) with suspensions that had S3 and SA only (Figure 31a).

When the SA ratio in the suspension was high, i.e., 100 SA and 15 S3, a discontinuous, non-monotonous flow behavior was observed, similar to suspensions dispersed with stearic acid at different solid loading values (Figure 30b). When suspensions had more than 25% of S3, a continuous, monotonous pseudoplastic behavior throughout the increasing shear rate range was observed. A pseudo-Newtonian behavior was observed when the ratio of S3 was increased, especially prominent at higher shear rates. It is important to note that due to their shear thinning behavior, the suspensions with high SA amount (100 SA and 15 S3) had lower viscosity values than other suspensions at high shear rates of 1000 s^{-1}.

The obtained flow curves were fitted by the Herschel-Bulkley (H-B) model (Figure 31b), commonly used for suspensions with high solids loading, which typically exhibit shear thinning and yield stress behavior [156], [157]. H-B model was applied to determine the fitting parameters (τ_0, K, n) for the suspensions with higher S3 content (R^2 values >0.99) (Figure 31b). For suspensions 100 SA and 15 S3, the maximum R^2 values were 0.97 and 0.92, respectively, indicating a poor fit of experimental values to the H-B model, possibly due to the non-monotonous behavior. All suspensions were characterized by a shear thinning behavior, as indicated by the flow index, which varied from a lower value for suspensions containing higher SA, suggesting pronounced pseudoplastic behavior, up to $n = 0.93$, indicating nearly Newtonian flow behavior for suspension 100 S3. A decrease in the consistency coefficient K was observed with increasing S3 ratio, which was in accordance with the lower viscosities obtained for these suspensions (see Figure 31a). Observed K values were significantly lower than the values of ~440, reported for highly loaded ATZ pastes that were used for direct ink writing, calculated by Ostwald-de Waele power law equation [158].

In order to examine whether the suspensions were well homogenized and the particles dispersed during the three-roll milling and pre-shearing prior to the measurements, cyclic measurements with increasing and decreasing shear rates were performed. Flow curves with three cycles of increased and decreased shear rates are presented in Figure 32. As can be seen, the flow curves for the majority of suspensions were repeatable, not exhibiting hysteresis loops, indicating that they were well homogenized. As the ratio of S3 was increased, a less pronounced thixotropic behavior was observed, corroborating observations from Figure 31a.

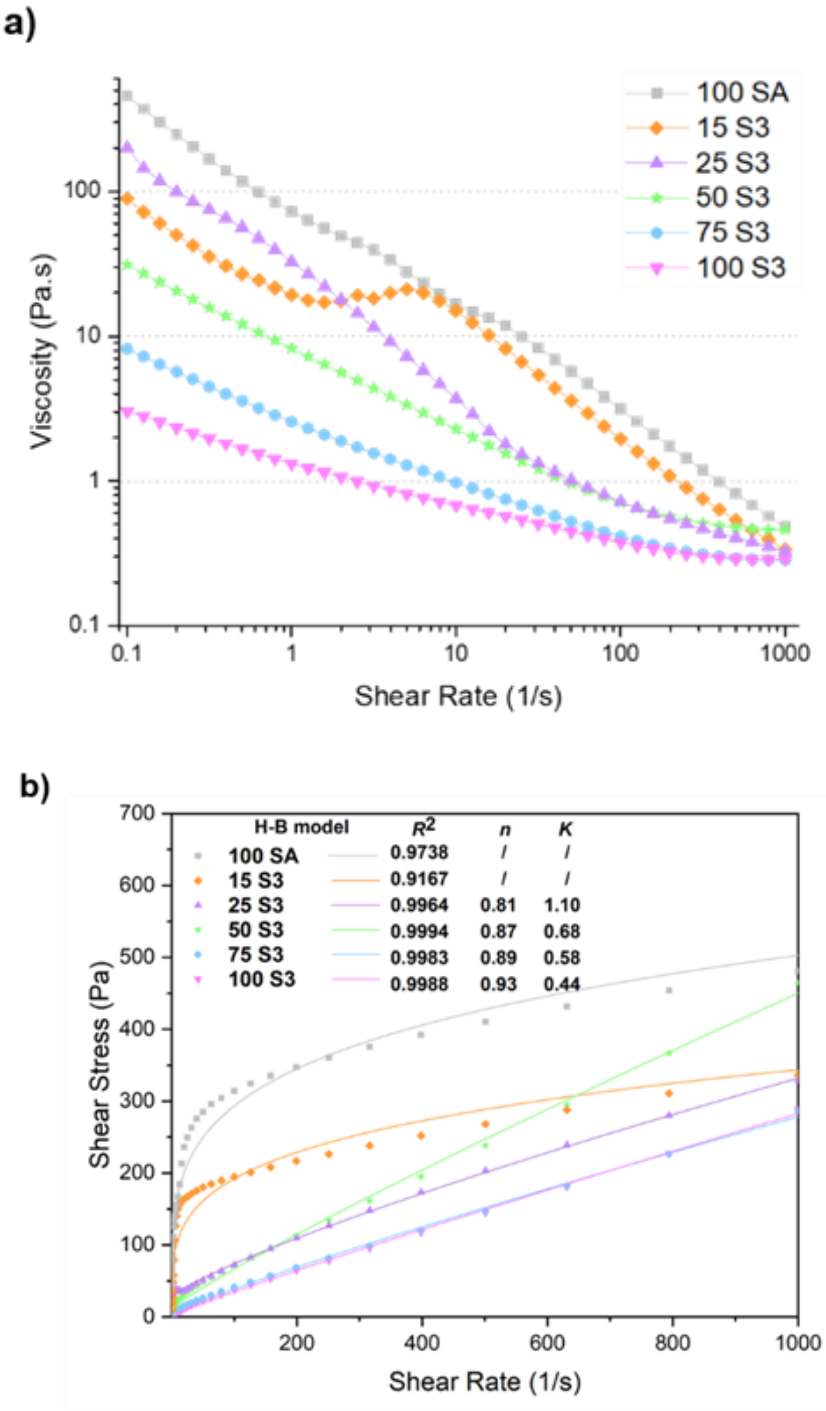


Figure 31: a) Measurement of viscosity versus shear rate (flow curves measurements) for suspensions with various SA/S3 surfactant content, b) shear stress vs shear rate for suspensions with various SA/S3 surfactant content where symbols represent experimental data and solid lines are fits of Herschel–Bulkley model [151].

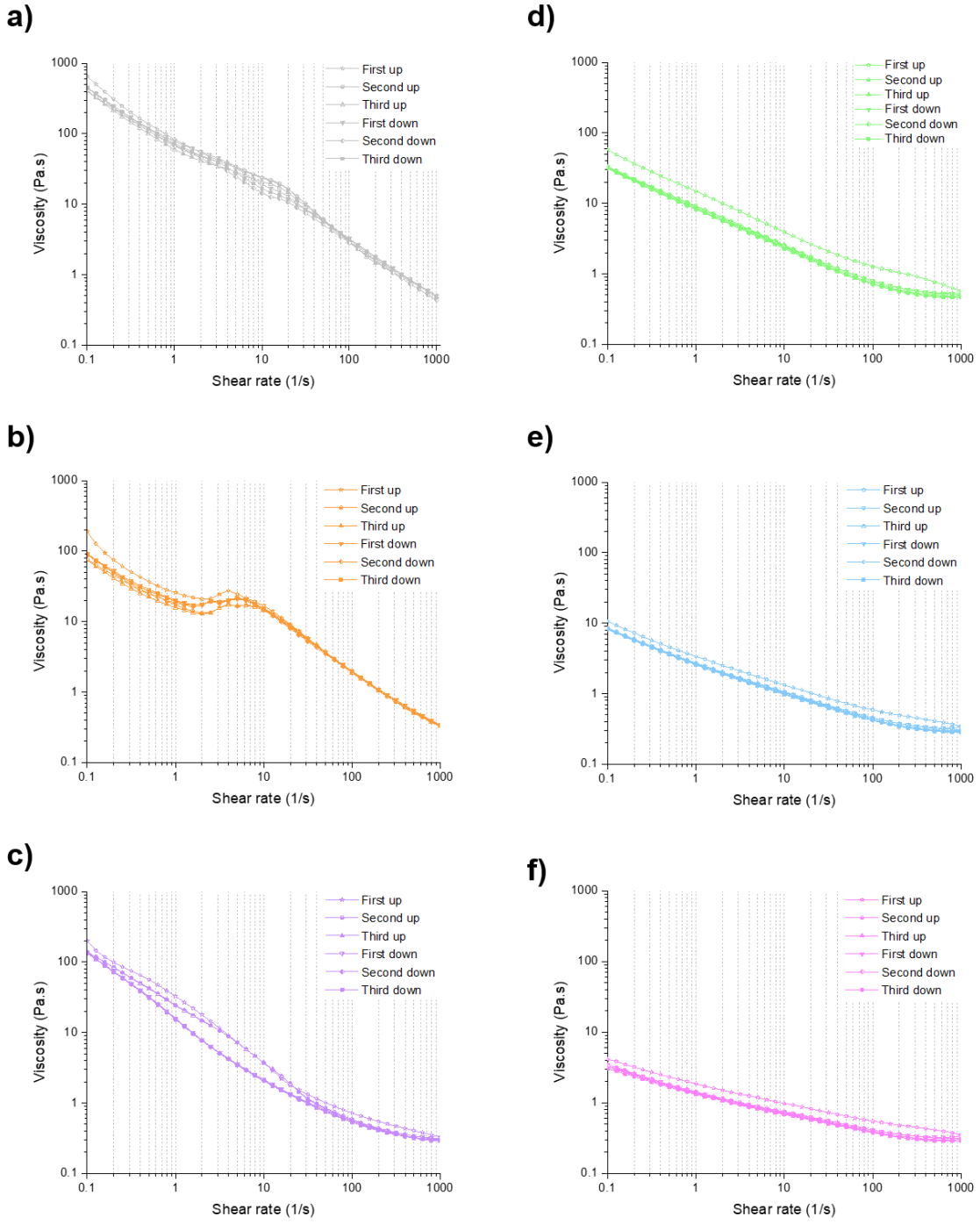


Figure 32: Flow curves with all cycles for a)100 SA, b)15 S3, c) 25 S3, d) 50 S3, e) 75 S3 and f) 100 S3 [151].

4.2.2.2 Yield stress behavior

The yield stress represents a critical yield point at which the suspension will start to flow [127] and, in the case of weakly flocculated suspensions, will provoke transition from weakly flocculated to flowing (dispersed) state with the increasing shear stress. Presented in Figure 33, are the yield stress behavior of all suspensions which were obtained from the results of shear strain measurement with respect to the applied shear stress. A large difference in the shear strain was observed between suspensions with weakly flocculated and well dispersed particles. Around shear stress of 40 Pa, the difference was up to 6 orders of magnitude, indicating a large distortion of structure for well dispersed particles. It can be seen that the weakly flocculated suspensions with a higher SA ratio (100 SA and 15 S3) had a distinct yield stress behavior at 55 Pa. The weakly flocculated suspension 25 S3 had a yield stress value of 45 Pa, while for suspensions 50 S3, 75 S3, and 100 S3, no yield stress was observed.

Data that was fitted by the Herschel-Bulkley model (Figure 31b), indicated that there was a distinct shift in the flow behavior between suspensions 100 SA and 15 S3, compared to the suspensions containing higher S3 content. Suspensions 100 SA and 15 S3 exhibited a clear yield stress behavior with minimal increase in shear rate, with an initial increase in shear stress up to a critical value of shear stress where the suspensions begin to flow. On the other hand, suspensions containing a higher amount of S3 exhibited a nearly linear shear stress-shear rate response, with no apparent yield stress behavior.

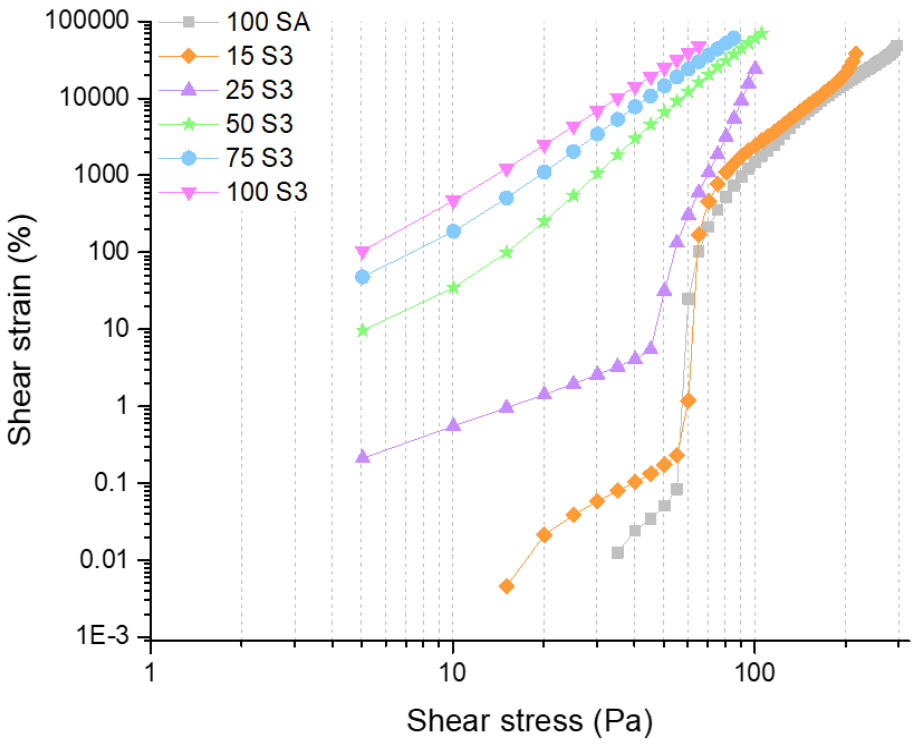


Figure 33: Shear stress versus shear strain curves for the following suspensions: 100 SA, 15 S3, 25 S3, 50 S3, 75 S3 and 100 S3 [151].

4.2.2.3 Storage and loss moduli

The viscoelastic properties of suspensions were analysed by measuring storage (G′) and loss (G″) moduli, and the results are presented in Figure 34. The temperature was decreased from 100 to 65°C during the measurement, in order to mimic the conditions that jetted suspension droplets experience during their travel from the nozzle to the print bed and eventually solidifying, after passing T_m and T_g.

Two distinct groups of suspensions were observed, as in yield point measurements. A weakly flocculated group of suspensions (100 SA, 15 S3, and 25 S3) exhibited higher moduli, whereas well dispersed suspensions showed substantially lower moduli. Namely, for the suspension 100 SA, a temperature-insensitive behavior of G′ and G″ of around 2000 Pa was observed. Suspensions 15 S3 and 25 S3 had an order of magnitude lower G′ and G″ values, in the 250–700 Pa range at 100 °C. When the ratio of S3 in suspensions was increased further, G′ and G″ values decreased for an additional order of magnitude, i.e., to the 10–100 Pa range. Except for suspensions 100 SA and 15 S3, all suspensions were temperature sensitive, and both moduli gradually increased with the decrease in temperature from 100 to 70 °C. When the temperature was lowered, low and high SA containing suspensions had G′ and G″ in the 80–250 and 1000–2500 Pa range, respectively.

At 67 °C (red dashed line in Figure 34), a sharp increase in both moduli was observed for all suspensions, indicating solidification at this temperature, which was in accordance with the melting temperatures of these suspensions, which were observed by TG/DTA (Figure 29). Prior to solidification, G″ > G′ was observed for all suspensions, which indicated a flow behavior [136].

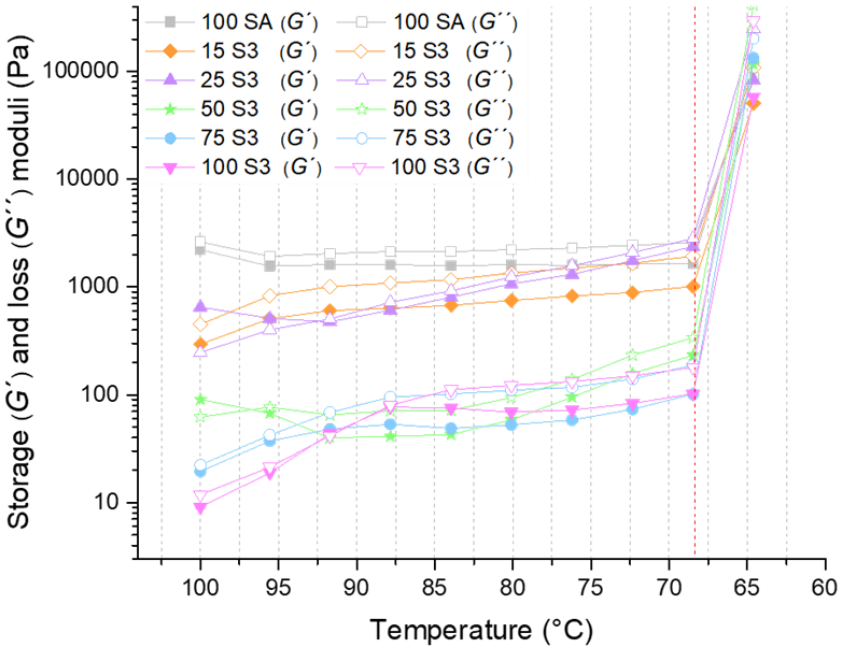


Figure 34: The storage (G′) and loss (G″) moduli of suspensions in relation to the temperature decrease [151].

4.2.2.4 Calculating Reynolds number

Re for each suspension was calculated in order to understand the effect of different surfactant combinations, and consequential steric barrier configuration and thickness on the jetting of all feedstocks. Results are presented in Table 3 along with other rheological properties. It was concluded that *Re* values above 0.064 were needed for deposition, while for *Re* values up to 0.398, no formation of satellite droplets was observed.

Table 3: Properties of zirconia suspensions with 40 vol% solid loading, summarized [151].

Suspension	**Viscosity**	***Re***	**G″**	**Yield stress***	**Yield stress****	**Printability of droplets**
	Pa · s (@ 10 s^{-1})		Pa (@ 100 °C)	Pa	Pa	
100 SA	16.7	0.014	2615	55	/	Clogging, flaws
15 S3	14.9	0.016	450	55	/	Flaws
25 S3	3.7	0.064	246	45	27	Flaws
50 S3	2.2	0.1	62	/	6	Defect free
75 S3	0.9	0.265	22	/	3	Defect free
100 S3	0.6	0.398	11	/	2	Low viscosity

* Data obtained from the yield stress measurement
** Data obtained from the Herschel-Bulkley model

4.3 Jetting Behavior of Individual Droplets and Lines as a Function of Suspension Characteristics

Different stages of droplet formation during jetting with T3DP, observed with a high-speed camera, are presented in Figure 35. The results indicate that the droplet formation took place in 3 main stages: extrusion, spreading, and droplet formation. Initially, in the extrusion stage, the feedstock was extruded from the nozzle, and landed on the print bed, while forming an elongated structure between the nozzle and the print bed. This was followed by the spreading i.e., increase in diameter of the deposited droplet on the print bed. The final stage was the formation of a droplet, where some differences among feedstocks were observed. For the highest SA containing feedstocks 100 SA and 15 S3, that were weakly flocculated and exhibiting the highest yield stress value of 55 Pa (Figure 33), droplets had inhomogeneous and asymmetrical tail geometry. This was indicative of high viscous forces present in these feedstocks. In the case of 25 S3 feedstock, which can be still considered as weakly flocculated, but with lower yield stress of 45 Pa, the tail receded and a “pancake-like” droplet was formed. For the rest of the “well-dispersed” feedstocks, the tail was receded prior to solidification of extruded material and a more well-defined spherical final droplet was formed. Differences in the extent of spreading of droplets on the print bed were also observed, where the lowest values were observed for feedstocks with the highest amount of S3.

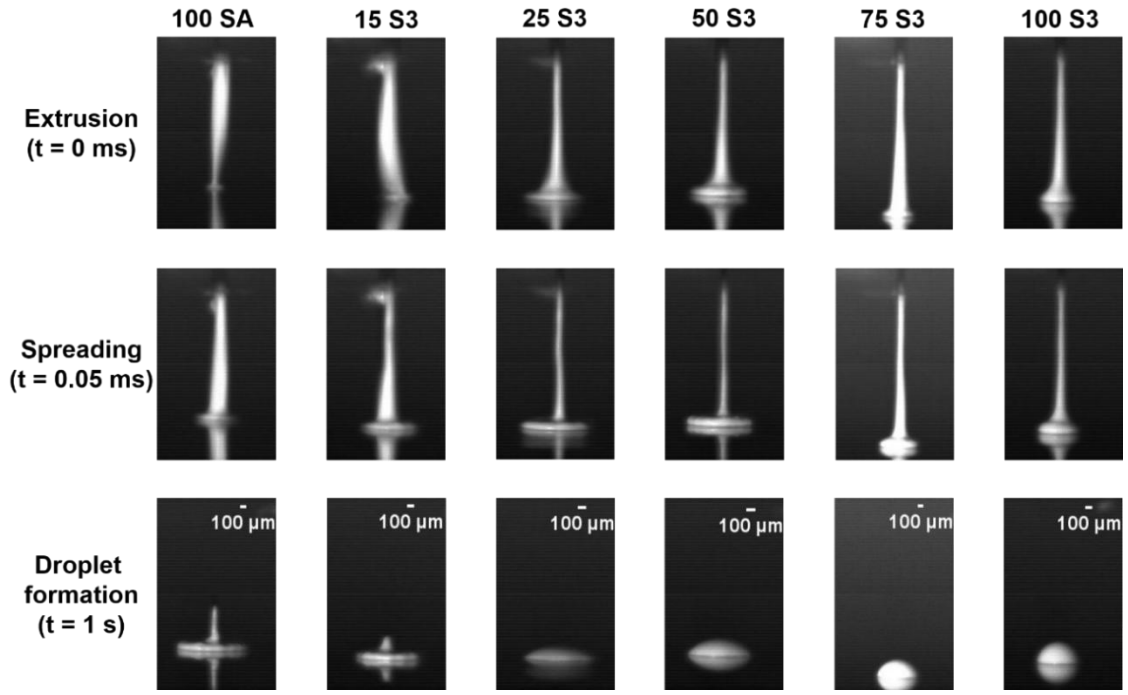


Figure 35: Droplet formation during jetting with T3DP recorded by high-speed camera [151].

The deposited droplets from all the feedstock compositions were further characterized for topographical analysis with stereomicroscopy and optical microscopy, and the results are presented in Figure 36. Droplets deposited using feedstock 100 SA showed a spatter morphology with a highly irregular edge (Figure 36a). For both weakly flocculated feedstocks exhibiting pronounced yield stress, i.e., 100 SA and 15 S3, observations of droplet tail formation were confirmed (Figure 36a and b). The rest of the droplets did not have this flaw in their centre. This indicated that a more droplet-like shape could be obtained when the surface tension dominated the viscous forces within the time prior to solidification. It was observed that the droplet diameter was inversely proportional to Solsperse 3000® ratio while droplet height was directly proportional. The diameter and height values obtained are presented in Figure 37.

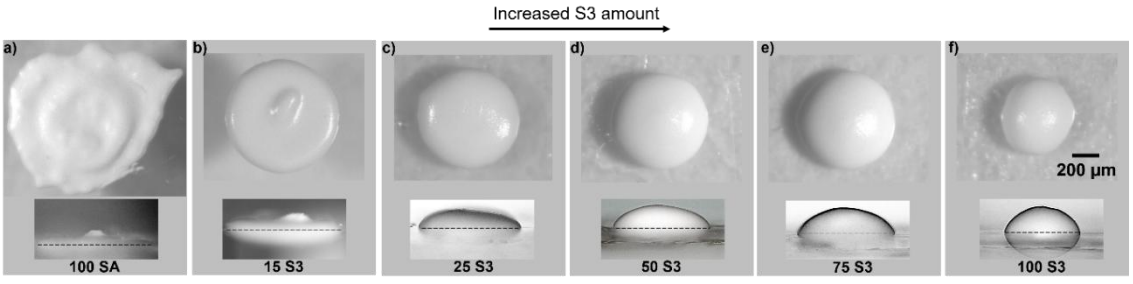


Figure 36: Top and side optical micrographs of deposited droplets from feedstocks: a)100 SA, b)15 S3, c) 25 S3, d) 50 S3, e) 75 S3 and f) 100 S3 [151].

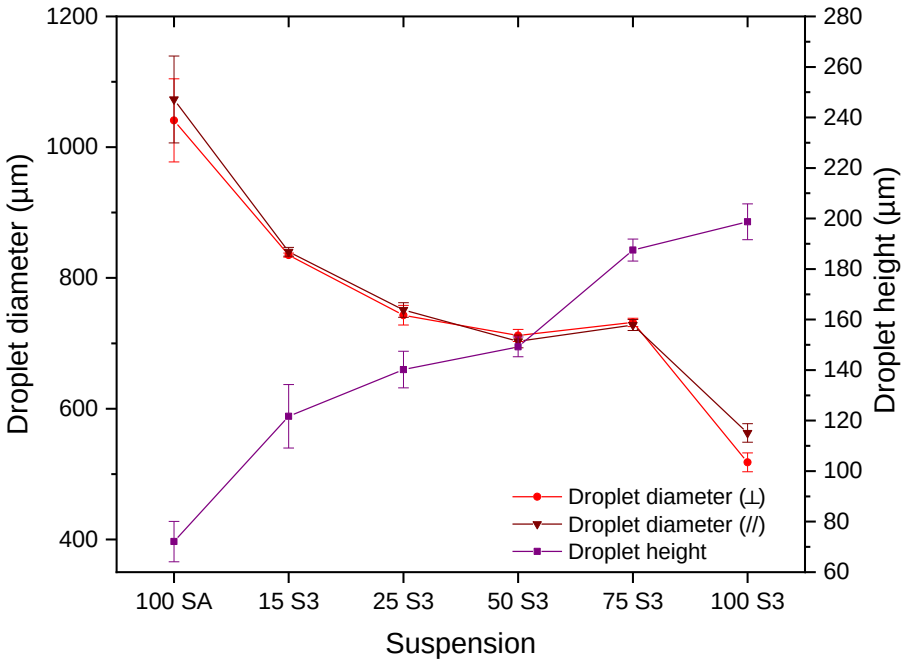


Figure 37: Droplet diameter versus height with respect to feedstock composition [151].

After droplet jetting on the print bed, the fusing of deposited droplets into lines was conducted and likewise evaluated by a high-speed camera. The high-speed camera micrographs are presented in Figure 38. As expected, the flaws obtained from individual droplets were translated and accumulated in the printed lines for weakly flocculated feedstocks 100 SA and 15 S3. Non-receded tails resulted in the formation of inhomogeneous lines with varying thickness and height. On the other hand, the lines formed from slightly flocculated feedstock 25 S3, and well dispersed 50 S3 and 75 S3 feedstocks presented minor differences in droplet overlap and line thickness, especially in the formed edge of a line exhibiting smaller and larger inter-fused droplet voids. Finally, the lines formed from feedstock 100 S3 had complete fusion between individual droplets, which formed a continuous, well-defined line.

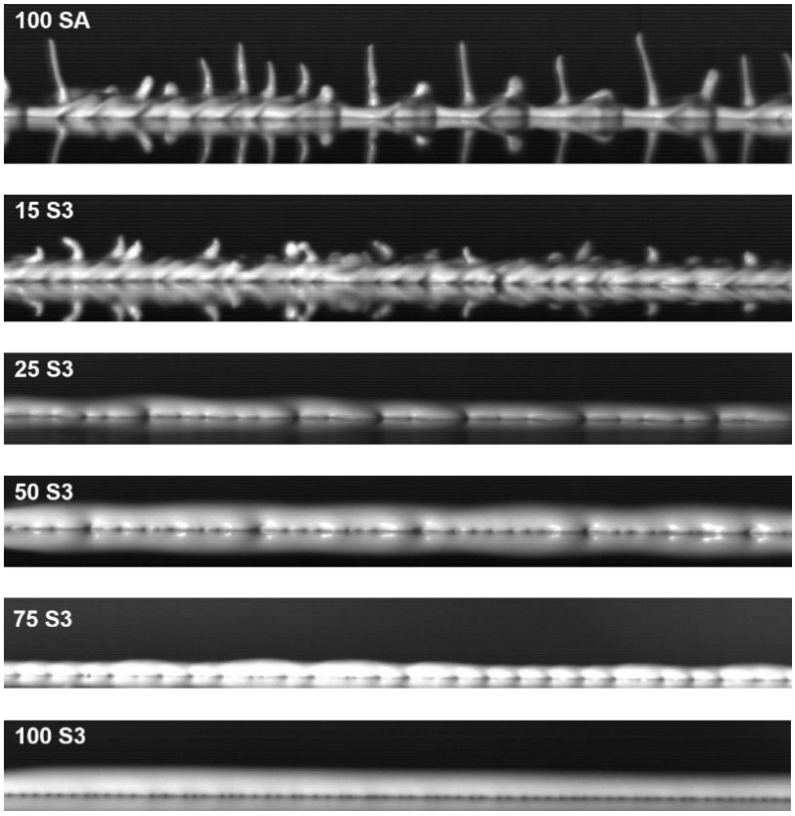


Figure 38: High-speed camera images presenting single lines formed from fused droplets jetted by T3DP from the following feedstocks: 100 SA, 15 S3, 25 S3, 50 S3, 75 S3 and 100 S3 [151].

4.4 Morphology of Printed Single Layers from Fused Droplets and Lines

Surface morphology of printed single layers of ~ 40 mm x 40 mm is presented in Figure 39. Using weakly flocculated suspension 100 SA (Figure 39a) as feedstock for T3DP process, it was not possible to complete the deposition of a single layer due to the collection of feedstock on the nozzle as a result of increased viscous resistance. It was possible to print a single layer from weakly flocculated feedstock 15 S3 (Figure 39b), but in line with poor droplet and line quality (Figure 38), the layer had poor homogeneity, i.e., had poor surface quality and irregular deposition, especially at the end of the print job, which was marked with yellow arrows in Figure 39b. Slightly better but similar outcome was observed in the case of feedstock 25 S3 (Figure 39c), which exhibited the weakest yield stress. Acceptable homogeneity of single layers, from the start to the end of layer print, was achieved with feedstocks 50 S3 (Figure 39d) and 75 S3 (Figure 39e). Surprisingly, by using the well dispersed feedstock 100 S3, exhibiting the most well-defined droplets and lines (Figure 39f), it was not possible to form a complete layer, that might be due to process related parameters such as overheating of the system.

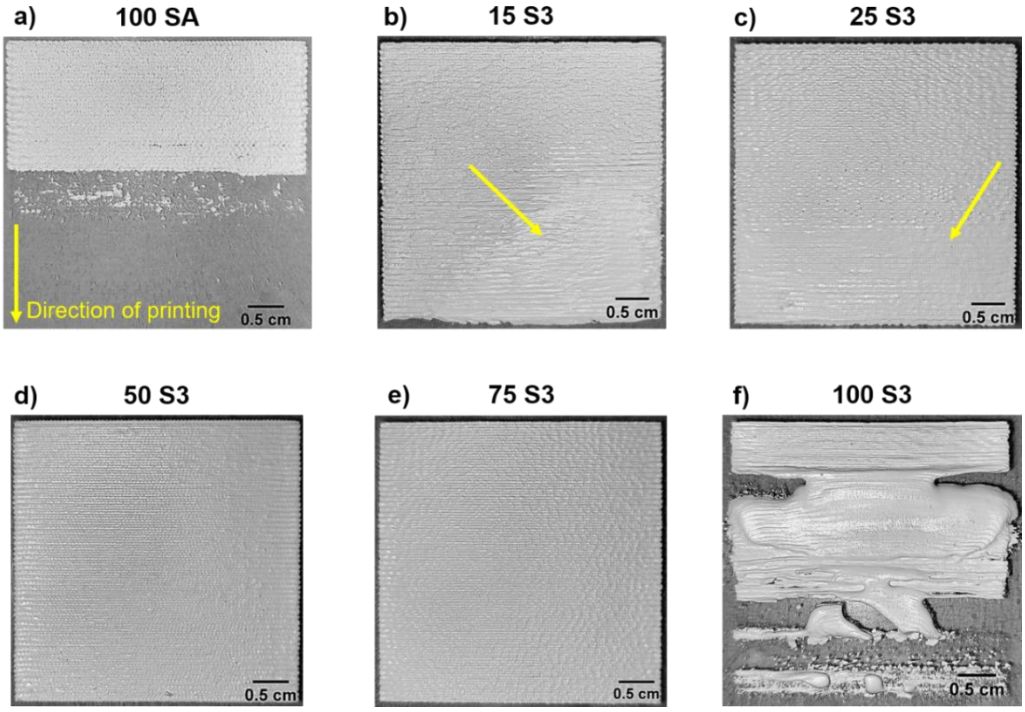


Figure 39: Topographical view of single layer squares printed from feedstocks: a)100 SA, b)15 S3, c) 25 S3, d) 50 S3, e) 75 S3 and f) 100 S3 [151].

The 3D surface texture morphology and the surface roughness parameters of printed single layers were assessed quantitatively by profilometry and are presented in Figure 40. Layers printed from feedstock 100 SA showed the highest level of irregularities as an outcome of fusing tail-containing, spatter-like droplets. Consequently, this sample exhibited the largest deviation in height (~250 µm) and uneven, wave-like surface topography with the highest S_a of 33 µm. The surface topography of 15 S3 was similar, but had lower height deviation (~200 µm) and S_a and S_{dr} parameters of 29 µm and 26%, respectively. Layers printed from feedstocks 25 S3 and 75 S3 exhibited similar height deviation (~150 µm). Notably, 75 S3 had more straight and well-defined lines. These two layers exhibited S_a of 24 and 18 µm and S_{dr} of 8 and 12%, respectively. The single layer with the least texture inhomogeneities, low surface roughness parameters S_a and S_{dr} (13 µm and 5%), and the lowest height deviation (~100 µm) between the fused droplet lines was measured for the layer printed from feedstock 50 S3.

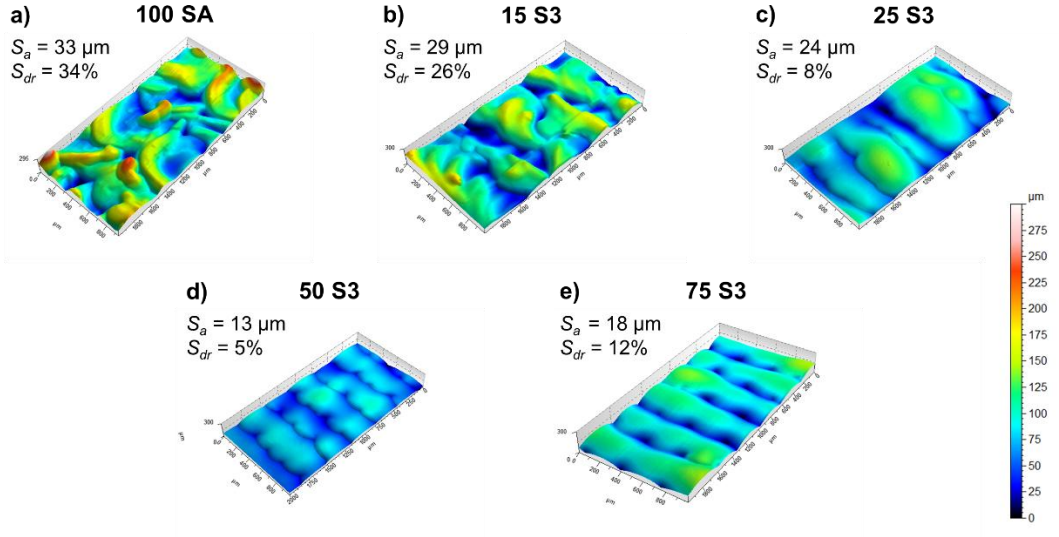


Figure 40: Profilometry 3D surface textures with corresponding roughness values of single layer squares printed from feedstocks: a)100 SA, b)15 S3, c) 25 S3, d) 50 S3 and e) 75 S3 [151].

4.5 Properties of Bending Bars Prepared by T3DP

In the second part of the study, related to the short mobility stay at Fraunhofer IKTS, the infill strategy was varied to evaluate the mechanical strength and flaw population. The zirconia suspensions developed at Fraunhofer IKTS were used as feedstocks for the T3DP process. Prior to the printing of bending bars, individual droplets were printed and characterized to determine the characteristic dimensions. The dimensions of the droplets were found to be $d_{//} = 850$ µm, $d_{\perp} = 700$ µm, and $h = 160$ µm. In the following chapters, the results on the properties of sintered bending bars, printed with three different infill strategies, i.e., 0°, 90°, and 0° + 90°, are presented.

4.5.1 Density measurement

The sintered bending bars had density values above 99.0% of the theoretical value for all infill strategies, as can be seen in Table 4. The differences between the density values for different infill strategies were insignificant, thus, varying the infill strategy did not alter the final densities, which can be the case in other AM techniques such as FFF [50].

Table 4: Sintered densities of parts [54].

Infill orientation	Sintered density
0°	99.0 ± 0.3%
90°	99.1 ± 0.2%
0° + 90°	99.3 ± 0.4%

4.5.2 Microstructure and phase analysis

Parts prepared with 0° infill strategy exhibited a typical microstructure for 3Y-TZP ceramics, consisting of equiaxed grains with a grain size of approximately 300 nm (Figure 41).

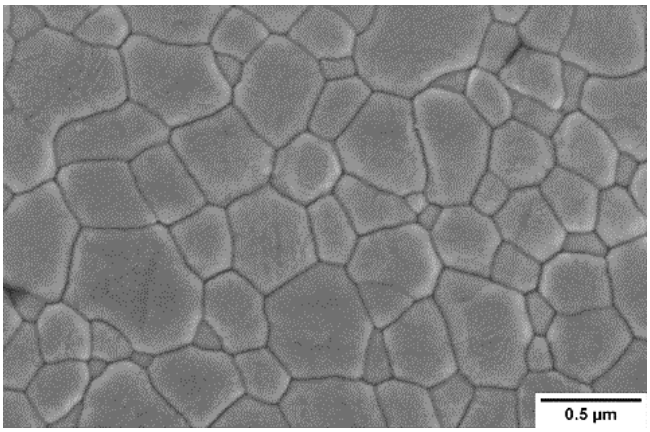


Figure 41: SEM micrograph of polished-and-etched sample with 0° infill strategy [54].

The XRD diffractogram of the ground and polished sample surface (Figure 42) showed the slight presence of the monoclinic (m-ZrO_2) phase, as a result of the grinding-induced phase transformation from tetragonal (t-ZrO_2) to monoclinic (*t-m*). In addition, low-2-theta asymmetric broadening of the main $(110)_t$ tetragonal peak was observed. The broadening of the peak was the result of the presence of residual compressive stresses in the part, induced by machining [159], which introduces surface irregularities masking the "inherent" flaw population of the samples and thus affecting the strength of the component [160], [161]. To reverse the *t-m* phase transformation and remove the compressive residual stresses, regeneration firing was applied at 1000 ℃ for 15 min [61], [162]. The second XRD measurement confirmed the success of the regeneration firing, as the asymmetry of the peak at $2\theta = 30°$ and the stresses were successfully annihilated.

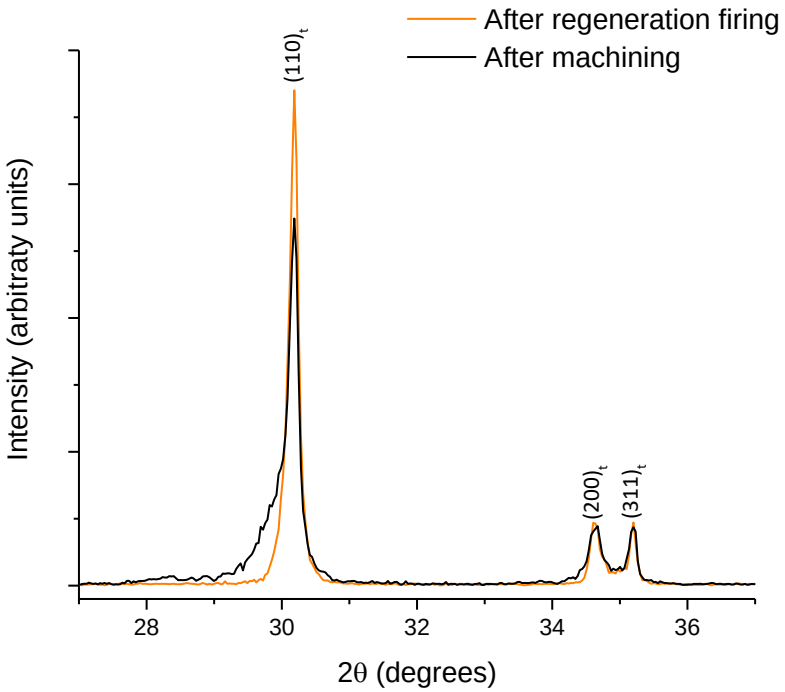


Figure 42: XRD pattern after machining and after regeneration firing [54].

4.5.3 4-point bending test and Weibull analysis

Thirty grinded and chamfered test specimens per infill strategy series were monotonically fractured using a universal testing machine. The results of 4-point bending tests on parts prepared with 3 different infill strategies are presented in Table 5. 0° series had the highest characteristic strength of 700 MPa, followed by 90° series, with characteristic strength of 662 MPa. Surprisingly, series printed with the 0° + 90° infill strategy, where the direction of fused lines in consecutive layers was alternating, had the lowest characteristic strength of 624 MPa.

Table 5: Strength (σ), characteristic strength (σ_0) and Weibull modulus (m) of parts for each infill strategy [54].

Infill strategy	**Strength (σ) (MPa)**	**σ_0 (MPa) [90% CI]**	**m [90% CI]**
0°	655 ± 110	700 [668–735]	7.0 [5.23–8.51]
90°	617 ± 109	662 [628–698]	6.4 [4.8–7.81]
0° + 90°	581 ± 102	624 [590–660]	6.0 [4.51–7.34]

Weibull strength distribution for parts prepared with different infill strategies is presented in Figure 43. The complete lines represent the best fit of the strength values according to the maximum-likelihood method, and the dashed lines represent the 90% confidence intervals. Like in the case of characteristic strengths, the differences in Weibull moduli were not significant, but still in accordance with the trend observed for the σ_0. The highest Weibull moduli were achieved for the 0° infill strategy ($m = 7.0$), followed by the 90° series exhibiting m of 6.4, while the 0° + 90° infill strategy had the lowest at a value of 6.0 (Table 5). Overall, the Weibull moduli were lower compared to dry-pressed or injection moulded, densely sintered, defect-free 3Y-TZP ceramics, which usually exhibit m values greater than 10 [159], [162]–[164]. On the other hand, the AM techniques, especially the extrusion-based, are prone to inter-filament and inter-layer defects, which result in substantially lower m values of less than 10. In the work of Cano et al. [50], FFF was used to fabricate zirconia bars by changing the infill strategy. In contrast to the present study, the infill strategy had a significant impact on m values, i.e., sample series of 0°, ±45°, and 90°, yielded m values of 9.9, 6.5, and 4.3, respectively. However, the 0° series from FFF exhibited superior reliability compared to T3DP. The SLA AM technique is known as the most reliable, but the slurry composition may contain air bubbles and agglomerates, affecting the overall reliability of ceramics. As a direct consequence, a lower m (<10) was attained [165], [166].

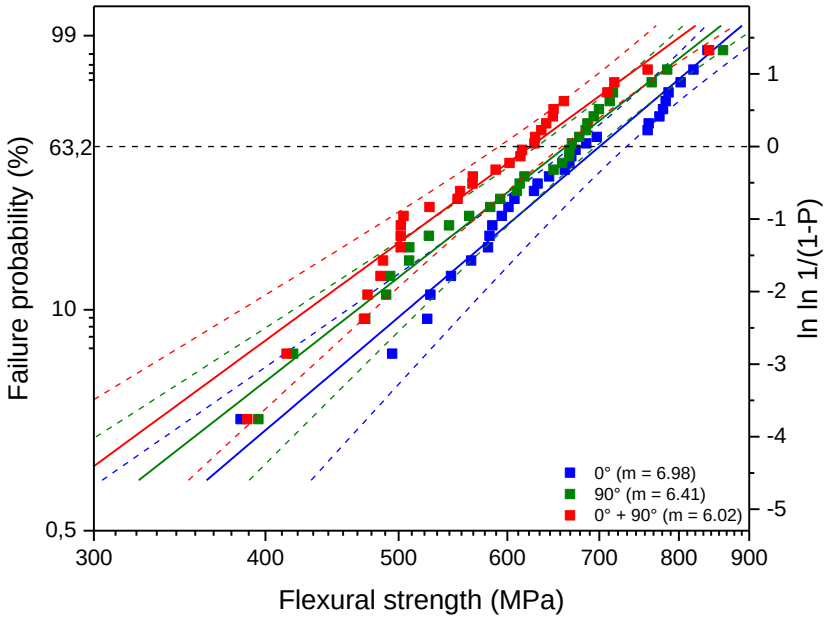


Figure 43: Weibull plot for 0°, 90°, and 0° + 90° infill strategies [54].

4.5.4 Fractography

In order to assess the strength limiting flaws and fracture origins, fractographic analysis was conducted. The results for different infill strategies are presented for parts that had high (failure probability = 98.3%), medium, and low strength (failure probability = 1.6%) values. Various types of flaws were identified, originating from *i)* feedstock inhomogeneities or *ii)* fusion of droplets to form lines and layers.

Namely, the bending bar with **0° infill strategy** and high strength of 839 MPa (strong), had a critical defect (~25 µm) on the tensile surface, and it consisted of a porous region (inset of Figure 44a). The powder used in the present study was granulated (not containing binder) and such porous region could be connected to the remaining or imperfectly deagglomerated granules with lower degree of packed zirconia particles. The sample with medium strength prepared with the 0° infill strategy had a 30 µm defect with an 80 µm-long crack (inset of Figure 44b), as a result of crack propagation during fracture. The coarse hackle lines, marked with a dashed line (Figure 44b), were observed extending out from this imperfection, as commonly observed in solid-state-sintered polycrystalline ceramics [167]. Such a relatively large imperfection was related to the fusion of subsequent droplets within the same layer, as depicted in Figure 44. For the low strength (384 MPa) (weak) sample of 0° infill strategy, an even larger defect of 150 µm was observed (Figure 44c). It was assumed that such a big flaw could be related to the inconsistent droplet deposition, as the size of the defect was similar to the height of a droplet (160 µm), which was attributed to the clogging of the nozzle, induced by the presence of agglomerates (or granules) in the feedstocks [166].

The strong bending bars with 861 MPa, prepared with **90° infill strategy** (Figure 44d) had a crack that was 80 µm next to a possibly delaminated area as a result of improper droplet-to-droplet fusion. Coarse hackle lines were propagating out from the crack confirming that this was strength limiting flaw. In addition, an air bubble with a diameter of 5–6 µm, trapped close to the origin of a fracture, was observed, as a consequence of improperly deaired suspensions, but its size was not relevant. The sample with medium strength had a larger crack of 90 µm, followed by a 120 µm-long branched system of two cracks extending into the bulk in the direction of crack propagation (dcp) (Figure 44e). The flaw was very similar to medium strength specimen for 0° infill strategy, where the flaw was related to the fusion of subsequent droplets within the same layer, even though the printing direction was different. The low strength part (395 MPa) had similar flaws to the medium strength part, however, containing an even bigger spherical flaw of about 150 µm in size and, as a consequence, a more complex fracture pattern containing twist hackles and a long crack rotated in the dcp direction (Figure 44f). Again, as in the case of 0° infill strategy (Figure 44c), such a flaw was related to the inconsistent droplet deposition due to the possible (partial) clogging of the nozzle.

Part prepared with the combination of **0° + 90° infill strategies**, with high strength values (842 MPa) (strong), had a volume type of flaw (Figure 44g), which appeared like the 30 µm-sized agglomerate surrounded by the empty volume as a result of partial sintering, producing crack-like voids responsible for fracture [168]. Such an agglomerate was already present in the feedstock or could be a part of the material clogged at the nozzle, that chipped from it and was deposited onto the printed layer. The 0° + 90° specimens with medium and low strengths (388 MPa) (Figure 44h-i) had round flaws varying in size and with the interior area of the intergranular type of surface indicating that the area was already delaminated (or poorly fused) before sintering. It was also indicative, that this infill strategy was more prone to the inconsistent droplet deposition originating from infill strategy itself (to be discussed later).

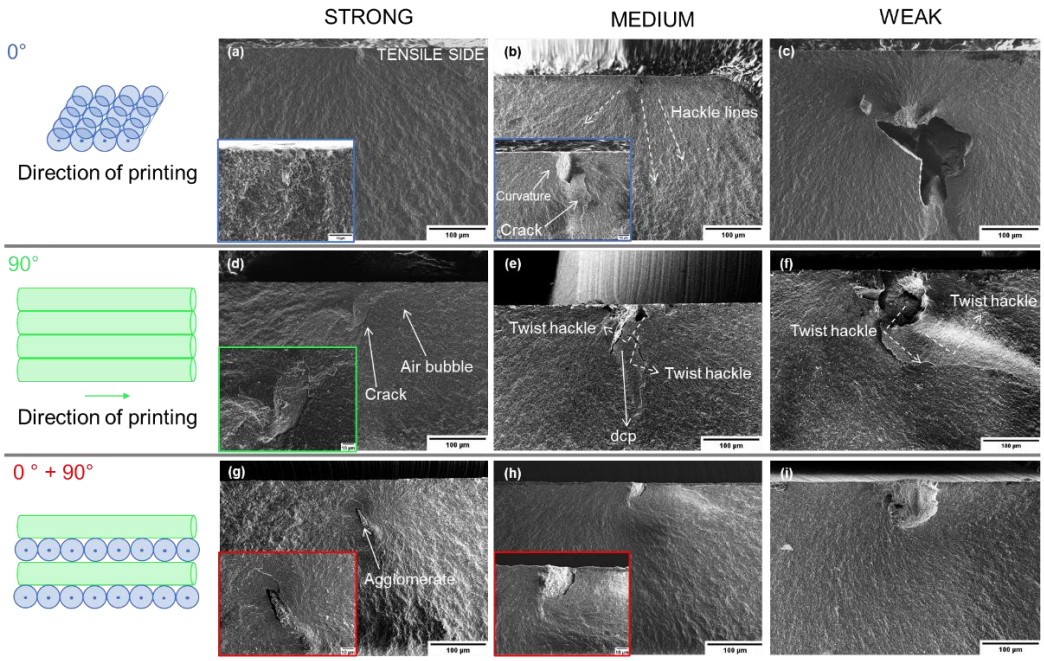


Figure 44: Fractography results for different infill strategies (from top to bottom: 0°, 90°, and 0° + 90°, from left to right: strong, medium and weak) [54].

Chapter 5

Discussion

The discussion of the present thesis is organized in three subchapters, encompassing the complete workflow of T3DP for the additive manufacturing of zirconia ceramics from feedstock of different properties achieved by tailoring the interparticle interaction with the use of two surfactants of different chain lengths.

In the **first chapter**, the effect of the steric barrier thickness and conformation on the flow indicators, evaluated through various types of rheological characterizations, i.e., viscosity and yield stress as well as the viscoelasticity of suspensions, is discussed. The steric barrier is modified by using combinations of surfactants with different chain lengths, leading to differences in its thickness and, more importantly, conformation of the used surfactants. The non-linear relation of chain length of surfactants and thickness of steric barrier is discussed, based on the differences in interaction of surfactants, assuming two types of interaction, i.e., interpenetration *versus* compression.

In the **second chapter**, the focus is on understanding the role of the rheological properties of suspensions, which are used as feedstocks in the T3DP additive manufacturing process, on the droplet jetting dynamics. The latter are pivotal for the (un)successful deposition and fusion of droplets that further form lines and layers in the component build-up process. Non-Newtonian feedstocks are used for T3DP applications, making it more complicated to set a range of rheological parameters, such as viscosity, *Re,* or *We*, which are reliable indicators for jetting of Newtonian feedstocks. Here, the focus is on feedstock related issues, such as clogging of the nozzle, unfinished and unsuccessful (cancelled) print jobs, and relate them to the rheological properties of the suspensions as well as particle interactions, that can lead to well dispersed state of the suspensions or to various magnitudes of weak flocculation. An attempt to define a "*roadmap*" for the properties of suspensions used as feedstocks for the T3DP process is made. The most suitable feedstocks were used for the printing of demonstrators.

Finally, in the **third chapter**, the effect of the infill strategy on the mechanical properties of parts prepared by T3DP is discussed. The effect of infill strategy on the mechanical properties of parts prepared by different extrusion-based AM methods is widely studied, but for T3DP, this remains unexplored. This issue is addressed by comparing microstructure, fracture strength, and flaw population of rectangular bending bars prepared with 3 different infill strategies, comparing them to other AM techniques such as FFF and SLA. In addition, even though it was shown that T3DP is practically insensitive to the infill strategy, as in contrast to FFF, relatively low characteristic strengths and Weibull moduli were obtained here, which will be discussed through the accuracy of positioning of individual droplets and how these micron sized details affect the final parts.

5.1 The Role of Steric Barrier Thickness and Conformation on the Flowability and Viscoelasticity of Suspensions Used for T3DP

This part of the discussion is divided into two sub-chapters. First, the role of the steric barrier thickness and conformation on the flow indicators (viscosity and yield stress) of prepared suspensions is discussed. Then, in the second sub-chapter, the viscoelastic behavior of suspensions at rest, provided by oscillatory measurements of storage and loss moduli, is discussed as well, providing deeper insight into the rheological behavior and state of the suspensions.

5.1.1 The mechanistic model of steric barrier interactions affecting flowability of suspensions

The steric barrier thickness and conformation govern the interparticle interactions, therefore affecting the flowability of suspensions when exposed to shear stress. The steric barrier was modified by using combinations of surfactants with different chain lengths. The differences in steric barrier led to differences in viscosities, shear thinning behavior (monotonous vs non-monotonous) (Figure 31) and the presence/lack of yield stress (Figure 33). Suspensions with shorter steric barriers had weakly flocculated particles, resulting in higher viscosities and non-monotonous shear thinning behavior with a distinct yield stress. In contrast, the rest of the suspensions showed lower viscosities, monotonous shear thinning behavior, and low/non-existent yield stress.

The steric barrier thickness. The steric barrier thickness is an important parameter that controls particle interactions and subsequently, the rheological properties of suspensions. For the suspensions prepared by using only stearic acid (100 SA) and Solsperse 3000® (100 S3), the chain lengths of surfactants (2.4 nm [125] and 10 nm [148]) were equal to the steric barrier thickness, as the monolayer coverage of surfactants of the same chain length allowed the fully extended "brush" conformation. On the other hand, when the combinations of these surfactants were used, the potential conformations and the consequential steric barrier thickness were unknown. The steric barrier thickness for these suspensions could be calculated based on the knowledge that the yield stress and the attractive potential energy are directly correlated [125]. The values of yield stresses that were measured for 100 SA, 15 S3, and 25 S3, as well as the values calculated by the H-B model for 50 S3, 75 S3, and 100 S3 (Table 3) were used in combination with Equation 3 to make computational iterations which led to the values of thickness of steric barrier between the dispersed particles in paraffin wax, yielding 2.4 nm, 2.8 nm, 7.9 nm and 9.4 nm for suspensions 15 S3, 25 S3, 50 S3, and 75 S3, respectively. Once the thicknesses of steric barriers between the particles were calculated for all the suspensions, the obtained values were used to calculate the van der Waals attractive forces, using Equation 3.

The resulting interaction potentials with respect to steric barrier thickness, presented in Figure 45, show a non-linear (negative reciprocal function) increase in the attractive potential as the amount of the surfactant with short chain length is increased. Suspensions with weakly flocculated particles (100 SA, 15 S3, and 25 S3) have a steric barrier thickness of less than 3 nm and interaction potential below -6.8 $x10^{-20}$ J, while suspensions with well dispersed particles (50 S3, 75 S3, and 100 S3) have a steric barrier thickness above 7 nm and interaction potential above -2 $x10^{-20}$ J, which was in agreement with *hypothesis 1.* These values showed a similar trend to those obtained by Bergstrom et al. [94] where the consolidation behavior of alumina suspensions was studied. In their work, particle

interactions and the resulting flocculation behavior was used as an indicator of compressibility and consolidation and for steric barrier thickness of 0.7 nm, achieved by propionic acid, attractive potential of -54 kT (-21.6 x10^{-20} J) was observed while increased steric barrier thickness resulted in a decrease of attractive potential where oleic acid with 2.5 nm thickness resulted in -11 kT (-4.4 x10^{-20} J). Furthermore, Studart et al. [169] also showed a decrease of attractive potential energy with increased steric barrier thickness, where dispersant with a short length of 0.97 nm resulted in a potential of -5.7 kT (-2.3 x10^{-20} J) and surfactant with a longer length of 2.52 nm resulted in a potential of -1.3 kT (-0.5 x10^{-20} J).

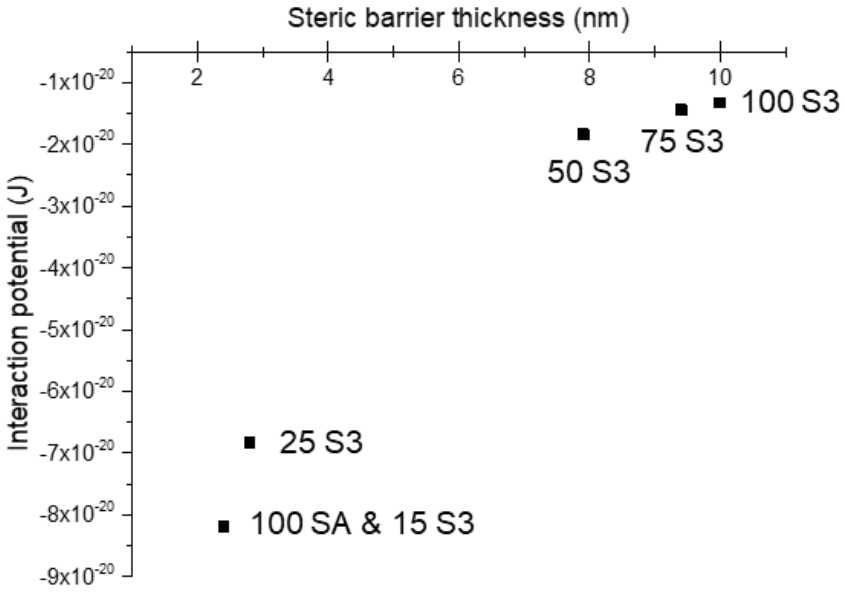


Figure 45: Interaction potential vs steric barrier thickness between particles dispersed in paraffin.

The relation between steric barrier thickness and conformation, interaction potentials, and rheological properties (yield stress and viscosity) for all the suspensions is presented in Figure 46. The important thing to note is the non-linear, sigmoidal type of relationship between the surfactant ratios and the thickness of the steric barrier. Obviously, this is directly correlated to the non-linear increase/decrease of attractive potential dictated by the steric barrier thickness and surfactant conformation during interparticle interactions. As a consequence, the apparent viscosities and yield stresses also exhibit non-linear, sigmoidal behavior corresponding to the barrier thickness (attractive potential), where, in addition, the steric barrier conformation during interparticle interactions contributes to viscosity and yield stress. For example, 100 SA and 15 S3 have the identical yield stress value of 55 Pa, while the former exhibits slightly non-monotonous flow behavior and the latter a non-monotonous flow behavior (Figure 31a).

Conformation of the steric barrier. Due to differences in the conformation of steric barriers, where the surfactant chains can be compressed or overlapped, as explained in Figure 14, the thickness of the steric barrier is varied, non-linearly related to the changes in the ratios of surfactants.

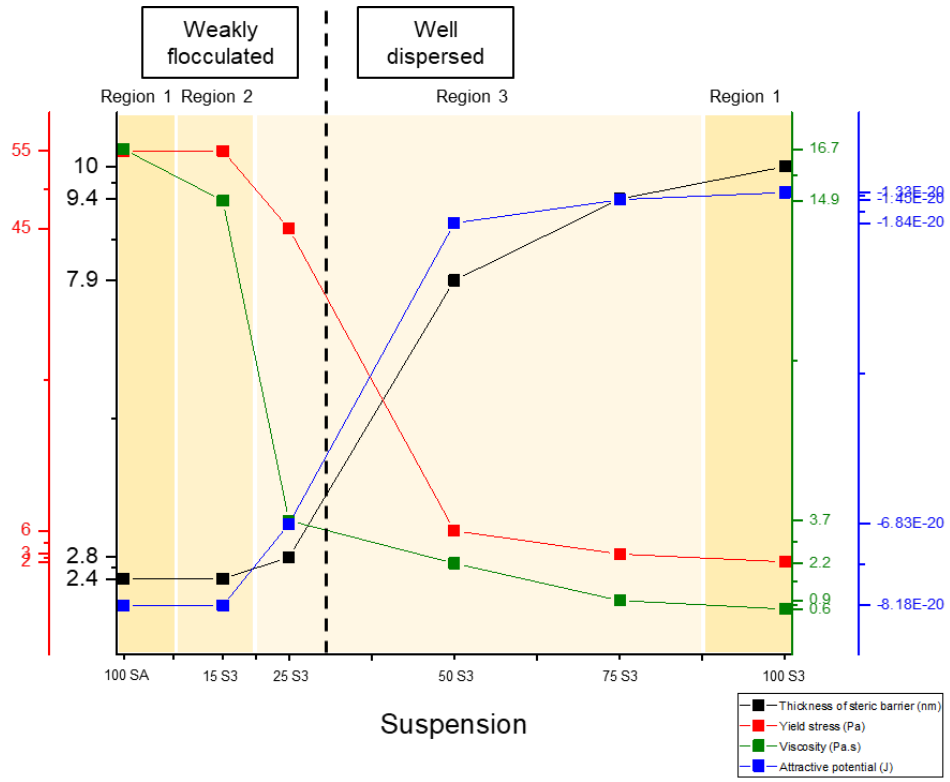


Figure 46: The relation of steric barrier thickness with the flow indicators and particle interactions for all suspensions.

In Figure 46, it is possible to observe three distinct regions, with possible conformations schematically presented in Figure 47:

Region 1. The first region is for suspensions 100 SA and 100 S3, where a single surfactant is used, and the thickness of the steric barrier can be assumed equal to the chain length of the surfactants, and this region is referred to as the *rigid region*.

Region 2. In the second region, which is labelled as the *overlapping region*, suspension 15 S3 is presented, where changes in the surfactant ratio compared to suspension 100 SA did not cause changes in the rheological properties.

Region 3. Finally, the third region is labelled as the *compression region*, consisting of suspensions 25 S3, 50 S3, and 75 S3, where the changes in the ratio of surfactants result in non-linear changes in the steric barrier thickness and properties of the suspensions.

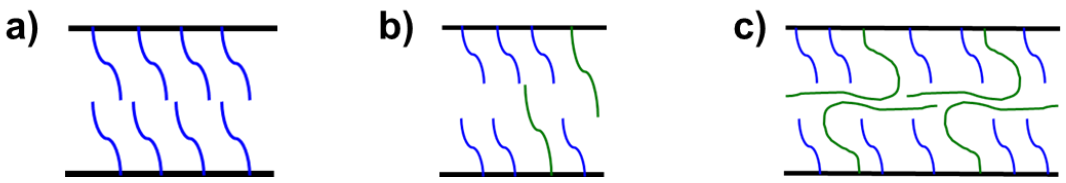


Figure 47: Schematic representation of the possible chain interaction: a) rigid, b) overlapping, c) compression.

In the **region 1** (*rigid region*) of Figure 46, suspensions 100 SA and 100 S3 are presented. For these two suspensions, full monolayer coverage of the particles by a single surfactant provided a rigid layer of steric barrier, where the surfactant chains are assumed to be fully extended. This rigidity provided resistance to overlapping and compression of the surfactants. Therefore, the thickness of the steric barrier could be considered equal to the surfactant length. For suspension 100 SA, the steric barrier thickness was 2.4 nm, and the surfactants provided a dense monolayer coverage of the particle surface. For this suspension, due to its short chain length, the stearic acid could provide only semi-steric stabilization [111], [125], which was unable to completely overcome the attractive van der Waals forces, thus residing in a secondary minimum with an attractive interaction potential of -8 $x10^{-20}$ J. This in turn resulted in an attractive particle network, causing the suspension to become **weakly flocculated** with a yield stress of 55 Pa and pronounced shear thinning and a slightly non-monotonous flow (Figure 31a).

The suspension 100 S3, on the other hand, had a pseudo-Newtonian (and monotonous) flow behavior (Figure 31a) and did not exhibit any yield stress behavior (Figure 33) due to well-dispersed particles at an interparticle distance of 20 nm (steric barrier thickness of 10 nm) where attractive van der Waals forces were not operative. Solsperse 3000®, due to its 10 nm, 66 carbon long chain [147], was adequate to allow complete steric stabilization of ceramic particles, resulting in a **well dispersed** suspension.

Suspension 15 S3 was ascribed to the **region 2** (*overlapping region*) in Figure 46. Suspension 15 S3 exhibited a yield stress of 55 Pa (Figure 33) and a non-monotonous shear thinning behavior (Figure 31a). This suspension had a high amount (85%) of short chain surfactant, stearic acid, adsorbed to the particle, accommodating the longer S3 molecules in between a dense SA layer. This partial immobilization of long-chained S3 molecules could prevent their compression when interacting with other particles [170]. It showed that the steric barrier thickness for this suspension was 2.4 nm (Figure 46), same as for 100 SA, which can be explained by the *overlapping (interpenetration)* (Figure 47) of Solsperse 3000® chains, allowing particles to come as close as the thickness of the dense stearic acid layer at 2.4 nm. This interaction results in a **weakly flocculated** particle network and a consequential yield stress of the suspension, same as suspension 100 SA.

Along with suspension 100 SA, suspension 15 S3 had a high initial viscosity and high pseudoplasticity, which can be explained by the fact that these suspensions had high amount of liquid medium trapped in the agglomerates at low shear rates, and when the shear rate was increased, trapped liquid medium was released, resulting in a large decrease of volume fraction of agglomerates [97] and consequently, of viscosity [117]. In addition, suspension 15 S3 had a pronounced non-monotonous shear thinning behavior with the presence of a shear thickening region. This behavior can be explained by the possible desorption of the surfactant with long chain from the particle or even the inability of the longer, more branched surfactant to form chemical bond with the particle surface, competing with SA. The carboxylic acid should form a covalent bond with the oxide powder surfaces, as shown in Figure 48. According to Wolfrum and Ponjee [171], one carboxyl group should be present on approximately every 0.55 nm^2 on the alumina surface, as calculated from carbon analyses and specific surface area. However, carbon analysis showed that the surface coverage of stearate was lower, i.e., one chain moiety per 1.2 nm^2. Moreover, Novak et al. [105] showed that alumina-paraffin suspensions were highly sensitive to the presence of moisture and in this case prone to destabilization, due to the fact that surfactant will only be physiosorbed instead chemically bonded. All these facts indicate the complexity and possible competition for adsorption of two dissimilar surfactants. In case of a potential excess of surfactants, these act as plasticizers, which may be the reason for slightly lower viscosity values of suspension 15 S3 than 100 SA. On the other hand, the overlapping sections of the long chain surfactant might also get entangled

and detangled with changing shear rates, leading to a transition to a disordered state. This possibility is less likely as it might lead to a larger interparticle distance and much lower viscosity values than observed. These dynamic situations of adsorption/desorption and entangling/detangling that occur at different shear rates result in the highly non-monotonous behavior seen for this suspension. According to the literature, the flow of concentrated colloidal suspensions, which under the effect of shear forms particulate layers sliding over each other, can be disrupted at a given shear rate. Order-disorder transition occurs at a critical shear rate and this disruption occurs due to the combination of the van del Waals forces and shear stress, thus the dilatant discontinuity arises [172], [173]. Below this critical point, particles are well ordered, forming layers which are able to flow over each other, resulting in a shear thinning behavior. When the critical shear rate is reached, these layers are broken, a less ordered state is reached, and due to particle jamming, viscosity increases while shear forces overcoming the interparticle repulsive forces also result in shear thickening and non-monotonous behavior of suspensions at a critical shear rate [124]. In the case of 15 S3, this critical shear rate was observed to be 2 s^{-1}, where the shear thickening started (Figure 31a).

Due to the observed flow discontinuity (Figure 31), poor fits of the shear stress-rate data were obtained using the Herschel–Bulkley model for suspensions 100 SA and 15 S3. For example, a similar, non-monotonous behavior was observed by Filip et al. [174] in polymer-based alumina feedstocks, stabilised with oleic acid, suitable for powder injection moulding. In this case, discontinuity in flow was observed at higher shear rates, higher viscosities, and temperatures.

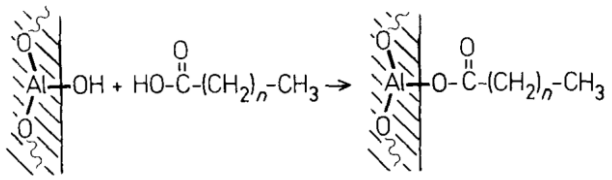


Figure 48: Formation of a monomolecular layer on alumina [171].

Suspensions 25 S3, 50 S3, and 75 S3 compose the **region 3** (*compression region*) in Figure 46. The suspension 25 S3 had a yield stress of 45 Pa, while suspensions 50 S3 and 75 S3 did not have measured yield stress behavior. All of these suspensions had a monotonous shear thinning behavior. With these suspensions, as the SA amount decreased and S3 amount increased, the rigid and dense adsorption layer provided by the short chain surfactant got weaker. This allowed the long chain S3 surfactant to be *compressed* (as shown in Figure 47), and thus the interaction was less complex compared to region 2. In region 3, the compressed (folded) section of the chain acted as a lubricant, leading to a decrease in viscosity. Amphipathic molecules such as fatty acids are attached to the surface of the particle, and provide boundary lubrication, lowering the friction coefficient and preventing contact of particles [124]. Fluid lubrication, also known as hydrodynamic lubrication, works similarly, but it may not be as effective as boundary lubrication, as it relies on the use of a liquid, which may be easily removed from the area between particles under compression, resulting in the absence of the lubrication effect [99].

This lubricating effect results in a monotonous shear thinning behavior when the shear rate is increased (Figure 31a). It can be seen that when the S3 amount was increased, the viscosity decreased due to this lubricating effect. It must also be mentioned that the

suspension 25 S3 still had a yield stress behavior, as the particles were still (slightly) **weakly flocculated** and the attractive van der Waals forces were dominant, while suspensions 50 S3 and 75 S3 had **well dispersed** particles, with unmeasurable (Figure 33), but calculated weak yield point (Table 3) behavior. For these suspensions, a plateau of viscosity at high shear rates (above 100 s^{-1}) was observed (Figure 31). Such behavior was previously attributed to the domination of viscous forces at such high shear rates and a hydrodynamically controlled structure [175].

It can be concluded that the chain length and thickness of the steric barrier are not the only parameters that affect the flowability of the suspensions. It is also important to understand and control the conformation of the steric barrier which varied with combination of surfactants as hypothesised in *hypothesis 1*, and the means of steric interaction (elastic vs mixing stabilization) to achieve desired flow behavior of suspensions with weakly flocculated or well dispersed particles.

5.1.2 The role of attractive potential magnitude and conformation of steric barrier on the viscoelastic behavior of suspensions

Presented in Figure 34, the storage (G′) and loss (G″) moduli of the suspensions provide valuable information on how the conformation of the steric barrier and the particle interactions i.e., the magnitude of weak flocculation affect the viscoelastic behavior. Prior to solidification, G″ > G′ was observed for all suspensions, which represents a liquid-like behavior [136].

In the case of **weakly flocculated suspensions** (100 SA and 15 S3, residing in regions 1 and 2), the storage and loss moduli were insensitive to changes in the temperature due to a strong attractive particle network (-8 $x10^{-20}$ J) present in these suspensions. The particles resided in the secondary minimum and the increase in temperature was not sufficient to disrupt the strong attractive network, which meant that the particles continued residing in the secondary minimum, despite the change of temperature, therefore, storage and loss moduli were not changed. Prior to solidification, for suspension 100 SA moduli were approximately 2000 Pa, while for suspensions 15 S3 and 25 S3, similar behavior was observed with lower values of 250–700 Pa at the initial temperature of 100 °C. These values were significantly lower than those obtained for highly loaded zirconia pastes used for direct ink writing, where both G′ and G″ were on the scale of 10^5 Pa [138]. Similarly, the values obtained in this work were much lower than those obtained for zirconia filaments with 50 vol% TZ-3YS-E (10^5 to 10^6 Pa), used for fused filament fabrication [51].

On the other hand, for suspensions 50 S3, 75 S3, and 100 S3, where the particles were **well dispersed**, G′ and G″ were affected by temperature changes and were in the 10–100 Pa range. The increase in thermal energy, resulting from the increased temperature, was able to overcome the very weak attractive forces (-2 to -1 $x10^{-20}$ J) and disturb the attractive interparticle structure present in these suspensions. The increased temperature also caused a decrease in the viscosity of the system, as well as an increase in the available volume due to expansion of the binder wax, therefore, the particles were able to move more freely to larger interparticle distances, where there were fewer particle interactions and a weaker particle network, causing a decrease in the moduli [176]. With the increase of S3 ratio, increased interparticle distances and lower magnitude of weak flocculation led to the expected decrease in G′ and G″ moduli, similar to the observations in the literature by Bell et al. [128].

For suspension 100 S3 (from region 1 in Figure 46), the largest decrease of both moduli was observed, as this suspension had the largest interparticle distance and the weakest particle network. For suspensions 50 S3 and 75 S3 (from region 3 in Figure 46), the decrease

in moduli with increased temperature was attributed to the lubricating effects of compressed surfactants, which was not the case for the suspensions from Region 2, where the surfactants were overlapping, and the particle movement was more restricted.

Shown in Figure 49a, amplitude sweep measurements were done in order to define the linear viscoelastic region (LVER), for suspensions 100 SA, 50 S3 and 100 S3. Following, using a shear strain value of 0.03%, which was in the defined LVER, temperature sweep measurements were repeated for suspensions 100 SA and 100 S3 (Figure 49b). The results of these measurements were compared to previously obtained G′ and G″ moduli values, and for weakly flocculated suspension of 100 SA, two order of magnitude higher values were obtained, due to lower strain values used in these measurements. In this case, the attractive particle network was able to withstand the applied stress better than previously, resulting in higher values of G′ and G″ moduli. For suspension 100 S3, however, one order of magnitude higher values were obtained, as in this case the well dispersed particles were able to move almost as freely as previously. It can be concluded that measurements in LVER provide information on the behavior of the suspensions at close-to-rest conditions (as present while the droplets are airborne and solidified on the print bed during T3DP) while the measurements after the crossover of G′ and G″ moduli provide information on the behavior of the suspensions during flow conditions (as observed during expansion and receding of the deposited droplets).

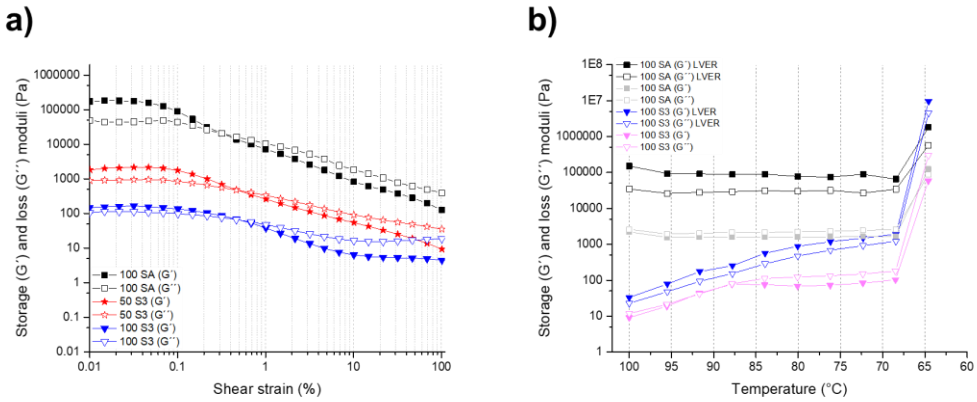


Figure 49: a) Defining the LVER for suspensions 100 SA, 50 S3 and 100 S3, b) temperature sweep in defined LVER conditions for suspensions 100 SA and 100 S3.

In conclusion, a large difference in the magnitude of the storage and loss modulus was observed between suspensions with weakly flocculated particles and well dispersed ones. For the suspensions with weakly flocculated particles and attractive network, values of moduli were in the range of 200–3000 Pa while for suspensions with well-dispersed particles, 2 orders of magnitude less values at 10–100 Pa were observed, which indicates the differences in the strength of the networks formed in these suspensions. This difference was in agreement with those observed from yield stress measurements where at shear stress of 40 Pa, a shear strain of 0.03% was observed for 100 SA while 100 S3 had a shear strain of 10000%, 6 orders of magnitude larger, indicating a larger distortion of the structure for suspensions with well dispersed particles due to a less strong particle network compared to those with weakly flocculated particles.

5.2 Droplet Jetting Dynamics as a Function of Rheological Properties

Reynolds number, Weber number, and inverse of Ohnesorge number have been used as indicators of printability for Newtonian fluids, however, they are not as applicable to non-Newtonian fluids due to the dependence of rheological parameters on the shear rate [135]. For non-Newtonian feedstocks, at a given shear rate, *Re* was calculated, and values followed a trend where the increased amount of long chain surfactant and consequential decrease in viscosity resulted in an increase in *Re* (Table 3). Since *Re* is the ratio between inertial and viscous forces in the system [146], observed increase in *Re* is attributed to the decrease of the viscous forces when the chain length is increased and the particles are well dispersed. It was shown that feedstocks with higher *Re* had better printability (Figure 39), up to *Re* = ~0.4, above which the deposition of a single layer was not possible anymore. As it was shown impossible to deposit single layers with feedstocks that had the lowest *Re* numbers (~0.01), where the viscous forces were dominant, it can be concluded that the *Re* needs to be in a certain range, indicating a balance of inertial and viscous forces, to ensure jettability.

In the case of T3DP used in this work, pressure was applied to all feedstocks during jetting, in order to overcome the viscous forces and ensure flow of feedstock from the nozzle, similar to previous reports in the literature [86], [177]. Application of pressure and the downwards movement of the tappet provided kinetic energy to the material that was deposited (Figure 9) which were necessary as the feedstocks used in this work had higher viscosity values than those of aqueous slurries reported in the literature, such as 30 vol% Si_3N_4 suspension used for drop-on-demand jetting [178]. The energy provided to the system was subject to viscous dissipation in case of highly loaded feedstocks (40 vol%) with high viscosity (up to 500 Pa · s at rest), and the undissipated energy was used to overcome the viscous forces in order to achieve deposition of feedstocks. In case of no applied pressure and low kinetic energy provided by the tappet, the material would be kept in the nozzle under the effect of fluid/air surface tension [179] and could not have been deposited.

In the present work, two main droplet jetting behaviors were observed. First, jetting of non-Newtonian feedstocks, 100 SA **(region 1)** and 15 S3 **(region 2),** exhibiting pronounced shear-thinning and non-monotonous behavior, and **weak flocculation** of particles with a yield stress of 55 Pa, resulted in droplets with **bump (tail) formation**. The deposited column of material was not retracted to the shape of a droplet while airborne, due to strong viscous forces [142] (also represented by low *Re* values of 0.014 and 0.016), as shown in Figure 35. These values of Reynolds number were significantly lower than those reported for the printable region of Newtonian fluids, where $Re<100$ was shown [144]. The result of non-retracted tails was bumps on the droplets, which was also previously explained by the breaking of the continuous feedstock column due to the movement of the print bed, shown in Figure 21 [142]. Observation of single lines revealed that the lines of feedstocks 100 SA and 15 S3 had the same bumps as individual droplets therefore, it was not possible to form a continuous line. Furthermore, the largest droplet diameters were observed for feedstocks 100 SA and 15 S3 (Figure 37). These feedstocks had very low viscosity (of ~0.3–0.5 Pa · s) at the maximum shear rate of 1000 s^{-1}, which was the maximum possible value used for the rheological measurements (to prevent slipping). Namely, the highest possible shear rates were representative of the shear rates present in the nozzle head (2000–3000 s^{-1}) (Figure 31), which resulted in a minimal viscous dissipation and large final kinetic energy applied on the deposited part. The kinetic energy, that was transformed to potential energy during impact (droplet deposition) resulted in the largest spreading of the droplet on the print bed. After this step, due to surface tension,

the droplet receded, and the diameter decreased, but the absence of shear at the print bed resulted in a 3 orders of magnitude increase in viscosity of the feedstock. The viscous force prevented the surface tension from retracting the droplets any further prior to solidification. This also explains the formation of the bump on the droplets due to high viscous forces, the surface tension could not retract the bump and generate the form of a droplet prior to solidification (Figure 35). It was not possible to deposit a single layer either, due to too high viscous forces, causing a build-up of feedstock on the nozzle (Figure 39). The kinetic energy that was applied to this feedstock with the movement of the tappet, as well as the applied pressure, was insufficient to overcome the viscous forces completely.

The second droplet jetting behavior was observed for the feedstocks, 25 S3, 50 S3, and 75 S3 (**region 3**), which had increased steric barrier thickness and less pronounced yield stress compared to the previously discussed feedstocks. The droplets of these feedstocks **did not exhibit non-receded bump/tail**, indicating that the surface tension was able to overcome the viscous forces which were weaker than the previous two feedstocks (100 SA and 15 S3). Feedstock 25 S3 (**region 3**) was a boundary between the printable and non-printable feedstocks. It was interesting to see a different droplet jetting behavior compared to feedstock 15 S3 (**region 2**), as these two **weakly flocculated** feedstocks had almost the same steric barrier thickness (2.4 vs 2.8 nm) and yield stress (55 vs 45 Pa). However, it has to be noted that there was a 4-times difference in the viscosities (14.9 vs 3.7 Pa $\cdot$ s) and Re values (0.016 vs 0.064) for 15 S3 and 25 S3. Such a difference obviously originates from the configuration of the steric barrier, where the lubrication effects introduced by compressed surfactants led to decreased viscous forces for feedstock 25 S3, and consequently, surface tension was able to overcome the viscous forces and a bump-free droplet was achieved. For the feedstock 25 S3, even though the deposition of a single layer was completed, the layer had some visible flaws, also supported by the Sa value of 24 µm obtained for this sample.

On the other hand, in the case of feedstocks 50 S3 and 75 S3 **(region 3)** with **well dispersed** particles, the compressed configuration of surfactant chains and reduced viscous forces (Re values of 0.1 and 0.265) allowed the retraction of the tail back to the main body of the droplet. For these feedstocks with less pronounced viscous forces, the surface tension was able to overcome the viscous forces and minimize the surface area, and the final droplets had a smaller diameter compared to those with high viscous forces. Lower S_a values of 13 and 18 µm were obtained for feedstocks 50 S3 and 75 S3, and these feedstocks resulted in higher homogeneity and reliability of the deposited single layers. Feedstock 75 S3 was used for the successful 3D printing of demonstrators with various geometrical complexities, such as an impeller, a tetrahedron, and a honeycomb disc, as shown in Figure 50.

In the case when particles in the feedstocks were **well dispersed** (100 S3; **region 1**), the viscous forces were lower than the rest of the feedstocks, exhibiting the highest Re value in this work (~ 0.4). Even though for this feedstock, deposition of droplets and lines was possible and they exhibited the nicest shapes and accuracy, it was found that deposition of a single complete layer was still not possible, disproving *hypothesis 3*. This was attributed to the lack of yield stress, low viscosity, and pseudo-Newtonian behavior observed in this feedstock at given processing parameters, leading to a very low viscous dissipation during jetting. This meant that the deposited droplets carried a high kinetic energy, and the deposited layer was inconsistent and had an accumulation of the material in different areas. It is believed that by optimizing the process parameters, such as pressure, temperature at the nozzle, and print bed temperature, it should be possible to print this feedstock as well.



Figure 50: Printing demonstrators with one of the "suitable" feedstocks, 75 S3 [151].

Finally, it can be summed up that the feedstocks in **region 3** of Figure 46, labeled as *compression region*, resulted in the deposition of droplets, lines, and layers with minimal flaws. In this region suspension 25 SA had the yield stress of 45 Pa while other suspensions did not have yield stress, while a monotonous shear thinning behavior and the steric barrier thickness of 2.8–9.4 nm were present. Feedstocks in this region included **well dispersed** as well as **weakly flocculated** particles. These findings disproved *hypothesis 2*. An important parameter was found to be the compression of the surfactants, which led to boundary lubrication and decreased viscosity values. *Re* was found to be 0.064–0.265 for the suspensions in this region. These limits were summarized in Figure 51 as a "*roadmap*" for the properties of suspensions used as feedstocks, where the limits of yield stress were indicated in gray and those for loss modulus, in green. Use of combination of surfactants with significantly different chain lengths presented a lubricating effect due to the possibility of achieving compressed configuration. It can be concluded that for highly loaded non-Newtonian feedstocks, control of rheological behavior as well as steric barrier thickness and configuration is desired for "successful" deposition. Here, it is also important to emphasize that the steric barrier thickness is not the sole parameter defining the jetting behavior of the feedstocks and use of a single surfactant, leading to the same steric barrier thickness would not result in the same jetting behavior as observed here, due to the lack of lubricating effect that was achieved thanks to compression of the long chain surfactant.

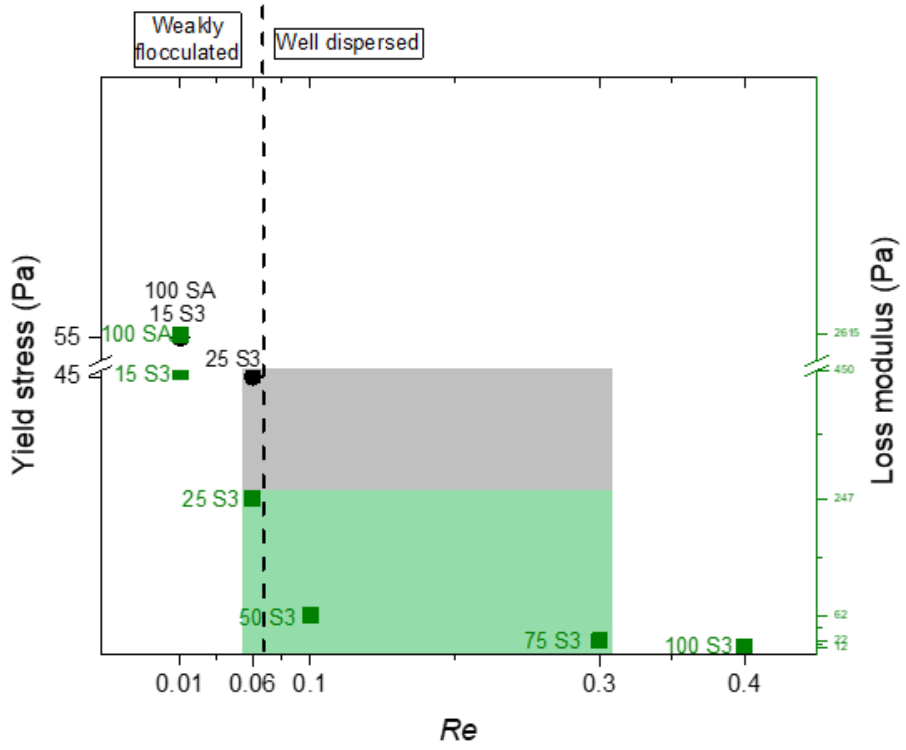


Figure 51: Roadmap for jettability of feedstocks for T3DP.

5.3 The Role of Droplet Deposition and Infill Strategy on the Strength and Flaw Type Population

T3DP AM process was employed to fabricate a series of printed and sintered rectangular bending bars, where the role of droplet deposition and infill strategy on the mechanical properties was investigated by 4-point bending strength test. Using Weibull analysis and fractography, it was possible to analyse and compare the flaw type population and reliability of fabricated parts to other extrusion-based AM methods, such as FFF.

Feedstock inhomogeneities, such as the presence of agglomerates, were one source of defects observed in parts [180]. Agglomerates in the feedstock could cause clogging of the nozzle, which leads to **inconsistent droplet deposition** as observed for our systems in Figure 44c, Figure 44f, Figure 44g. Shown in Figure 44c, a large defect of 150 µm could indicate the inconsistent droplet deposition, as the size of the defect was similar to the height of a droplet (160 µm). It is important to improve the feedstock preparation and remove agglomerates from the feedstocks, to minimize the introduction of flaws. Nevertheless, compared to other AM methods, T3DP is more insensitive to feedstock induced flaws. It was shown for parts prepared by SLA that pores were a recurring flaw, introduced by feedstock preparation as well as process parameters [62].

Process induced flaws, on the other hand, were also present in the printed parts. Fractography results showed that the defects observed for all infill strategies were mainly due to **the imperfect fusion of subsequent droplets** (inset of Figure 44a, Figure 44b, and Figure 44d), as well as **imperfect fusion of subsequent lines** (Figure 44f). To understand the reason for such behavior, a detailed analysis of the coordinates of deposited droplets used for the print jobs was made, where the positioning of every single droplet for

all infill strategies could be observed, as presented in Figure 52, Figure 53, and Figure 54 [54]. Blue dots show the position of droplets for 0° infill strategy while green dots indicate droplet positions for 90° infill strategy. The movement of the print head was shown with continuous lines. As presented in Figure 52, for 0° infill strategy, droplets were deposited along the x direction, and subsequent layers consisted of droplets that were deposited at the exact same position. A similar situation was observed for the 90° infill strategy (Figure 53), where the deposition was done in the y direction. For the 0° + 90° infill strategy, however, as the droplets in subsequent layers were not positioned on top of each other due to the change of infill strategy on each layer (Figure 54), as well as the differences in the diameter of droplets in the direction of printing ($d_{//}$) and in the direction perpendicular to printing ($d_{\perp}$), shown in Figure 37, large (number of) defects as indicated by yellow arrows in micro-CT images in Figure 55c were observed. As seen in Figure 55a and Figure 55b, parts prepared by 0° and 90° infill strategies had smaller defects.

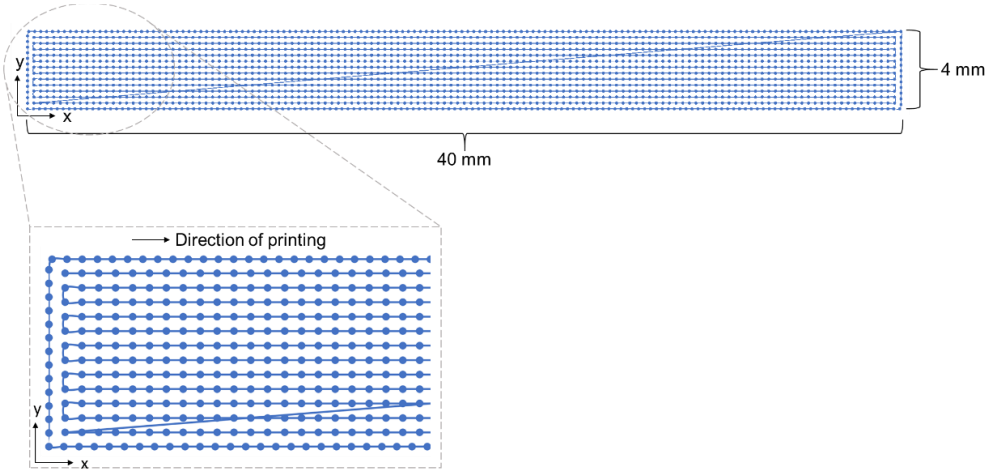


Figure 52: Droplet positioning of 0° infill strategy [54].

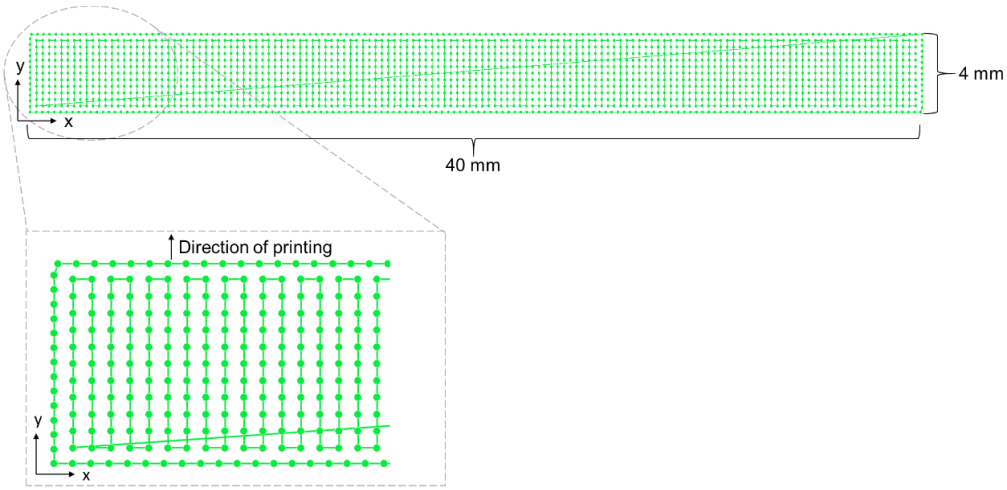


Figure 53: Droplet positioning of 90° infill strategy [54].

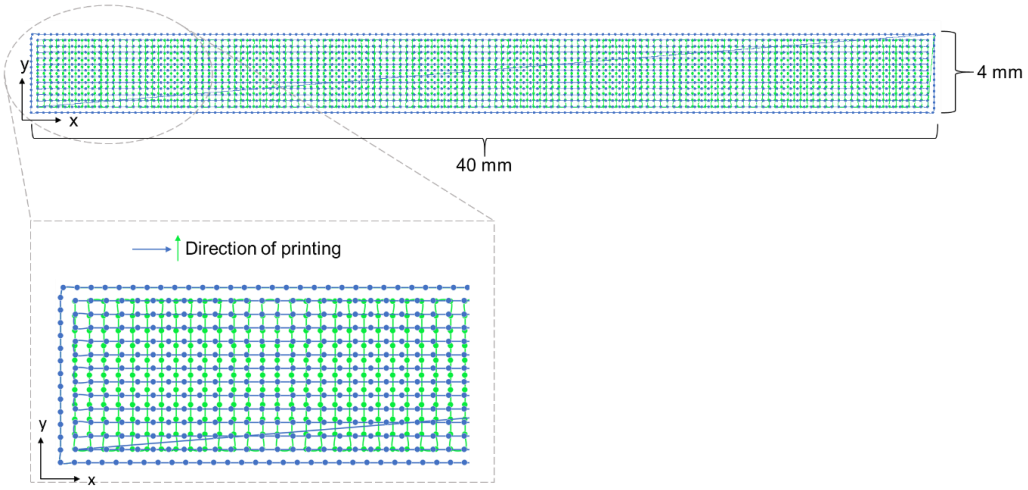


Figure 54: Droplet positioning of 0° + 90° infill strategy [54].

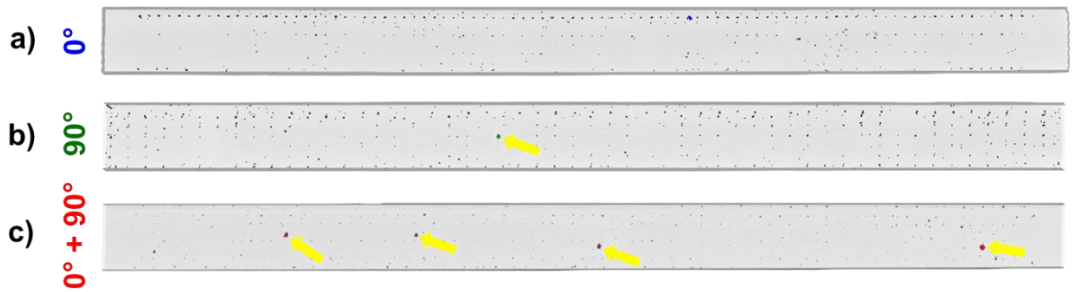


Figure 55: Total volumetric population of defects present in a) 0°, b) 90°, and c) 0° + 90° infill strategy.

4-point bending test results were summarized in Table 5, showing that even though the results achieved for 0° were slightly superior to the rest of the infill strategies, the differences were negligible which disproved *hypothesis 4*. It could be concluded that the mechanical properties were (almost) insensitive to the changes in the infill strategy, which is not usually the case for other extrusion-based AM methods. Namely, for parts prepared by FFF, differences in mechanical properties were observed when the infill strategy was changed, mainly due to pores and voids as a result of poor fusion between deposited filament lines and layers [181]. The voids present between deposited filaments are a common flaw present in parts prepared by FFF, not only for ceramic loaded filaments [182], [183]. It was recently shown in a review by Staudacher et al. [184] that parts prepared by material extrusion commonly have flaws such as delamination, pores, and voids, marked yellow in Figure 56.

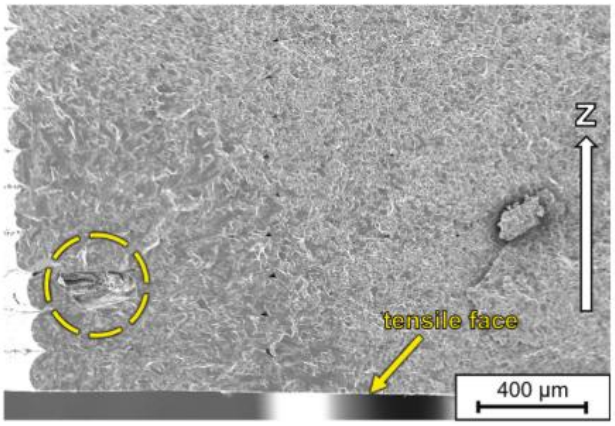


Figure 56: Voids present in alumina 4-point bending bars, prepared by material extrusion [184].

While the strength values were insensitive to the changes in the infill strategies for parts prepared by T3DP, it must be noted that the parts had low Weibull moduli (m = 6.0 to 7.0), compared to other AM processes. For zirconia parts prepared by SLA, Weibull modulus up to m = 9.3–16.0 was shown to be possible [165], [185] while for FFF, Weibull modulus m = 5.7–9.9 was achieved [50], [186]. The low values of Weibull moduli obtained by T3DP can be improved by better controlling of droplet positioning in the parts by altering the coordinates of the deposition in the slicing software, as well as by ensuring that the droplet diameter in different directions is as similar as possible, which can be achieved by lowering the travel speed of the print head to avoid elongation in one direction.

Chapter 6

Conclusions

This work aimed to deepen the understanding of jetting of highly loaded thermoplastic ceramic feedstocks with thermoplastic 3D printing and was divided into two parts. In the first part, the feedstock properties and their jetting were studied, while the second part focused on the process parameters and the mechanical properties of the final parts.

In the first part of this thesis, the focus was on the colloidal particle interactions, the effect of steric barrier thickness, and conformation on the flowability of suspensions used for T3DP. The thickness of the steric barrier was changed by using different combinations of a short chain and long chain surfactant. It was concluded that the suspensions with shorter steric barriers had weakly flocculated particles, resulting in higher viscosities and non-monotonous shear thinning behavior with distinct yield stress behavior. On the other hand, suspensions with increased steric barrier thickness resulted in lower viscosities, monotonous shear thinning behavior, and low/non-existent yield stress. Suspensions with weakly flocculated particles had values of storage and loss moduli in the range of 200–3000 Pa while suspensions with well dispersed particles had 2 orders of magnitude lower values of 10–100 Pa. These values showed that the increased attractive potential of the suspensions with weakly flocculated particles increased the strength of the particle network, resulting in high moduli values. Conformation of the steric barrier was shown to be a very crucial parameter. It was shown that steric barrier could have certain conformations: rigid, overlapping, and compression. Compression conformation was shown to provide decreased viscosity and increased jettability of the feedstocks, which was attributed to the introduction of the boundary lubrication effect. It was shown that this lubrication allowed jetting of feedstocks with both weakly flocculated and well dispersed particles. It was concluded that using a combination of surfactants with significantly different chain lengths allowed the compression conformation and the lubricating effect, and finally improved the jetting of feedstocks. Depending on the composition and rheological properties of the feedstock, two main droplet jetting behaviors were observed. Feedstocks exhibiting pronounced shear-thinning and non-monotonous behavior, and weak flocculation of particles with a yield stress of >50 Pa, resulted in droplets with the non-receded bump (tail) formation (after solidification). On the other hand, feedstocks with increased steric barrier thickness and less pronounced yield stress resulted in jetting of droplets with no bump formation, indicating that the surface tension was able to overcome the viscous forces present in these feedstocks. It was possible to deposit droplets, lines, and layers with minimal flaws using feedstocks in the compression region. In this region, the feedstocks had yield stress values below 45 Pa, a monotonous shear thinning behavior, and the steric

barrier thickness of 2.8–9.4 nm. Re was found to be 0.064–0.265 for the feedstocks in this region.

In the second part of the thesis, the effect of droplet deposition and infill strategy on the strength and flaw type population of sintered zirconia bending bars was studied. Use of different infill strategies resulted in negligible differences in the mechanical properties, and it was concluded that the mechanical properties were (almost) insensitive to the changes in the infill strategy, unlike other extrusion-based AM processes such as FFF. It was shown that the flaws present in parts prepared by T3DP were either due to feedstock inhomogeneities or were process induced. However, compared to other AM processes such as SLA, T3DP was found to be more insensitive to feedstock induced flaws. Process induced flaws were found to be the imperfect fusion of subsequent droplets and lines that were attributed to the imperfect positioning of the droplets in consequential lines and layers as well as differences in diameter. The imperfect fusion and positioning of droplets, that can certainly be improved, were found to be the main reason for the low Weibull moduli ($m =$ 6.0 to 7.0) which was observed for parts prepared by T3DP. Improving both feedstock properties and process parameters is necessary for manufacturing parts with increased mechanical properties and reliability.

In conclusion, this thesis provided an insight into the complete process of T3DP, covering a range of crucial steps starting from (rheological) properties of suspensions, and their effect on jettability, to process parameters and their effect on the final (mechanical) properties of the parts. The thesis delivers a "*roadmap*" for the design of the steric barrier thickness and configuration, which governs various rheological properties of the feedstocks, with defined boundaries for the successful jetting outcome, going beyond the state of the art for T3DP. By exploiting the feedstock properties and process details, improvement of the current state of art for T3DP was achieved, which would allow preparation of complex parts with good qualities that can be used in many different fields as dentistry, biomedicine, catalysis, semiconductor industry and others. Furthermore, understanding the properties of feedstock would facilitate the introduction of new feedstock formulations, the development of novel composites, and the creation of multi-material parts that can even mimic the complex structures of natural materials. However, understanding the interparticle interactions and resulting rheological behavior of highly-loaded paraffin-wax suspensions used as feedstocks for T3DP is essential for its successful implementation.

References

[1] Z. Chen *et al.*, "3D printing of ceramics: A review," *J. Eur. Ceram. Soc.*, vol. 39, no. 4, pp. 661–687, 2019, doi: 10.1016/j.jeurceramsoc.2018.11.013.

[2] N. Travitzky *et al.*, "Additive manufacturing of ceramic-based materials," 2014, doi: 10.1002/adem.201400097.

[3] Y. Lakhdar, C. Tuck, J. Binner, A. Terry, and R. Goodridge, "Additive manufacturing of advanced ceramic materials," *Progress in Materials Science*, vol. 116. Elsevier Ltd, Feb. 01, 2021, doi: 10.1016/j.pmatsci.2020.100736.

[4] R. M. German, P. Suri, and S. J. Park, "Review: Liquid phase sintering," *J. Mater. Sci.*, 2009, doi: 10.1007/s10853-008-3008-0.

[5] R. Moreno, "Better ceramics through colloid chemistry," *J. Eur. Ceram. Soc.*, vol. 40, no. 3, pp. 559–587, 2020, doi: 10.1016/j.jeurceramsoc.2019.10.014.

[6] G. V. Franks, C. Tallon, A. R. Studart, M. L. Sesso, and S. Leo, "Colloidal processing: enabling complex shaped ceramics with unique multiscale structures," *J. Am. Ceram. Soc.*, vol. 100, no. 2, pp. 458–490, 2017, doi: 10.1111/jace.14705.

[7] H. M. Tülümen, T. Hanemann, V. Piotter, and D. Stenzel, "Investigation of feedstock preparation for injection molding of oxide–oxide ceramic composites," *J. Manuf. Mater. Process.*, vol. 3, no. 1, pp. 4–8, 2019, doi: 10.3390/jmmp3010009.

[8] L. Gorjan, "Wick Debinding - An Effective Way of Solving Problems in the Debinding Process of Powder Injection Molding," *Some Crit. Issues Inject. Molding*, 2012, doi: 10.5772/34969.

[9] A. Barazanchi, K. C. Li, B. Al-Amleh, K. Lyons, and J. N. Waddell, "Additive Technology: Update on Current Materials and Applications in Dentistry," *J. Prosthodont.*, vol. 26, no. 2, pp. 156–163, 2017, doi: 10.1111/jopr.12510.

[10] I. Özden, A. Iveković, and A. Kocjan, "Additive manufacturing of ceramics from thermoplastic feedstocks," *Open Ceram.*, vol. 6, no. April, 2021, doi: 10.1016/j.oceram.2021.100129.

[11] "ISO/ASTM, 17296 Standard on Additive Manufacturing (AM) Technologies."

[12] S. A. M. Tofail, E. P. Koumoulos, A. Bandyopadhyay, S. Bose, L. O'Donoghue, and C. Charitidis, "Additive manufacturing: scientific and technological challenges, market uptake and opportunities," *Mater. Today*, vol. 21, no. 1, pp. 22–37, 2018, doi: 10.1016/j.mattod.2017.07.001.

[13] C. W. Hull, "Apparatus for production of three-dimensional objects by stereolithography. U.S. Patent No 4,575,300. Washington DC: Patent and Trademak Office," 1986.

[14] E. Sachs, M. Cima, and J. Cornie, “Three-Dimensional Printing: Rapid Tooling and Prototypes Directly from a CAD Model,” *CIRP Ann. - Manuf. Technol.*, 1990, doi: 10.1016/S0007-8506(07)61035-X.

[15] A. Zocca, P. Colombo, C. M. Gomes, and J. Günster, “Additive Manufacturing of Ceramics: Issues, Potentialities, and Opportunities,” *J. Am. Ceram. Soc.*, vol. 98, no. 7, pp. 1983–2001, 2015, doi: 10.1111/jace.13700.

[16] J. C. Wang, H. Dommati, and S. J. Hsieh, “Review of additive manufacturing methods for high-performance ceramic materials,” *Int. J. Adv. Manuf. Technol.*, vol. 103, no. 5–8, pp. 2627–2647, 2019, doi: 10.1007/s00170-019-03669-3.

[17] L. Rabinskiy, A. Ripetsky, S. Sitnikov, Y. Solyaev, and R. Kahramanov, “Fabrication of porous silicon nitride ceramics using binder jetting technology,” 2016, doi: 10.1088/1757-899X/140/1/012023.

[18] J. A. Gonzalez, J. Mireles, Y. Lin, and R. B. Wicker, “Characterization of ceramic components fabricated using binder jetting additive manufacturing technology,” *Ceram. Int.*, 2016, doi: 10.1016/j.ceramint.2016.03.079.

[19] J. Y. Lee, J. An, and C. K. Chua, “Fundamentals and applications of 3D printing for novel materials,” *Appl. Mater. Today*, vol. 7, pp. 120–133, 2017, doi: 10.1016/j.apmt.2017.02.004.

[20] T. D. Ngo, A. Kashani, G. Imbalzano, K. T. Q. Nguyen, and D. Hui, “Additive manufacturing (3D printing): A review of materials, methods, applications and challenges,” *Compos. Part B Eng.*, vol. 143, no. February, pp. 172–196, 2018, doi: 10.1016/j.compositesb.2018.02.012.

[21] K. Shahzad, J. Deckers, S. Boury, B. Neirinck, J. P. Kruth, and J. Vleugels, “Preparation and indirect selective laser sintering of alumina/PA microspheres,” *Ceram. Int.*, 2012, doi: 10.1016/j.ceramint.2011.08.055.

[22] P. Colombo, J. Schmidt, G. Franchin, A. Zocca, and J. Günster, “Additive manufacturing techniques for fabricating complex ceramic components from preceramic polymers,” *Am. Ceram. Soc. Bull.*, vol. 96, no. 3, pp. 16–23, 2017.

[23] Additive Manufacturing Research Group, “The 7 Categories of Additive Manufacturing,” *Loughborough University*, 2018. .

[24] M. Schwentenwein and J. Homa, “Additive manufacturing of dense alumina ceramics,” *Int. J. Appl. Ceram. Technol.*, vol. 12, no. 1, pp. 1–7, 2015, doi: 10.1111/ijac.12319.

[25] H. Li, L. Song, J. Sun, J. Ma, and Z. Shen, “Stereolithography-fabricated zirconia dental prostheses: concerns based on clinical requirements,” *Adv. Appl. Ceram.*, vol. 119, no. 5–6, pp. 236–243, 2020, doi: 10.1080/17436753.2019.1709687.

[26] E. Zanchetta *et al.*, “Stereolithography of SiOC Ceramic Microcomponents,” *Adv. Mater.*, vol. 28, no. 2, pp. 370–376, 2016, doi: 10.1002/adma.201503470.

[27] A. A. Altun, T. Prochaska, T. Konegger, and M. Schwentenwein, “Dense, strong, and precise silicon nitride-based ceramic parts by lithography-based ceramic manufacturing,” *Appl. Sci.*, 2020, doi: 10.3390/app10030996.

[28] N. Aliheidari, R. Tripuraneni, A. Ameli, and S. Nadimpalli, “Fracture resistance measurement of fused deposition modeling 3D printed polymers,” *Polym. Test.*, vol. 60, pp. 94–101, 2017, doi: 10.1016/j.polymertesting.2017.03.016.

[29] D. Nötzel, R. Eickhoff, and T. Hanemann, "Fused filament fabrication of small ceramic components," *Materials*, vol. 11, no. 8. 2018, doi: 10.3390/ma11081463.

[30] J. Abel *et al.*, "Fused filament fabrication (FFF) of metal-ceramic components," *J. Vis. Exp.*, 2019, doi: 10.3791/57693.

[31] U. Scheithauer *et al.*, "Droplet-based additive manufacturing of hard metal components by thermoplastic 3D Printing (T3DP)," *J. Ceram. Sci. Technol.*, vol. 8, no. 1, pp. 155–160, 2017, doi: 10.4416/JCST2016-00104.

[32] U. Scheithauer, T. Slawik, E. Schwarzer, H. J. Richter, T. Moritz, and A. Michaelis, "Additive manufacturing of metal-ceramic-composites by thermoplastic 3D-printing (3DTP)," *J. Ceram. Sci. Technol.*, 2015, doi: 10.4416/JCST2014-00045.

[33] S. Weingarten *et al.*, "Multi-material ceramic-based components - additive manufacturing of blackand- white zirconia components by thermoplastic 3D-printing (CerAM - T3DP)," *J. Vis. Exp.*, vol. 2019, no. 143, pp. 1–10, 2019, doi: 10.3791/57538.

[34] C. A. Díaz-Moreno *et al.*, "Binder jetting additive manufacturing of aluminum nitride components," *Ceram. Int.*, vol. 45, no. 11, pp. 13620–13627, 2019, doi: 10.1016/j.ceramint.2019.03.187.

[35] S. Huang, C. Ye, H. Zhao, and Z. Fan, "Additive manufacturing of thin alumina ceramic cores using binder-jetting," *Addit. Manuf.*, vol. 29, no. April, p. 100802, 2019, doi: 10.1016/j.addma.2019.100802.

[36] P. Lima, A. Zocca, W. Acchar, and J. Günster, "3D printing of porcelain by layerwise slurry deposition," *J. Eur. Ceram. Soc.*, vol. 38, no. 9, pp. 3395–3400, 2018, doi: 10.1016/j.jeurceramsoc.2018.03.014.

[37] J. Hostaša *et al.*, "Transparent laser ceramics by stereolithography," *Scr. Mater.*, vol. 187, pp. 194–196, 2020, doi: 10.1016/j.scriptamat.2020.06.006.

[38] S. Zakeri, M. Vippola, and E. Levänen, "A comprehensive review of the photopolymerization of ceramic resins used in stereolithography," *Additive Manufacturing*. 2020, doi: 10.1016/j.addma.2020.101177.

[39] J. Deckers, J. Vleugels, and J. P. Kruth, "Additive manufacturing of ceramics: A review," *J. Ceram. Sci. Technol.*, vol. 5, no. 4, pp. 245–260, 2014, doi: 10.4416/JCST2014-00032.

[40] J. Gonzalez-Gutierrez, S. Cano, S. Schuschnigg, C. Kukla, J. Sapkota, and C. Holzer, "Additive manufacturing of metallic and ceramic components by the material extrusion of highly-filled polymers: A review and future perspectives," *Materials (Basel).*, vol. 11, no. 5, 2018, doi: 10.3390/ma11050840.

[41] E. Feilden, E. G. T. Blanca, F. Giuliani, E. Saiz, and L. Vandeperre, "Robocasting of structural ceramic parts with hydrogel inks," *J. Eur. Ceram. Soc.*, vol. 36, no. 10, pp. 2525–2533, 2016, doi: 10.1016/j.jeurceramsoc.2016.03.001.

[42] L. Zema, G. Loreti, A. Melocchi, A. Maroni, and A. Gazzaniga, "Injection Molding and its application to drug delivery," *Journal of Controlled Release*. 2012, doi: 10.1016/j.jconrel.2012.01.001.

[43] C. Aumnate, A. Pongwisuthiruchte, P. Pattananuwat, and P. Potiyaraj, "Fabrication of ABS/Graphene oxide composite filament for fused filament fabrication (FFF) 3D Printing," *Adv. Mater. Sci. Eng.*, vol. 2018, 2018, doi:

10.1155/2018/2830437.

[44] S. Cano *et al.*, "Optimization of material properties for highly-filled thermoplastic polymers used in fused filament fabrication of ceramics," *AIP Conf. Proc.*, vol. 2065, no. February, 2019, doi: 10.1063/1.5088316.

[45] C. Esposito Corcione, F. Scalera, F. Gervaso, F. Montagna, A. Sannino, and A. Maffezzoli, "One-step solvent-free process for the fabrication of high loaded PLA/HA composite filament for 3D printing," *J. Therm. Anal. Calorim.*, vol. 134, no. 1, pp. 575–582, 2018, doi: 10.1007/s10973-018-7155-5.

[46] H. Mei, Y. Yan, L. Feng, K. G. Dassios, H. Zhang, and L. Cheng, "First printing of continuous fibers into ceramics," *J. Am. Ceram. Soc.*, vol. 102, no. 6, pp. 3244–3255, 2019, doi: 10.1111/jace.16234.

[47] S. A. Tronvoll, T. Welo, and C. W. Elverum, "The effects of voids on structural properties of fused deposition modelled parts: a probabilistic approach," *Int. J. Adv. Manuf. Technol.*, vol. 97, no. 9–12, pp. 3607–3618, 2018, doi: 10.1007/s00170-018-2148-x.

[48] C. Kukla, J. Gonzalez-gutierrez, S. Cano, and S. Hampel, "Fused Filament Fabrication (FFF) of PIM Feedstocks," *Proc. VI Congr. Nac. Pulvimetalurgia y I Congr. Iberoam. Pulvimetalurgia*, no. July, 2017.

[49] M. Vukšić, M. Bek, L. S. Perše, M. M. Kržmanc, A. Kocjan, and A. Iveković, "The role of paraffin wax on the properties and printability of ethylene vinyl acetate-based feedstocks for alumina fused filament fabrication," *Open Ceram.*, vol. 16, no. August, 2023, doi: 10.1016/j.oceram.2023.100496.

[50] S. Cano *et al.*, "Influence of the infill orientation on the properties of zirconia parts produced by fused filament fabrication," *Materials (Basel).*, vol. 13, no. 14, 2020, doi: 10.3390/ma13143158.

[51] D. Nötzel, R. Eickhoff, C. Pfeifer, and T. Hanemann, "Printing of zirconia parts via fused filament fabrication," *Materials (Basel).*, vol. 14, no. 19, 2021, doi: 10.3390/ma14195467.

[52] M. Orlovská, Z. Chlup, Bača, M. Janek, and M. Kitzmantel, "Fracture and mechanical properties of lightweight alumina ceramics prepared by fused filament fabrication," *J. Eur. Ceram. Soc.*, vol. 40, no. 14, pp. 4837–4843, 2020, doi: 10.1016/j.jeurceramsoc.2020.02.026.

[53] S. Rangarajan, G. Qi, N. Venkataraman, A. Safari, and S. C. Danforth, "Powder Processing, Rheology, and Mechanical Properties of Feedstock for Fused Deposition of Si3N4 Ceramics," *J. Am. Ceram. Soc.*, vol. 83, no. 7, pp. 1663–1669, 2004, doi: 10.1111/j.1151-2916.2000.tb01446.x.

[54] I. Özden, U. Scheithauer, A. Iveković, and A. Kocjan, "Effect of infill strategy on the flexural strength of 3Y-TZP bars fabricated by thermoplastic 3D printing (T3DP)," *Open Ceram.*, vol. 14, no. February, 2023, doi: 10.1016/j.oceram.2023.100367.

[55] C. L. Gnanasagaran, K. Ramachandran, V. H. Kumar, V. Ramachandran, and M. Rangarajan, "Influence of infill patterns on mechanical properties of 3D printed Al2O3 ceramics via fused filament fabrication," *Ceram. Int.*, vol. 50, no. 10, pp. 17796–17806, 2024, doi: 10.1016/j.ceramint.2024.02.269.

[56] G. D. Goh, Y. L. Yap, H. K. J. Tan, S. L. Sing, G. L. Goh, and W. Y. Yeong, "Process–Structure–Properties in Polymer Additive Manufacturing via Material Extrusion: A Review," *Crit. Rev. Solid State Mater. Sci.*, vol. 45, no. 2, pp. 113–133, 2020, doi: 10.1080/10408436.2018.1549977.

[57] S. Iyer *et al.*, "Microstructural characterization and mechanical properties of Si3N4 formed by fused deposition of ceramics," *Int. J. Appl. Ceram. Technol.*, vol. 5, no. 2, pp. 127–137, 2008, doi: 10.1111/j.1744-7402.2008.02193.x.

[58] O. Lame, D. Bellet, M. Di Michiel, and D. Bouvard, "In situ microtomography investigation of metal powder compacts during sintering," 2003, doi: 10.1016/S0168-583X(02)01690-7.

[59] R. M. German, "Thermodynamics of sintering," in *Sintering of Advanced Materials*, 2010.

[60] Y.-M. Chiang, D. P. Birnie, and W. D. Kingery, *Physical Ceramics*. 1997.

[61] G. R. Hatanaka, G. S. Polli, L. M. G. Fais, J. M. dos S. N. Reis, and L. A. P. Pinelli, "Zirconia changes after grinding and regeneration firing," *J. Prosthet. Dent.*, vol. 118, no. 1, pp. 61–68, 2017, doi: 10.1016/j.prosdent.2016.09.026.

[62] W. Harrer, M. Schwentenwein, T. Lube, and R. Danzer, "Fractography of zirconia-specimens made using additive manufacturing (LCM) technology," *J. Eur. Ceram. Soc.*, vol. 37, no. 14, pp. 4331–4338, 2017, doi: 10.1016/j.jeurceramsoc.2017.03.018.

[63] M. Wendler *et al.*, "Chairside CAD/CAM materials. Part 2: Flexural strength testing," *Dent. Mater.*, vol. 33, no. 1, pp. 99–109, 2017, doi: 10.1016/j.dental.2016.10.008.

[64] R. Danzer, P. Supancic, J. Pascual, and T. Lube, "Fracture statistics of ceramics - Weibull statistics and deviations from Weibull statistics," *Eng. Fract. Mech.*, vol. 74, no. 18, pp. 2919–2932, 2007, doi: 10.1016/j.engfracmech.2006.05.028.

[65] S. Karakoca and H. Yilmaz, "Influence of surface treatments on surface roughness, phase transformation, and biaxial flexural strength of Y-TZP ceramics," *J. Biomed. Mater. Res. - Part B Appl. Biomater.*, vol. 91, no. 2, pp. 930–937, 2009, doi: 10.1002/jbm.b.31477.

[66] R. Danzer, T. Lube, P. Supancic, and R. Damani, "Fracture of ceramics," *Adv. Eng. Mater.*, vol. 10, no. 4, pp. 275–298, 2008, doi: 10.1002/adem.200700347.

[67] R. Huang *et al.*, "Material extrusion and sintering of binder-coated zirconia: Comprehensive characterizations," *Addit. Manuf.*, vol. 45, no. May, p. 102073, 2021, doi: 10.1016/j.addma.2021.102073.

[68] V. Lang *et al.*, "Process data-based knowledge discovery in additive manufacturing of ceramic materials by multi-material jetting (CerAM MMJ)," *J. Manuf. Mater. Process.*, vol. 4, no. 3, 2020, doi: 10.3390/JMMP4030074.

[69] J. A. Lewis, J. E. Smay, J. Stuecker, and J. Cesarano, "Direct ink writing of three-dimensional ceramic structures," *J. Am. Ceram. Soc.*, vol. 89, no. 12, pp. 3599–3609, 2006, doi: 10.1111/j.1551-2916.2006.01382.x.

[70] D. H. Lee and B. Derby, "Preparation of PZT suspensions for direct ink jet printing," *J. Eur. Ceram. Soc.*, vol. 24, no. 6, pp. 1069–1072, 2004, doi: 10.1016/S0955-2219(03)00421-7.

[71] U. Scheithauer *et al.*, "Investigation of Droplet Deposition for Suspensions Usable

for Thermoplastic 3D Printing (T3DP)," *J. Mater. Eng. Perform.*, 2018, doi: 10.1007/s11665-017-2875-4.

[72] "Microdispensing System MDS 3280," 2020.

[73] U. Scheithauer *et al.*, "Ceramic-Based 4D Components: Additive manufacturing (AM) of ceramic-based functionally graded materials (FGM) by thermoplastic 3D printing (T3DP)," *Materials (Basel).*, vol. 10, no. 12, 2017, doi: 10.3390/ma10121368.

[74] Z. Li, J. Yang, K. Li, L. Zhu, and W. Tang, "Fabrication of PDMS microfluidic devices with 3D wax jetting," *RSC Adv.*, vol. 7, no. 6, pp. 3313–3320, 2017, doi: 10.1039/C6RA24884E.

[75] J. E. Zorzi, C. A. Perottoni, and J. A. H. Da Jornada, "Hard-skin development during binder removal from Al2O3-based green ceramic bodies," *J. Mater. Sci.*, vol. 37, no. 9, pp. 1801–1807, 2002, doi: 10.1023/A:1014949923939.

[76] S. Novak, S. M. H. Olhero, J. M. F. Ferreira, and A. Zupančič, "Rheological properties of paraffin suspensions of surface-modified alumina powder for low-pressure injection moulding," *Rheol. Acta*, vol. 43, no. 5, pp. 559–566, 2004, doi: 10.1007/s00397-004-0401-8.

[77] U. Scheithauer, E. Schwarzer, H. J. Richter, and T. Moritz, "Thermoplastic 3D printing - An additive manufacturing method for producing dense ceramics," *Int. J. Appl. Ceram. Technol.*, 2015, doi: 10.1111/ijac.12306.

[78] U. Scheithauer, A. Bergner, E. Schwarzer, H. J. Richter, and T. Moritz, "Studies on thermoplastic 3D printing of steel-zirconia composites," *J. Mater. Res.*, vol. 29, no. 17, pp. 1931–1940, 2014, doi: 10.1557/jmr.2014.209.

[79] "AMAREA- Premium Materials Overview." https://www.amarea.de/materials.

[80] U. Scheithauer, R. Johne, L. Gottlieb, S. Weingarten, H. Wiemer, and S. Holtzhausen, "Recent developments in the field of additive manufacturing of ceramic-based multi-material components open the door to highly functionalized components," *Prog. Addit. Manuf.*, no. 0123456789, 2025, doi: 10.1007/s40964-025-01112-6.

[81] L. Gorjan, A. Dakskobler, and T. Kosmač, "Strength evolution of injection-molded ceramic parts during wick-debinding," *J. Am. Ceram. Soc.*, vol. 95, no. 1, pp. 188–193, 2012, doi: 10.1111/j.1551-2916.2011.04872.x.

[82] L. Gorjan, T. Lusiola, D. Scharf, and F. Clemens, "Kinetics and equilibrium of Eco-debinding of PZT ceramics shaped by thermoplastic extrusion," *J. Eur. Ceram. Soc.*, vol. 37, no. 16, pp. 5273–5280, 2017, doi: 10.1016/j.jeurceramsoc.2017.04.063.

[83] J. K. Wright and J. R. G. Evans, "Removal of organic vehicle from moulded ceramic bodies by capillary action," *Ceram. Int.*, 1991, doi: 10.1016/0272-8842(91)90014-Q.

[84] S. W. Kim, H. W. Lee, and H. Song, "Effect of minor binder on capillary structure evolution during wicking," *Ceram. Int.*, vol. 25, no. 7, pp. 671–676, 1999, doi: 10.1016/S0272-8842(98)00082-0.

[85] S. Novak, A. Dakskobler, and V. Ribitsch, "The effect of water on the behavior of alumina-paraffin suspensions for low-pressure injection moulding (LPIM)," *J. Eur. Ceram. Soc.*, 2000, doi: 10.1016/S0955-2219(00)00083-2.

[86] K. A. M. Seerden, N. Reis, J. R. G. Evans, P. S. Grant, J. W. Halloran, and B.

Derby, "Ink-Jet Printing of Wax-Based Alumina Suspensions," *J. Am. Ceram. Soc.*, vol. 84, no. 11, pp. 2514–2520, 2001, doi: 10.1111/j.1151-2916.2001.tb01045.x.

[87] J. A. Lewis, "Colloidal processing of ceramics," *J. Am. Ceram. Soc.*, 2000, doi: 10.1111/j.1151-2916.2000.tb01560.x.

[88] B. Derjaguin and L. D. Landau, "Theory of the stability of strongly charged lyophobic sols and of the adhesion of strongly charged particles in solutions of electrolytes," *Acta Physicochim. U.R.S.S.*, vol. 14, pp. 633–662, 1941.

[89] E. J. W. Verwey and J. T. G. Overbeek, "Theory of the Stability of Lyophobic Colloids," *Elsevier, Amsterdam*, 1948.

[90] E. M. Hotze, T. Phenrat, and G. V. Lowry, "Nanoparticle Aggregation: Challenges to Understanding Transport and Reactivity in the Environment," *J. Environ. Qual.*, vol. 39, no. 6, pp. 1909–1924, 2010, doi: 10.2134/jeq2009.0462.

[91] R. Moreno, "Colloidal Processing of Ceramic-Ceramic and Ceramic-Metal Composites," *Process. Prop. Adv. Ceram. Compos. III*, vol. 225, pp. 147–159, 2011, doi: 10.1002/9781118144442.ch13.

[92] A. Meurk, P. F. Luckham, and L. Bergström, "Direct measurement of repulsive and attractive van der Waals forces between inorganic materials," *Langmuir*, vol. 13, no. 14, pp. 3896–3899, 1997, doi: 10.1021/la9610967.

[93] R. H. French, "Origins and applications of London dispersion forces and Hamaker constants in ceramics," *J. Am. Ceram. Soc.*, vol. 83, no. 9, pp. 2117–2146, 2000, doi: 10.1111/j.1151-2916.2000.tb01527.x.

[94] L. Bergström, C. H. Schilling, and I. A. Aksay, "Consolidation Behavior of Flocculated Alumina Suspensions," *J. Am. Ceram. Soc.*, vol. 75, pp. 3305–3314, 1992.

[95] K. Lu, "Theoretical analysis of colloidal interaction energy in nanoparticle suspensions," *Ceram. Int.*, vol. 34, no. 6, pp. 1353–1360, 2008, doi: 10.1016/j.ceramint.2007.02.016.

[96] A. L. Ogden and J. A. Lewis, "Effect of nonadsorbed polymer on the stability of weakly flocculated suspensions," *Langmuir*, vol. 12, no. 14, pp. 3413–3424, 1996, doi: 10.1021/la950953o.

[97] W. M. Sigmund, N. S. Bell, and L. Bergström, "Novel powder-processing methods for advanced ceramics," *J. Am. Ceram. Soc.*, vol. 83, no. 7, pp. 1557–1574, 2000, doi: 10.1111/j.1151-2916.2000.tb01432.x.

[98] H. C. Hamaker, "The London-van der Waals attraction between spherical particles," *Physica*, vol. 4, no. 10, pp. 1058–1072, 1937, doi: 10.1016/S0031-8914(37)80203-7.

[99] J. S. Reed, *Principles of ceramics processing*. 1995.

[100] B. Faure *et al.*, "Dispersion and surface functionalization of oxide nanoparticles for transparent photocatalytic and UV-protecting coatings and sunscreens," *Sci. Technol. Adv. Mater.*, vol. 14, no. 2, 2013, doi: 10.1088/1468-6996/14/2/023001.

[101] F. F. Lange, "Colloidal processing of powder for reliable ceramics," *Curr. Opin. Solid State Mater. Sci.*, vol. 3, no. 5, pp. 496–500, 1998, doi: 10.1016/S1359-0286(98)80014-4.

[102] A. Kocjan and Z. Shen, "Colloidal processing and partial sintering of high-performance porous zirconia nanoceramics with hierarchical heterogeneities," *J. Eur.*

Ceram. Soc., vol. 33, no. 15–16, pp. 3165–3176, 2013, doi: 10.1016/j.jeurceramsoc.2013.06.004.

[103] J. Widegren and L. Bergström, "The effect of acids and bases on the dispersion and stabilization of ceramic particles in ethanol," *J. Eur. Ceram. Soc.*, vol. 20, no. 6, pp. 659–665, 2000, doi: 10.1016/S0955-2219(99)00199-5.

[104] E. Piacenza, A. Presentato, and R. J. Turner, "Stability of biogenic metal(loid) nanomaterials related to the colloidal stabilization theory of chemical nanostructures," *Crit. Rev. Biotechnol.*, vol. 38, no. 8, pp. 1137–1156, 2018, doi: 10.1080/07388551.2018.1440525.

[105] S. Novak, K. Vidovič, M. Sajko, and T. Kosmač, "Surface Modification of Alumina Powder for LPIM," *J. Eur. Ceram. Soc.*, 1997, doi: 10.1016/s0955-2219(96)00171-9.

[106] P. Thomas, B. Levenfeld, A. Várez, and A. Cervera, "Production of alumina microparts by powder injection molding," *Int. J. Appl. Ceram. Technol.*, vol. 8, no. 3, pp. 617–626, 2011, doi: 10.1111/j.1744-7402.2009.02471.x.

[107] A. Mannschatz, A. Müller, and T. Moritz, "Influence of powder morphology on properties of ceramic injection moulding feedstocks," *J. Eur. Ceram. Soc.*, 2011, doi: 10.1016/j.jeurceramsoc.2011.01.013.

[108] J. E. Zorzi, C. A. Perottoni, and J. A. H. Da Jornada, "Wax-based binder for low-pressure injection molding and the robust production of ceramic parts," *Ind. Ceram.*, vol. 23, no. 1, pp. 47–49, 2003.

[109] F. A. Çetinel, W. Bauer, M. Müller, R. Knitter, and J. Haußelt, "Influence of dispersant, storage time and temperature on the rheological properties of zirconia-paraffin feedstocks for LPIM," *J. Eur. Ceram. Soc.*, 2010, doi: 10.1016/j.jeurceramsoc.2009.12.003.

[110] S. T. Lin and R. M. German, "Interaction between binder and powder in injection moulding of alumina," *J. Mater. Sci.*, vol. 29, no. 19, pp. 5207–5212, 1994, doi: 10.1007/BF01151118.

[111] A. Dakskobler and T. Kosmač, "Rheological properties of re-melted paraffin-wax suspensions used for LPIM," *J. Eur. Ceram. Soc.*, vol. 29, no. 10, pp. 1831–1836, 2009, doi: 10.1016/j.jeurceramsoc.2008.11.012.

[112] J. L. Ortega-Vinuesa, A. Martín-Rodríguez, and R. Hidalgo-Álvarez, "Colloidal stability of polymer colloids with different interfacial properties: Mechanisms," *J. Colloid Interface Sci.*, vol. 184, no. 1, pp. 259–267, 1996, doi: 10.1006/jcis.1996.0619.

[113] S. Zürcher and T. Graule, "Influence of dispersant structure on the rheological properties of highly-concentrated zirconia dispersions," *J. Eur. Ceram. Soc.*, vol. 25, no. 6, pp. 863–873, 2005, doi: 10.1016/j.jeurceramsoc.2004.05.002.

[114] L. Bergström and E. Sjöström, "Temperature induced gelation of concentrated ceramic suspensions: Rheological properties," *J. Eur. Ceram. Soc.*, vol. 19, no. 12, pp. 2117–2123, 1999, doi: 10.1016/S0955-2219(99)00021-7.

[115] K. Lu and C. Kessler, "Colloidal dispersion and rheology study of nanoparticles," *J. Mater. Sci.*, vol. 41, no. 17, pp. 5613–5618, 2006, doi: 10.1007/s10853-006-0303-5.

[116] F. F. Lange, "Shape forming of ceramic powders by manipulation the interparticle pair potential," *Chem. Eng. Sci.*, vol. 56, no. 9, pp. 3011–3020, 2001, doi:

10.1016/S0009-2509(00)00484-X.

[117] V. Moloney, D. Parris, and M. Edirisinghe, "Rheology of Zirconia Suspensions in a Nonpolar Organic Medium," *J. Am. Ceram. Soc.*, vol. 78, pp. 3225–3232, Apr. 2005, doi: 10.1111/j.1151-2916.1995.tb07958.x.

[118] P. G. de Gennes, "Conformations of Polymers Attached to an Interface," *Macromolecules*, vol. 13, no. 5, pp. 1069–1075, 1980, doi: 10.1021/ma60077a009.

[119] W. M. De Vos, *Brushes and Particles*, no. September 2009. 2009.

[120] D. H. Napper, *Polymeric Stabilization of Colloidal Dispersions*. Academic Press, 1983.

[121] T. Tadros, "Interparticle interactions in concentrated suspensions and their bulk (Rheological) properties," *Adv. Colloid Interface Sci.*, vol. 168, no. 1–2, pp. 263–277, 2011, doi: 10.1016/j.cis.2011.05.003.

[122] T. Tadros, "Interaction forces between adsorbed polymer layers," *Adv. Colloid Interface Sci.*, vol. 165, no. 2, pp. 102–107, 2011, doi: 10.1016/j.cis.2011.02.002.

[123] T. Tadros, "Viscoelastic properties of sterically stabilised emulsions and their stability," *Adv. Colloid Interface Sci.*, vol. 222, pp. 692–708, 2015, doi: 10.1016/j.cis.2015.03.001.

[124] R. J. Pugh and L. Bergstrom, *Surface and Colloid Chemistry in Advanced Ceramics Processing*. Taylor \& Francis, 1993.

[125] D. M. Liu, "Effect of dispersants on the rheological behavior of zirconia-wax suspensions," *J. Am. Ceram. Soc.*, vol. 82, no. 5, pp. 1162–1168, 1999, doi: 10.1111/j.1151-2916.1999.tb01890.x.

[126] L. Gorjan, L. Reiff, A. Liersch, and F. Clemens, "Ethylene vinyl acetate as a binder for additive manufacturing of tricalcium phosphate bio-ceramics," *Ceram. Int.*, vol. 44, no. 13, pp. 15817–15823, 2018, doi: 10.1016/j.ceramint.2018.05.260.

[127] A. Dakskobler, A. Kocjan, and P. Bowen, "Predicting the yield stress of paraffin-wax suspensions," *Powder Technol.*, 2016, doi: 10.1016/j.powtec.2015.12.002.

[128] N. S. Bell, M. E. Schendel, and M. Piech, "Rheological properties of nanopowder alumina coated with adsorbed fatty acids," *J. Colloid Interface Sci.*, vol. 287, no. 1, pp. 94–106, 2005, doi: 10.1016/j.jcis.2005.01.113.

[129] S. Varchanis *et al.*, "Transition between solid and liquid state of yield-stress fluids under purely extensional deformations," *Proc. Natl. Acad. Sci. U. S. A.*, vol. 117, no. 23, pp. 12611–12617, 2020, doi: 10.1073/pnas.1922242117.

[130] Y. Xia, B. Gates, Y. Yin, and Y. Lu, "Monodispersed colloidal spheres: Old materials with new applications," *Adv. Mater.*, vol. 12, no. 10, pp. 693–713, 2000, doi: 10.1002/(SICI)1521-4095(200005)12:10<693::AID-ADMA693>3.0.CO;2-J.

[131] S. Lu, X. Chen, H. Zheng, Y. Zhao, and Y. Long, "Simulation and experiment on droplet volume for the needle-type piezoelectric jetting dispenser," *Micromachines*, vol. 10, no. 9, 2019, doi: 10.3390/mi10090623.

[132] X. Wang, W. W. Carr, D. G. Bucknall, and J. F. Morris, "High-shear-rate capillary viscometer for inkjet inks," *Rev. Sci. Instrum.*, vol. 81, no. 6, 2010, doi: 10.1063/1.3449478.

[133] V. Mechtcherine *et al.*, "Extrusion-based additive manufacturing with cement-based materials – Production steps, processes, and their underlying physics: A review,"

Cem. Concr. Res., vol. 132, no. March, p. 106037, 2020, doi: 10.1016/j.cemconres.2020.106037.

[134] Z. Zhou, M. J. Solomon, P. J. Scales, and D. V. Boger, "The yield stress of concentrated flocculated suspensions of size distributed particles," *J. Rheol. (N. Y. N. Y).*, vol. 43, no. 3, pp. 651–671, 1999, doi: 10.1122/1.551029.

[135] D. Liepsch, "A Basic Introduction to Rheology Shear Flow," *J Biomech*, vol. 35, no. 4, pp. 415–435, 2016, [Online]. Available: https://cdn.technologynetworks.com/TN/Resources/PDF/WP160620BasicIntroRheology.pdf.

[136] L. del-Mazo-Barbara and M. P. Ginebra, "Rheological characterisation of ceramic inks for 3D direct ink writing: A review," *J. Eur. Ceram. Soc.*, vol. 41, no. 16, pp. 18–33, 2021, doi: 10.1016/j.jeurceramsoc.2021.08.031.

[137] A. Mantelli, A. Romani, R. Suriano, M. Levi, and S. Turri, "Direct Ink Writing of Recycled Composites with Complex Shapes: Process Parameters and Ink Optimization," *Adv. Eng. Mater.*, vol. 23, no. 9, 2021, doi: 10.1002/adem.202100116.

[138] M. Yarahmadi, P. Barcelona, G. Fargas, E. Xuriguera, and J. J. Roa, "Optimization of the ceramic ink used in Direct Ink Writing through rheological properties characterization of zirconia-based ceramic materials," *Ceram. Int.*, vol. 48, no. 4, pp. 4775–4781, 2022, doi: 10.1016/j.ceramint.2021.11.013.

[139] N. Wang *et al.*, "Preparation of High-Stability Ceramic Slurry with Gel Behavior for Stereolithography 3D Printing," *Materials (Basel).*, vol. 16, no. 7, 2023, doi: 10.3390/ma16072816.

[140] R. Eickhoff, S. Antusch, S. Baumgärtner, D. Nötzel, and T. Hanemann, "Feedstock Development for Material Extrusion-Based Printing of Ti6Al4V Parts," *Materials (Basel).*, vol. 15, no. 18, 2022, doi: 10.3390/ma15186442.

[141] A. Elkaseer, K. J. Chen, J. C. Janhsen, O. Refle, V. Hagenmeyer, and S. G. Scholz, "Material jetting for advanced applications: A state-of-the-art review, gaps and future directions," *Addit. Manuf.*, vol. 60, no. PA, p. 103270, 2022, doi: 10.1016/j.addma.2022.103270.

[142] G. Li, T. Liu, X. Xiao, M. Gu, and W. Liao, "Numerical simulations of droplet forming, breaking and depositing behaviors in high-viscosity paste jetting," *J. Manuf. Process.*, vol. 78, no. December 2021, pp. 172–182, 2022, doi: 10.1016/j.jmapro.2022.03.047.

[143] B. Derby, "Inkjet printing ceramics: From drops to solid," *J. Eur. Ceram. Soc.*, vol. 31, no. 14, pp. 2543–2550, 2011, doi: 10.1016/j.jeurceramsoc.2011.01.016.

[144] B. Derby, "Additive Manufacture of Ceramics Components by Inkjet Printing," *Engineering*, vol. 1, no. 1, pp. 113–123, 2015, doi: 10.15302/J-ENG-2015014.

[145] D. Jang, D. Kim, and J. Moon, "Influence of fluid physical properties on ink-jet printability," *Langmuir*, vol. 25, no. 5, pp. 2629–2635, 2009, doi: 10.1021/la900059m.

[146] X. Xiao, G. Li, T. Liu, and M. Gu, "Experimental Study of the Jetting Behavior of High-Viscosity Nanosilver Inks in Inkjet-Based 3D Printing," *Nanomaterials*, vol. 12, no. 17, 2022, doi: 10.3390/nano12173076.

[147] P. Ried *et al.*, "Processing of YSZ screen printing pastes and the characterization of the electrolyte layers for anode supported SOFC," *J. Eur. Ceram. Soc.*, vol. 28, no.

9, pp. 1801–1808, 2008, doi: 10.1016/j.jeurceramsoc.2007.11.018.

[148] D. Burnat, P. Ried, P. Holtappels, A. Heel, T. Graule, and D. Kata, "The rheology of stabilised lanthanum strontium cobaltite ferrite nanopowders in organic medium applicable as screen printed SOFC cathode layers," *Fuel Cells*, vol. 10, no. 1, pp. 156–165, 2010, doi: 10.1002/fuce.200900014.

[149] N. S. Leyland, J. R. G. Evans, and D. J. Harrison, "Lithographic printing of force-sensitive resistors," *J. Mater. Sci. Mater. Electron.*, vol. 13, no. 7, pp. 387–390, 2002, doi: 10.1023/A:1016032325024.

[150] "Stearic acid." https://www.sigmaaldrich.com/SI/en/product/sial/175366?srsltid=AfmBOoqHORz2ScD-eYE4qPST5z5d6yUpiwHoZaTp9wQfiO_YwSnSHRXG.

[151] I. Özden Moser, M. Vukšić, M. Dular, A. Iveković, and A. Kocjan, "Tuning the rheological properties of paraffin-wax ceramic feedstocks for deposition with thermoplastic 3D printing," *J. Eur. Ceram. Soc.*, vol. 44, no. 13, pp. 7791–7800, 2024, doi: 10.1016/j.jeurceramsoc.2024.05.057.

[152] T. Mezger, *The Rheology Handbook*. 2020.

[153] W. H. Herschel and R. Bulkley, "Konsistenzmessungen von Gummi-Benzollösungen," *Kolloid-Zeitschrift*, vol. 39, no. 4, pp. 291–300, 1926, doi: 10.1007/BF01432034.

[154] E. Willems *et al.*, "Additive manufacturing of zirconia ceramics by material jetting," *J. Eur. Ceram. Soc.*, vol. 41, no. 10, pp. 5292–5306, Aug. 2021, doi: 10.1016/j.jeurceramsoc.2021.04.018.

[155] W. J. Tseng, D. M. Liu, and C. K. Hsu, "Influence of stearic acid on suspension structure and green microstructure of injection-molded zirconia ceramics," *Ceram. Int.*, vol. 25, no. 2, pp. 191–195, 1999, doi: 10.1016/S0272-8842(98)00024-8.

[156] L. Gorjan, C. Galusca, M. Sami, T. Sebastian, and F. Clemens, "Effect of stearic acid on rheological properties and printability of ethylene vinyl acetate based feedstocks for fused filament fabrication of alumina," *Addit. Manuf.*, vol. 36, no. March, p. 101391, 2020, doi: 10.1016/j.addma.2020.101391.

[157] B. Loebbecke, R. Knitter, and J. Haußelt, "Rheological properties of alumina feedstocks for the low-pressure injection moulding process," *J. Eur. Ceram. Soc.*, 2009, doi: 10.1016/j.jeurceramsoc.2008.11.001.

[158] V. Inês dos Santos, M. Celso Fredel, B. Henriques, and L. Gremillard, "Rheological characterization of pastes of Alumina-Toughened Zirconia with additions of carbon nanofibers and evaluation of their printability via Material Extrusion," vol. 131, no. April, pp. 1784–1801, 2023, doi: 10.1016/j.jmapro.2024.09.094.

[159] A. Kocjan, A. Abram, and A. Dakskobler, "Impact strengthening of 3Y-TZP dental ceramic root posts," *J. Eur. Ceram. Soc.*, vol. 40, no. 14, pp. 4765–4773, 2020, doi: 10.1016/j.jeurceramsoc.2020.02.040.

[160] T. Kosmac, C. Oblak, P. Jevnikar, N. Funduk, and L. Marion, "The effect of surface grinding and sandblasting on flexural strength and reliability of Y-TZP zirconia ceramic.," *Dent. Mater.*, vol. 15, no. 6, pp. 426–433, Nov. 1999, doi: 10.1016/s0109-5641(99)00070-6.

[161] J. Cotič, P. Jevnikar, and A. Kocjan, "Ageing kinetics and strength of airborne-

particle abraded 3Y-TZP ceramics," *Dent. Mater.*, vol. 33, no. 7, pp. 847–856, 2017, doi: 10.1016/j.dental.2017.04.014.

[162] T. Mirt *et al.*, "Effect of airborne-particle abrasion of yttria-containing zirconia dental ceramics on mechanical properties before and after regeneration firing," *J. Eur. Ceram. Soc.*, vol. 42, no. 12, pp. 5035–5044, 2022, doi: https://doi.org/10.1016/j.jeurceramsoc.2022.05.010.

[163] Q. Flamant and M. Anglada, "Hydrofluoric acid etching of dental zirconia. Part 2: effect on flexural strength and ageing behavior," *J. Eur. Ceram. Soc.*, vol. 36, no. 1, pp. 135–145, 2016, doi: https://doi.org/10.1016/j.jeurceramsoc.2015.09.022.

[164] R. K. Chintapalli, A. Mestra Rodriguez, F. Garcia Marro, and M. Anglada, "Effect of sandblasting and residual stress on strength of zirconia for restorative dentistry applications," *J. Mech. Behav. Biomed. Mater.*, vol. 29, pp. 126–137, 2014, doi: https://doi.org/10.1016/j.jmbbm.2013.09.004.

[165] Y. Lu *et al.*, "Flexural strength and Weibull analysis of Y-TZP fabricated by stereolithographic additive manufacturing and subtractive manufacturing," *J. Eur. Ceram. Soc.*, vol. 40, no. 3, pp. 826–834, 2020, doi: https://doi.org/10.1016/j.jeurceramsoc.2019.10.058.

[166] A. Zenthöfer *et al.*, "Strength and reliability of zirconia fabricated by additive manufacturing technology," *Dent. Mater.*, vol. 38, no. 10, pp. 1565–1574, 2022, doi: https://doi.org/10.1016/j.dental.2022.07.004.

[167] G. Quinn, *Fractography of Ceramics and Glasses (1st edition)*. 2007.

[168] F. F. LANGE, B. I. DAVIS, and I. A. AKSAY, "Processing-Related Fracture Origins: III, Differential Sintering of ZrO2 Agglomerates in Al2O3/ZrO2 Composite," *J. Am. Ceram. Soc.*, vol. 66, no. 6, pp. 407–408, 1983, doi: https://doi.org/10.1111/j.1151-2916.1983.tb10070.x.

[169] A. R. Studart, E. Amstad, M. Antoni, and L. J. Gauckler, "Rheology of concentrated suspensions containing weakly attractive alumina nanoparticles," *J. Am. Ceram. Soc.*, vol. 89, no. 8, pp. 2418–2425, 2006, doi: 10.1111/j.1551-2916.2006.01087.x.

[170] R. Lenk and A. P. Krivoshchepov, "Effect of surface-active substances on the rheological properties of silicon carbide suspensions in paraffin," *J. Am. Ceram. Soc.*, vol. 83, no. 2, pp. 273–276, 2000, doi: 10.1111/j.1151-2916.2000.tb01184.x.

[171] S. M. Wolfrum and J. J. Ponjeé, "Surface modification of powders with carboxylic acids," *J. Mater. Sci. Lett.*, vol. 8, no. 6, pp. 667–669, 1989, doi: 10.1007/BF01730436.

[172] R. L. Hoffman, "Discontinuous and dilatant viscosity behavior in concentrated suspensions. II. Theory and experimental tests," *J. Colloid Interface Sci.*, vol. 46, no. 3, pp. 491–506, 1974, doi: https://doi.org/10.1016/0021-9797(74)90059-9.

[173] H. A. Barnes, "A review of the slip (wall depletion) of polymer solutions, emulsions and particle suspensions in viscometers: its cause, character, and cure," *J. Nonnewton. Fluid Mech.*, vol. 56, no. 3, pp. 221–251, 1995, doi: https://doi.org/10.1016/0377-0257(94)01282-M.

[174] P. Filip, B. Hausnerova, and L. Cucova, "ON THE MODELLING OF NON-MONOTONOUS VISCOSITY DESCRIBING FEEDSTOCK BEHAVIOR IN POWDER INJECTION MOULDING," no. July, pp. 192–195, 2012.

[175] L. Bergström, "Shear thinning and shear thickening of concentrated ceramic suspensions," *Colloids Surfaces A Physicochem. Eng. Asp.*, vol. 133, no. 1–2, pp. 151–155, 1998, doi: 10.1016/S0927-7757(97)00133-7.

[176] M. Bek, J. Gonzalez-Gutierrez, C. Kukla, K. P. Črešnar, B. Maroh, and L. S. Perše, "Rheological behavior of highly filled materials for injection moulding and additive manufacturing: Effect of particle material and loading," *Appl. Sci.*, vol. 10, no. 22, pp. 1–23, 2020, doi: 10.3390/app10227993.

[177] N. Reis and B. Derby, "Ink jet deposition of ceramic suspensions: Modelling and experiments of droplet formation," *Mater. Res. Soc. Symp. - Proc.*, vol. 624, no. January 2000, pp. 65–70, 2000, doi: 10.1557/proc-625-117.

[178] B. Cappi, E. Özkol, J. Ebert, and R. Telle, "Direct inkjet printing of Si3N4: Characterization of ink, green bodies and microstructure," *J. Eur. Ceram. Soc.*, vol. 28, no. 13, pp. 2625–2628, 2008, doi: 10.1016/j.jeurceramsoc.2008.03.004.

[179] B. Derby, "Inkjet printing of functional and structural materials: Fluid property requirements, feature stability, and resolution," *Annu. Rev. Mater. Res.*, vol. 40, no. June 2010, pp. 395–414, 2010, doi: 10.1146/annurev-matsci-070909-104502.

[180] J. Ebert *et al.*, "Direct inkjet printing of dental prostheses made of zirconia," *J. Dent. Res.*, vol. 88, no. 7, pp. 673–676, Jul. 2009, doi: 10.1177/0022034509339988.

[181] A. Hadian, M. Fricke, A. Liersch, and F. Clemens, "Material extrusion additive manufacturing of zirconia parts using powder injection molding feedstock compositions," *Addit. Manuf.*, vol. 57, no. February, p. 102966, 2022, doi: 10.1016/j.addma.2022.102966.

[182] C. Tosto, J. Tirillò, F. Sarasini, and G. Cicala, "Hybrid metal/polymer filaments for fused filament fabrication (FFF) to print metal parts," *Appl. Sci.*, vol. 11, no. 4, p. 1, 2021, doi: 10.3390/app11041444.

[183] T. Gajjar, R. Yang, L. Ye, and Y. X. Zhang, "Effects of key process parameters on tensile properties and interlayer bonding behavior of 3D printed PLA using fused filament fabrication," *Prog. Addit. Manuf.*, vol. 10, no. 2, pp. 1261–1280, 2025, doi: 10.1007/s40964-024-00704-y.

[184] M. Staudacher *et al.*, "Strength limiting defects in additively manufactured ceramics," *Open Ceram.*, vol. 24, no. August, p. 100858, 2025, doi: 10.1016/j.oceram.2025.100858.

[185] H. Nakai *et al.*, "Additively manufactured zirconia for dental applications," *Materials (Basel).*, vol. 14, no. 13, pp. 1–9, 2021, doi: 10.3390/ma14133694.

[186] A. Hadian *et al.*, "Material extrusion based additive manufacturing of large zirconia structures using filaments with ethylene vinyl acetate based binder composition," *Addit. Manuf.*, vol. 47, no. April, p. 102227, 2021, doi: 10.1016/j.addma.2021.102227.

Bibliography

Publications Related to the Thesis

Journal Articles

Özden, I., Iveković, A. & Kocjan, A. Additive manufacturing of ceramics from thermoplastic feedstocks. Open Ceram. 6, (2021). https://doi.org/10.1016/j.oceram.2021.100129 (COBISS.SI-ID 64927491)

Özden, I., Scheithauer U., Iveković, A. & Kocjan, A. Effect of Infill Strategy on the Flexural Strength of 3Y-TZP Bars Fabricated by Thermoplastic 3D Printing (T3DP), Open Ceram. (2023). https://doi.org/10.1016/j.oceram.2023.100367 (COBISS.SI-ID 154191107)

I. Özden Moser, M. Vukšić, M. Dular, A. Iveković, and A. Kocjan, "Tuning the rheological properties of paraffin-wax ceramic feedstocks for deposition with thermoplastic 3D printing," J. Eur. Ceram. Soc., vol. 44, no. 13, pp. 7791–7800, 2024, doi: 10.1016/j.jeurceramsoc.2024.05.057 (COBISS.SI-ID 205464579)

Conference Papers

Oral presentation *'Thermoplastic 3D Printing: The Effect of Particle Interactions and Infill Strategies on the Properties of Zirconia Parts'* at 29th International Conference on Materials and Technology, 2024, Portorož, Slovenia

Oral presentation *'Thermoplastic 3D printing of zirconia parts with varying infill strategies'* at young Ceramists Additive Manufacturing Forum, 2022, University of Barcelona, Barcelona, Spain (COBISS.SI-ID 154307587)

Poster presentation *'Effect of feedstock properties and process parameters on the quality of parts prepared with thermoplastic 3D printing'* at Ceramics in Europe, 2022, Krakow, Poland (COBISS.SI-ID 144284675)

Oral and poster presentation *'Effect of infill strategy on mechanical properties of parts prepared by thermoplastic 3D printing'* at 14th Jožef Stefan International Postgraduate School Students' Conference, 2022, Kamnik, Slovenia (COBISS.SI-ID 139166723)

Oral and poster presentation *'Thermoplastic 3D Printing of Ceramics'* at 13th Jožef Stefan International Postgraduate School Students' Conference, 2021, online (COBISS.SI-ID 69755907)

Poster presentation *'Microstructural and mechanical evaluation of rectangular bars additively manufactured by FFF'* at young Ceramists Additive Manufacturing Forum, 2020, online (COBISS.SI-ID 154247427)

Other Publications

Jevnikar, A.P.; Malgaj, T.; Radan, K.; Özden, I.; Kušter, M.; Kocjan, A. Rheological Properties and Setting Kinetics of Bioceramic Hydraulic Cements: ProRoot MTA versus RS+. Materials 2023, 16, 3174. https://doi.org/10.3390/ma16083174 (COBISS.SI-ID 149530371)

Biography

The author of this thesis, İpeknaz Özden Moser, was born in 1993, in Istanbul. From 2006 to 2012, she was a member of Turkish National Sailing Team. In 2012, she started studying Bioengineering in Ege University, Engineering Faculty, Bioengineering Department in Izmir, Turkey. During 2014-15, she completed voluntary internship at Animal Cell Culture and Tissue Engineering Laboratory, Ege University in Izmir, Turkey and received a research experience certificate. In 2015, she completed a mandatory internship at 3D Systems Design and Realization Research Laboratory, Sabanci University in Istanbul, Turkey. In 2016, she received her Bachelor's Degree, graduating with the 3rd highest GPA of her class. In 2016, she started studying Materials Science and Nano Engineering in Sabanci University, Faculty of Engineering and Natural Sciences, Materials Science and Nano Engineering Program in Istanbul, Turkey. She was a recipient of Full Scholarship and Summer Projects Scholarship. She was Master Teaching Assistant for Science of Nature 101 course for which she won the 3rd place in First Year Teaching Assistant Award. She was also the Country Representative at Asian Science Camp 2017. She was a member of the Sabanci University sailing team for which she received Extracurricular Student Activities Award. In 2018, has received her Master's degree and started doctoral studies.

She has completed doctoral studies at Jožef Stefan International Postgraduate School Nanosciences and Nanotechnologies Study Program in Ljubljana, Slovenia. During her PhD, she attended Spring School "3D Printing and ceramic processes", in 2019, in Maubeuge, France, as recipient of JECS Trust grant. Also, in 2019, she attended young Ceramists Additive Manufacturing Forum, in University of Mons in Mons, Belgium and 11th Jožef Stefan International Postgraduate School Students' Conference, in Planica, Slovenia. In 2020, she had a poster presentation titled '*Microstructural and mechanical evaluation of rectangular bars additively manufactured by FFF'* at young Ceramists Additive Manufacturing Forum, that was held online. In 2021, she had oral and poster presentation *'Thermoplastic 3D Printing of Ceramics'* at 13th Jožef Stefan International Postgraduate School Students' Conference, that was held online. Also, in 2021, she was a visiting researcher at Fraunhofer IKTS, in Dresden, Germany for 2.5 months, as recipient of JECS Trust grant for mobility. In 2022, she had oral and poster presentation titled *'Effect of infill strategy on mechanical properties of parts prepared by thermoplastic 3D printing'* at 14th Jožef Stefan International Postgraduate School Students' Conference, in Kamnik, Slovenia. She had a poster presentation titled *'Effect of feedstock properties and process parameters on the quality of parts prepared with thermoplastic 3D printing'* at Ceramics in Europe 2022 conference in Krakow, Poland. She had an oral presentation *'Thermoplastic 3D printing of zirconia parts with varying infill strategies'* at young Ceramists Additive Manufacturing Forum, at University of Barcelona, in Barcelona, Spain, which she attended as recipient of JECS Trust grant. Finally, in 2024, she had an oral presentation *'Thermoplastic 3D Printing: The Effect of Particle Interactions and Infill Strategies on the Properties of Zirconia Parts'* at 29th International Conference on Materials and Technology, in Portorož, Slovenia.